REPORT DOCUMENTATION PAGE

Form Approved
OMB No. 0704-0188

1. AGENCY USE ONLY *(Leave blank)*	2. REPORT DATE	3. REPORT TYPE AND DATES COVERED
	February 15, 2001	Technical 03/31/98 to 2/15/01

4. TITLE AND SUBTITLE: Development and Testing of the Virginia Tech Doppler Global Velocimeter

5. FUNDING NUMBERS
N00014-98-1-0425

6. AUTHORS

Troy B. Jones and Roger L. Simpson

7. PERFORMING ORGANIZATION NAME(S) AND ADDRESS(ES)

Department of Aerospace and Ocean Engineering
Virginia Polytechnic Institute and State University
Blacksburg, Virginia 24061-0203

8. PERFORMING ORGANIZATION REPORT NUMBER

VPI-AOE-271

9. SPONSORING/MONITORING AGENCY NAME(S) AND ADDRESS(ES)

Office of Naval Research
800 N. Quincy Street
Arlington, Virginia 22217

10. SPONSORING/MONITORING AGENCY REPORT NUMBER

11. SUPPLEMENTARY NOTES

12a. DISTRIBUTION/AVAILABILITY STATEMENT

Unlimited

DISTRIBUTION STATEMENT A
Approved for Public Release
Distribution Unlimited

12b. DISTRIBUTION CODE

13. ABSTRACT *(Maximum 200 words)*

A new laser based flow interrogation system, capable of simultaneous measurement of planar three-component velocity data, was constructed and tested. The Virginia Tech Doppler Global Velocimeter (DGV) system was designed for use in the Virginia Tech Stability Wind Tunnel as a tool for investigating complex three-dimensional separated flow regions. The systems was designed for robustness, ease of use, and for acquisition of low uncertainty velocity data. A series of tests in the Stability Tunnel were conducted to determine the how well the new DGV system met these goals. Extensive calibration tests proved the system is capable of measuring the frequency shifts of scattered laser light, and therefore velocity. However, equipment failures and inadequate flow seed density prevented accurate velocity measurements in the separated wake region behind a 6:1 prolate spheroid. Detailed uncertainty analysis techniques demonstrated that, under the proper conditions, the system is capable of making velocity measurements with approximately +/- 2m/s uncertainty.

14. SUBJECT TERMS	15. NUMBER OF PAGES
Doppler Global velocimetry, planar Doppler velocimetry	112
	16. PRICE CODE

17. SECURITY CLASSIFICATION OF REPORT	18. SECURITY CLASSIFICATION OF THIS PAGE	19. SECURITY CLASSIFICATION OF ABSTRACT	20. LIMITATION OF ABSTRACT
UNCLASSIFIED	UNCLASSIFIED	UNCLASSIFIED	UNLIMITED

Contents

List of Figures

List of Tables

Chapter 1

Introduction

Experimental measurements of fluid flow properties are fundamental to understanding fluid dynamics. Fluid flow measurements provide necessary data for a multitude of tasks, from vehicle and building design, to validation of Computational Fluid Dynamics simulations. The data required for these tasks range from pressure and velocity measurements,to forces and moments acting on the object in the flow, and even quantities such as skin friction. In this research, we focus on the measurement of fluid velocities. Fluid velocity measurement techniques fall into one of two possible broad categories – intrusive or non-intrusive – as described in the following sections.

1.1 Intrusive Techniques

Intrusive flow measurement methods rely on the placement of a probe which directly measures the desired quantity within the region of interest. Examples of such techniques include the use of pressure and hot-wire probes to measure fluid velocities. Pressure probes and hot-wire systems are point measurement techniques. To collect data from an entire region, the probe head must be traversed to many discrete points in a grid pattern. This process is time consuming, but well established and useful for collecting data, particularly in steady flow fields.

1.1.1 Pressure Probes

Pressure measurement probes (i.e. pitot and pitot-static) measure the difference between the static and stagnation pressures at a point in the flow. For low speed flows,

this pressure difference yields a component of velocity at the tip of the probe. Probes with multiple static pressure ports around the circumference of the probe are capable of measuring multiple velocity components [1]. However, due to their limited frequency response range of less than $100Hz$, pressure probes are most suited to measurement of mean flow velocities.

1.1.2 Hot-Wire Systems

Hot-wire systems measure changes in resistance of an electrically heated wire element immersed in the flow. These changes in resistance are due to thermal convection and are a function of the velocity component perpendicular to the wire. Anemometer circuits are set to maintain either the temperature of the wire, or the current flow through it, thereby providing a difference signal for velocity calculations. The use of several wires mounted at varying angles on the probe head supplies multiple component velocity data. Typical hot-wire systems measure velocities with frequency responses range of $20kHz$ making them useful for turbulence measurements.

1.2 Non-Intrusive Techniques

Non-intrusive techniques commonly use optics with laser illumination to measure flow properties as viewed through a window. Examples of non-intrusive methods range from the well established Laser Doppler Anemometry (LDA) to the newer techniques of Particle Image Velocimetry (PIV) and Doppler Global Velocimetry (DGV). The techniques of LDA and DGV are based on the measurement of Doppler shift of scattered laser light from seed* particles, while PIV relies on direct tracking of seed particles in the flow.

1.2.1 Laser Doppler Anemometry

Laser Doppler Anemometry is a point measurement technique, where the measurement point is defined by the crossing of two laser beams. By slightly shifting the frequency of one beam relative with respect to the other, interference fringes are created at the intersection of the beams (known as the measurement volume). As seed particles pass through the measurement volume fringes, laser light is scattered with a Doppler shifted

*Flow seeding refers to the injection of particulate matter into the flow. The size and density of the particles depend on the requirements of the technique.

frequency. The scattered light is collected and amplified by a photo-multiplier tube which is sampled by specialized LDA processors which perform Fast Fourier Transforms on the signal. The recovered frequency information is then used to calculate the velocity of the particle through the measurement volume. Crossing multiple beams at the same point allows for multi-component velocity measurement. A miniature three-component LDA system was used to acquire flow velocities and turbulence data in the crossflow separated region behind a 6:1 prolate spheriod [2]. A five component LDA for turbulence measurements is described in Ölçmen and Simpson [3].

1.2.2 Particle Image Velocimetry

Particle Image Velocimetry is a non-Doppler shift based planar velocity measurement technique. A pulse laser beam is spread into a sheet passing through a seeded flow of interest. Digital cameras acquire images of the particles passing through the plane at discrete time intervals. The individual particles are then tracked frame by frame to determine the velocity for each particle. The implementation of PIV is straightforward and easy to understand, but extracting meaningful velocity data requires complex algorithms to track the individual particles through the image sequences. Fundamentally, PIV is limited to two-component measurements in the laser sheet plane. Newer variants of PIV use holographic methods or stereo camera systems to obtain an estimate of the out-of-plane velocity component [4].

1.2.3 Doppler Global Velocimetry

Doppler Global Velocimeter systems are known by various names, including Planar Doppler Velocimetry (PDV) and Filtered Rayleigh Scattering (FRS). Regardless of the name, the basic operational principles of these planar system are equivalent. The systems measure velocities over planar regions by passing a laser sheet though a fluid flow of interest and digitally imaging two views of the laser sheet plane. One camera view passes through a molecular filter while the other is left unfiltered. A popular choice of molecular filter is diatomic iodine vapor enclosed in a glass cylinder with optical windows at each end. Iodine is an excellent choice for planar velocimeter use for two important reasons: one, the atomic absorption spectrum is well documented; and two, iodine has several strong absorption lines in the wavelength range of Argon-Ion continuous wave (cw) gas lasers ($514nm$), and Nd:YAG [†] solid state pulse lasers ($532nm$). Examples of such absorption lines versus relative frequency (from $532.247nm$ or 5.6326×10^5 GHz)

[†]Neodynum: Yittrium Aluminum Garnet, the chemical composition of the core rod within the laser

are plotted in Figure 1.1. Tuning the frequency output of the laser to fall midway on the absorption line slope then provides increases or decreases in light transmission as a function of the incoming light Doppler shifted frequency.

After alignment of the filtered and reference views and some image processing, the views are divided on a pixel by pixel basis yielding an image whose pixel intensity values are proportional to Doppler shift. Knowing the Doppler shifts at each pixel allows calculation of a velocity component for each pixel. The relationship between Doppler shift and velocity is given by Equation 1.1,

$$\Delta f = \frac{1}{\lambda}(\bar{o} - \bar{l}) \cdot \vec{V} \tag{1.1}$$

where Δf represents the Doppler shift, λ the wavelength of the incident laser light, $\bar{o}$ the unit vector in the observing direction, $\bar{l}$ the unit vector in the incident laser direction, and $\vec{V}$ the total velocity vector. Relative placement of the camera systems and the laser sheet specify the incident light and observation vectors. Use of three camera systems – collecting reference and filtered images from three angles relative to the laser sheet – allows determination of the total velocity vector for each pixel in the normalized image.

1.3 Research Movtivation

The development of the Virginia Tech DGV system was motivated by a need to measure large scale velocity fields in subsonic flow conditions. The key design driver for the system was the ability to measure instantaneous velocities in the unsteady three-dimensional separated wake region behind a maneuvering wind tunnel model. Accomplishing this requires a non-intrusive measurement technique capable of measuring three-component velocities simultaneously in a planar region. The planar measurement requirement precludes the use of point techniques such as LDA. The use of a PIV system would meet the planar measurement constraint, however PIV depends on multiple exposures over time to calculate velocity fields which does not meet the instantaneous measurement requirement. This leaves the new technique of Doppler Global Velocimetry as the only viable option. The research described herein resulted in the construction and testing of a DGV system tailored to meet these objectives.

Chapter 2

Previous Work

In this chapter we review the methods of planar Doppler velocimetry which have influenced the design of the Virginia Tech DGV system. The major emphasis is placed on reviewing systems designed for low-speed flow measurements. Finally, a brief review of the flow features around a 6:1 prolate spheroid is presented.

2.1 Planar Doppler Measurement Techniques

Modern planar Doppler velocity measurement techniques arose from work performed in the mid 1980's by Shimizu *et al.* [5, 6]. They developed a High Spectral Resolution LIDAR system, based on a combination of diatomic iodine molecular filters and scattered laser light, to remotely measure atmospheric properties.

Two groups performed the pioneering work in making molecular filter based techniques useful for fluid dynamic testing. Both research teams developed planar Doppler measurement systems that operated on the same principles as discussed in Section 1.2.3. The efforts of the two groups differed in the type of laser light scattering utilized by their systems.

2.1.1 Rayleigh Scattering Techniques

Miles *et al.* [7] at Princeton University were the first to develop a system based on molecular, or Rayleigh, scattering. Their technique relies on scattered laser light from the gas molecules inherent in the flow and is practical only for supersonic measurements. Tuning the output wavelength of the laser to an appropriate iodine absorption line effec-

tively attenuates the laser scattering from tunnel walls, while passing the Doppler shifted scattered light through the filter. The technique is termed Filtered Rayleigh Scattering (FRS) and has been used to measure boundary layer formation [8] and turbulence [9] in supersonic flows.

The Rayleigh scattering spectrum is a function of the thermal and acoustic motions of the scattering molecules [7]. This allows (FRS) systems to simultaneously measure flow velocities and thermodynamic properties. A recent example of such a measurement system is given in Elliot *et al.* [10].

Another characteristic of high speed planar Doppler systems is the use of pressure broadened molecular filters. Pressure, or Lorentz, broadened filters are created by adding an inert buffer gas into the molecular filter. This increases the width of the absorption line as compared to the same frequency range for a non-broadened filter. A wider absorption line allows a greater dynamic range for the velocity measurements [4].

2.1.2 Mie Scattering Techniques

Particle, or Mie, scattering techniques were first introduced by Komine *et al.* [11]. Their system relied on imaging a laser sheet in a particle seeded flow with standard video cameras. The reference and filtered images were divided in "real-time" – at 30 frames-per-second – by an analog circuit with the resulting normalized image digitized and stored in a computer for processing. This system was simple in design and suffered from high uncertainties, but proved the viability of the Doppler Global Velocimeter.

More recent examples of DGV systems show how the technique has evolved from its humble beginnings. The fundamental operations are the same, but continuous improvements in the data processing methods and compensation for laser frequency drift have made DGV systems true tools for flow measurements. In the following sections we review DGV systems of a few key groups who introduced innovations in DGV and whose work directly influenced the Virginia Tech DGV system.

NASA DGV Research

Work began at NASA Langley on DGV development in 1991 when Meyers worked with Komine to develop a prototype one-component DGV system using an argon-ion continuous wave laser [12]. The system was similar to Komine's original system, using RS-170 standard video cameras and analog divider circuitry. However, as the system evolved, digitizing boards were used to capture the image frames from 8-bit CCD video cameras

and digital image processing techniques were employed. Digitizing the camera frames allowed for image corrections which were not possible with analog methods. These image processing improvements included [13, 14];

- Matching of the reference and filtered views to sub-pixel accuracy
- Correction of the data images for perspective distortion
- Subtraction of background light levels from each data image
- Correction for CCD pixel sensitivity
- Use of a Nd:YAG Pulse laser for resolution of instantaneous flow features

In 1998 Meyers used a full three-component DGV to investigate the flow field of a helicopter rotor wake [15]. The system used six standard CCD video cameras (two per viewing angle) digitized to 10 bit resolution. The tests were performed in NASA Langley 14x22 *ft* Subsonic Tunnel with the laser and cameras mounted inside the tunnel's open test section. From those tests it was concluded that the stability of the Nd:YAG laser frequency output and the temperature control of the iodine cells were adversely affected by the harsh environment of the wind tunnel. The tests also revealed a problem with laser speckle noise in the data images.

Laser speckle noise appears in images illuminated with pulse lasers, and is due to interference patterns created when monochromatic laser light is scattered by particles in the flow. Smith [16] performed a series of tests to determine the best methods for reducing the laser speckle noise in planar Doppler based systems. He determined that reductions in laser speckle were achieved by using the lowest f/number* lens settings possible with low magnification factors and by averaging multiple images over time.

On the west coast at NASA Ames, McKenzie performed crucial research on quantifying the errors in planar Doppler measurement techniques [17]. McKenzie's rigorous error analysis led to several important conclusions about the design of future planar Doppler systems. McKenzie showed that 8-bit digital truncation error limits detector resolution to around 8 *MHz* for instantaneous measurements, and requires image averaging to provide adequately low uncertainties. He made the assertion that the use of 16-bit scientific grade digital cameras would provide the optimal instantaneous resolution of approximately 2 *MHz* Doppler shift (corresponding to about 1.5 $\frac{m}{s}$). This higher resolution data requires fewer averages to achieve a desired uncertainty level, which translates into less time to acquire a high accuracy data set.

*The f/number or, f/stop is the ratio of the focal length to the aperture diameter

Another significant contribution from McKenzie's research is the use of a laser "reference tab" in for tracking of laser output frequency. The Nd:YAG pulse lasers predominantly used in DGV work experience pulse-to-pulse output frequency variations as large as $10MHz$ while injection seeded[†] [18]. While this variance is small in terms of absolute frequency, it corresponds to a sizeable velocity change. Therefore, for low-speed flow measurements, a means of tracking the output frequency of the laser for each pulse is required. Each single pulse data image may then be corrected for the actual laser frequency. A typical laser pulse lasts approximately 10 ns making direct measurement of the pulse frequency with a spectrum analyzer impractical. It is reasonable to then consider using a molecular filter and camera or photodiode system to track the laser's frequency in the same manner as the DGV system. McKenzie developed and tested a simple tracking system by directing a small portion of the beam onto a tab within the field of view of one of the cameras. The reference tab is stationary and outside of the flow, providing a reference laser intensity with zero Doppler shift. McKenzie performed

[†]In an injection seeded Nd:YAG laser, a smaller high stability and frequency tunable laser is fired directly into the host Nd:YAG laser to produce a more stable output beam.

more research targeted at the use of DGV in low speed flows [19, 20]. Utilizing an ideal laboratory setup, he was able to measure rotating wheel velocities with $\pm 1 \frac{m}{s}$ accuracy. Tests were then conducted in the 80x120 *ft* Full Scale Wind Tunnel at NASA Ames and measured velocities in a full scale helicopter rotor flow.

The DGV system research at NASA yielded a great deal of valuable information on the design and operation of DGV systems. The advances made in the areas of data processing and laser speckle reduction have been widely adopted by many researchers. Unlike many other systems, those developed at NASA (Langley and Ames) were tested in large scale tunnels, rather than the more common small diameter free expanding jet experiments. Lessons learned from these DGV systems were directly applied to the development of the Virginia Tech DGV.

University DGV Research

Unlike the research in high speed Filtered Rayleigh Scattering systems, university involvement in DGV research did not begin until the late 1990's. Doppler Global Velocimeter systems developed at Rutgers and West Virginia Universities are using lessons learned from the NASA research experiences to make new advances in DGV.

An early DGV system developed at Rutgers University by Mosedale *et al.* [21] was only a single component system, but included some important features. The system utilized two 16-bit scientific grade digital cameras with an Nd:YAG laser, and featured a laser pulse frequency tracking system. Those measurements yielded instantaneous velocity uncertainties as low as $4\frac{m}{s}$ which lowered to $2 \frac{m}{s}$ for averaged data sets. That same year Arnette and Elliot developed a novel color-based DGV system [22]. Instead of relying on image processing to align the reference and filtered views, their system illuminated the flow with two laser wavelengths and recorded images on color CCD cameras. One laser wavelength was tuned to operate on an iodine absorption line, while the other wavelength was not. This resulted in a reference and filtered views collected on separate color channels of the same camera, eliminating the need to align the views. Recently Elliot *et al.* [23] presented a comprehensive overview of research into the techniques of both DGV and other planar Doppler systems.

Work on DGV at West Virginia University began with development of a single point system [24]. The point technique relies on photo-diodes to measure light intensity through the same type of molecular iodine cells used by Meyers at NASA Langley. Later work added a second photo-diode to measure two velocity component data on a rotating wheel and achieved uncertainties less than $1 \frac{m}{s}$ [25]. Expanding on the work for the point system, Naylor developed a two component camera based DGV [26, 27]. The system

used four Hitachi 8-bit CCD cameras, with illumination from an argon ion continuous wave laser. Naylor acquired data sets on a rotating wheel standard and in a turbulent pipe exhaust flow and reported 1-2 $\frac{m}{s}$ uncertainties.

2.2 Prolate Spheroid Flow

The test data acquired for the Virginia Tech DGV measured velocities in the wake of a 6:1 prolate spheroid. The wake behind a prolate spheroid at an angle of attack is dominated by crossflow vortical separation. Many investigations into the steady and unsteady prolate spheroid flow features have been conducted at Virginia Tech. Three-component velocity measurements made with a miniature LDA probe and a hot-wire probe system are described in Chesnakas *et al.* [2]. That research resulted in a detailed velocity map of the steady flow case at selected longitudinal stations on the leeward side of the prolate spheroid. Plots of this data are shown in Figure 1.2. Wetzel [28, 29] measured steady and unsteady skin friction values over the spheroid surface and mapped the separation lines shown in Figure 1.2.

The prolate spheroid flow is of practical interest for several reasons. The generic shape is similar to submarine hulls, missiles, torpedoes and even aircraft fuselages. The three-dimensional nature of the separated wake of a prolate spheroid has proven difficult to model using CFD techniques. Therefore, experimental data is needed to improve the accuracy of computational methods and our general understanding of such complex flows.

Chapter 3

Virginia Tech DGV System Design

Since the inception of DGV, advances in system design have proceeded evolutionarily; groups built and tested new systems with incremental advances over previous systems, tailoring techniques for their particular use. The design of the Virginia Tech DGV makes maximum use of this pattern by taking the best aspects of previous DGV work and incorporating them into a single system. This methodology is evident in our selections of an Nd:YAG pulse laser for illumination, scientific grade 16-bit CCD cameras for imaging, and high quality pure iodine molecular filters for frequency discrimination. Advances made during the development of the Virginia Tech DGV include: high accuracy thermoelectric temperature control for the iodine cells, unique split image camera optics, custom modular enclosures, and single computer-single user operation of the entire system. The following sections detail the design of the Virginia Tech DGV on a subsystem level.

3.1 Laser System

The laser source impacts all aspects of the system design and use. The most fundamental decision is the selection of a continuous wave or pulse laser. Selecting a continuous wave laser, typically argon-ion, results in a highly stable, but low power light source. A recent example of an argon-ion based DGV system is given in Naylor [26]. In that system, the laser achieved a linewidth* of less than $25 MHz$ using an etalon†, but only $1.5 W$ of output power at 514.5 *nm*. Naylor's use of an argon-ion laser also required special provisions for calibrating the iodine cells. This process relies on producing light of varying frequency

*Linewidth is the total frequency range the output light of the laser spans.

†An etalon is used in continuous wave lasers to filter out the unwanted modes (frequencies) generated in the laser cavity

so the resulting transmission curve can be measured. Argon-ion lasers using etalons can only produce frequencies at large intervals, known as mode hops. Mode hops are realized by physically tilting the etalon assembly, or varying its temperature. The resulting iodine cell calibration contains only a few data points and requires accurate curve fitting [26].

Selecting a pulse laser for planar Doppler use yields several advantages over a continuous wave system, but creates a unique set of problems. Pulse lasers have a significant power advantage over continuous wave systems. A continuous wave laser may generate a $1.5\,W$ $514.5nm$ beam, while a typical Nd:YAG pulse laser may have an *average* power of $4\,W$ at 532 nm, but this comparison is misleading. Many Nd:YAG lasers used for planar Doppler velocimetry emit $450mJ$ of energy in bursts lasting less than $10ns$. Dividing the output energy by the pulse duration gives a per-pulse power of $45 \times 10^6 J/s = 45MW$. While this comparison is only approximate, it demonstrates why pulse lasers are preferred in planar Doppler techniques – they deliver high power in a short pulse, allowing a single pulse to illuminate the instantaneous velocity field. Another important feature of an Nd:YAG pulse laser is the ability to continuously tune the laser over a frequency range of 70-80GHz [18]. Frequency adjustments are made by setting a bias voltage on the injection seeder laser inside the host Nd:YAG laser. This ability simplifies the task of iodine cell calibration by allowing continuous frequency adjustment and therefore a well defined transmission line measurement.

The benefits of using a pulse laser, however, do not come without cost. Unlike a continuous wave argon-ion laser, the linewidth of an injection seeded Nd:YAG pulse laser is around 100 MHz. This implies that the output beam from a pulse laser is not as high quality as an argon-ion beam, but yet is still adequate for DGV use [4]. As discussed in Section 2.1.2, pulse lasers also cause laser speckle noise in the data images, and experience random frequency fluctuations. If not accounted for, these phenomena can lead to substantial errors in DGV velocity data [16, 17].

3.1.1 Nd:YAG Laser

When the previous issues of laser selection are compared with the design goal of the Virginia Tech DGV of providing instantaneous velocity measurements over large planar regions, the selection of an Nd:YAG pulse laser is practical. All but three of the systems discussed in Section 2.1.2 used Nd:YAG pulse lasers. The laser used in this research is a GCR-170-10 injection seeded $10Hz$ Nd:YAG pulse laser manufactured by Spectra-Physics Lasers, Inc. It has a fundamental output wavelength of $1064nm$ at an average

power of $8\,W$ with an output linewidth of $100 MHz$[‡]. A harmonic generator unit inside the laser uses a non-linear crystal to produce an output harmonic beam at $532nm$ with a maximum energy per-pulse of $450mJ$. An added feature of this laser is the addition of a computer interface board, a CIM-2, also made by Spectra-Physics. This board mounts in the laser power supply and allows remote control of all laser functions via an RS-232 serial connection.

3.1.2 Laser Frequency Monitoring

As discussed in Section 2.1.2, pulse to pulse variations in laser frequency output can cause substantial errors in DGV velocity data. To combat this source of error, a method of tracking the laser frequency of each pulse must be used. A common method for frequency tracking uses a separate iodine cell system and a photodiode in conjunction with high-speed signal integrators [23]. In this system, a portion of the beam is split off and passed into the tracking system, which records the photodiode intensity measurement for each pulse. During DGV measurements, the photodiode system provides a reference intensity for zero Doppler shift. McKenzie [17, 20] implemented a reference tab system for tracking laser frequency in which a portion of the beam is directed to a tab in the field of view of a receiver camera. This also provides a zero Doppler shifted reference intensity, but does not require an extra iodine cell system or high speed photodiode integrators.

Laser frequency monitoring in the Virginia Tech DGV is performed by using a modified reference tab system. A portion of the laser pulse is directed onto a stationary target within a receiver camera field of view. Another separate indication of the laser pulse frequency is provided by outputs from the Nd:YAG injection seeder laser. Analog voltages are output which indicate the frequency locking performance and the reset state of the seeder system. The frequency locking metric is called the Q-Switch[§] build up time. Low build up times indicate the injection seed laser is locked onto the frequency of the host laser, implying a high probability of locked frequency pulses. The injection seed laser periodically resets in order to acquire a new lock onto the host laser frequency. During this reset time the output pulses are multi-mode and should not be used for data collection.

The laser monitor outputs, together with the reference tab system, comprise a two-level

[‡]Linewidth is related to another common laser parameter named coherence length (l_c) by the relation $l_c = \frac{c}{\Delta v}$ where c is the speed of light and Δv is the linewidth in Hz

[§]The Q-Switch operates like a capacitor for light energy. Emitted energy from the Nd:YAG rods is built up and then released in a $9ns$ pulse. The time required for the energy to reach release level is called the build up time

approach to laser frequency monitoring. As each image is acquired with the Virginia Tech DGV system, the injection seed laser outputs are recorded for that image. Later, during data reduction of the image set, the Q-Switch build up time and reset signals are used to reject images which were acquired with probable multi-mode pulses. Only after passing these two tests is the image processed, at which point the laser reference tab intensity is utilized.

3.1.3 Laser Shutter

The laser used for this DGV system pulses at a rate $10Hz$ but there is a "single shot" mode of operation, whereby the laser restricts beam emission until a trigger is issued. However, this mode produces a beam with unknown frequency characteristics [30]. Therefore, the laser must always be run in pulse mode to ensure stable frequency output. One of the main reasons for selecting an Nd:YAG laser was the ability to illuminate an instantaneous velocity field with a single pulse. This implies that a system is required to allow only a single pulse into the measurement plane at the desired time. The Virginia Tech DGV addresses this problem by using an electronic laser shutter. The shutter, model SES16500/900, is made by JML Optical and has a $25mm$ apperture. A shutter driver/timer unit was purchased with the shutter and contains precision timers for setting of trigger delays and exact shutter exposure times (down to 1 millisecond resolution). Digital lines from the control computer and output triggers from the laser are used to synchronize the shutter/laser system and allow only a single pulse during camera exposure. This shutter system was not designed for use with high power pulse lasers. Over time, laser pulses begin burning through the closed shutter. Shutter life is extended by only blocking the emitted beam a few seconds before and after camera exposure. At all other times the shutter remains open.

3.2 Molecular Filter System

All of the DGV systems reviewed in Section 2.1 use diatomic iodine molecular filters. The filter dimensions vary depending on the type of measurements. Chan [31] presents a detailed investigation of the use of iodine filters for DGV and gives recommendations for the best cell size ranges. He notes that choosing the length of the iodine cell represents a design compromise: longer cell bodies contain more iodine vapor and theoretically perform better, however, practical issues such as minimizing the temperature gradients in the cell body require shorter lengths. Cell lengths in the 4 to $5cm$ range are recommended

for operating temperature ranges of 40-50°C. Chan also discusses the use of a "cold finger" on the iodine cell to simplify the stringent temperature control requirements – setting the stem temperature lower than the main body temperature causes iodine to condense in the stem which sets the vapor pressure of the iodine in the cell. Fixing the vapor pressure determines the absorption characteristics of the cell and makes the cell relatively insensitive to the temperature of the main body [23].

3.2.1 Iodine Cell

The molecular iodine filter used in the Virginia Tech DGV was selected based on the experiences of previous researchers and recommendations of Chan [31]. The filter, manufactured by Opthos Instruments, has a 5.08 cm long cylindrical main body capped on either end with $\frac{1}{4}$ wave flat[¶] 5.08 cm diameter windows. Protruding from the center of the main body is a hollow stem approximately 7 cm in length. The iodine cell is completely sealed and contains 99.9% pure diatomic iodine vapor, with a few crystals of solid iodine. The use of high purity iodine provides the best possible sensitivity for subsonic flow measurements (see Section 1.2.3).

3.2.2 Temperature Control

The use of molecular filters in planar Doppler techniques depends on accurate temperature control. Iodine absorption profiles are a function of the iodine vapor pressure. As previously discussed, the vapor pressure is set by controlling the temperature of the iodine cell stem. Chan [31] shows that 1% stability of the vapor pressure requires 0.04% stability in the temperature of the cell stem. Assuming this level of control on the stem temperature, the main body temperature is much less critical. The main body must simply be maintained at a higher temperature than the stem. This requirement implies the need for two separate zones of control for the iodine cell. The most common method of dual-temperature control uses heat tape around the cell body connected to an electronic controller while the stem temperature is controlled by a high accuracy water bath [23]. An interesting exception to this method was used by Naylor [26]. He used heating elements with a PID[‖] controller around the cell body, but connected the stem to a copper wire "thermal ground". The cell was then allowed to reach equilibrium with the ambient conditions. This system gave stem temperature uncertainty around 0.2°C, due mainly

[¶] A specification for the flatness of a surface in terms of a wavelength of light

[‖] Proportional Integral Derivative

to fluctuations of ambient conditions. Typical uncertainties for water baths systems are quoted as $\pm 0.1°C$ [10].

Body Temperature Control

This research employs a body temperature control scheme similar to methods used in other DGV systems. The body of the iodine cell is wrapped in a heating mat and then mounted into the body housing as shown in Figure 3.1. The body housing is a machined aluminum box with cutouts for the iodine cell windows stem. An RTD** temperature probe, inserted into the body housing, provides feedback to the PID control unit. The body temperature controller is basic PID unit, model Dyna Sense Mk.III, manufactured by Scientific Instruments, Inc. The rated set point stability of this controller is $\pm 1.0°C$.

Stem Temperature Control

Using a water bath system for stem temperature control was considered early in the Virgnia Tech DGV design process. It was felt that a water based system would be too cumbersome and difficult to maintain, therefore a dry system was developed using thermoelectric modules. Thermoelectric modules transfer heat between their surfaces when an electrical current is passed through the core thermocouple material. Heating or cooling is possible by reversing the current flow through the thermoelectric module. Thermoelectrics are often used to cool small electronic devices where electrical power is readily available and small size, low weight, and reliability are important. For iodine cell stem temperature control, we wish to heat the stem to temperatures above ambient.

Figure 3.1 shows the stem housing and the placement of the thermoelectric modules on either side. The stem housing is an single open-ended box made from bent copper sheet. A YSI 400 series thermistor is mounted inside the housing using thermal adhesive pads and a piece of $2cm$ thick high temperature insulation is fit into the open end of the housing. Two thermoelectric modules, Melcor model CP1.0-254-254, are mounted to either side of the housing using thermal adhesive pads. Closed loop operation is achieved using a Wavelength Electronics LFI-3551 Thermoelectric PID temperature controller. This controller provides the power for the thermoelectric modules and accepts feedback from the thermistor. Tests of the stem temperature control system lasting several hours indicate average uncertainty levels of $\pm 0.058°C$ or 0.145% of the $40°C$ set point. This

**Resistive temperature probes with higher accuracy ratings than thermocouples, but slower response times

is almost a factor of two improvement over a water bath system with $\pm 0.1°C$ or 0.25% uncertainty.

3.3 Camera System

There is some debate among DGV researchers about camera selection. The argument exists between groups who use 8 and 10-bit resolution CCD systems and those who invested in scientific grade 14 and 16-bit systems. Meyers [15] in 1998 and Naylor [26] in 1997 used 10 and 8-bit CCD video cameras, respectively, in their research. Naylor achieved 1-2$\frac{m}{s}$ velocity uncertainties in his laboratory wheel and pipe flow measurements, but no uncertainty estimates are available from Meyer's extensive large scale wind tunnel tests. When Meyer describes the camera systems used in his work, emphasis is placed on the "low cost" aspect of the system. Standard CCD video cameras certainly are cost effective, but if the accuracy of the measurements is important, McKenzie [17] has demonstrated that scientific grade cameras give the best results.

Camera lens selection is also important in DGV research. McKenzie [20] recently used lenses with a focal length of $f = 50mm$ and an f/number=1.4 in a series of large scale wind tunnel tests. Use of a large aperture setting (low f/number) allows more light through the lens, allowing acquisition of images in low light conditions. As discussed in Section 2.1.2, larger aperture settings on DGV cameras help reduce the effects of pulse laser speckle. These benefits, however, do not come without a price. Aperture size determines the distance tolerance for acceptable focus of an object, which is called the depth of field [32]. Larger aperture sizes decrease the depth of field which can lead to the problem illustrated in Figure 3.3. DGV systems must view the measurement plane from oblique angles, requiring the depth of field to at least contain the entire plane. Setting a large aperture size may therefore result in poor focus for parts of the measurement plane.

The cameras used in the Virginia Tech DGV were manufactured by Spectra-Source Instruments. All three cameras use an SI502A 512×512 pixel back illuminated CCD array which has a full well potential[††] of more than 350,000 electrons. Each CCD array is cooled to $-16°C$ by means of a thermoelectric module mounted directly to the substrate. The CCD array output is digitized to 16-bit greyscale resolution by a camera control board inside the control computer. The model numbers and the corresponding names of the camera systems are listed in Table 3.1. The reference names given will be used throughout the remainder of this document when referring to the camera systems.

[††]The number of electrons which build up in each CCD element at saturation

Table 3.1: Virginia Tech DGV camera names and model numbers

Reference Name	Model Number
Camera 1	Spectra-Source MCD-1000S
Camera 2	Spectra-Source Orbis 16
Camera 3	Spectra-Source Orbis 16(2)

One of the cameras was tested at NASA Langley by Fleming [33] to determine its performance relative to other camera systems. The results of the test are plotted in Figure 3.2 which shows the Signal-to-Noise Ratio (SNR) of several camera systems versus the illumination level. At lower illumination levels, the Virginia Tech DGV camera achieves a $20dB$ increase in SNR over the lower quality 8-bit camera and $5dB$ increases over the 10 and 12-bit systems. The increased performance at low light levels is critical for acquiring generally low light level DGV image data.

Zoom lenses manufactured by Tamron are mounted to each camera. The lenses have an adjustable focal length of $f = 70 - 210mm$ with a maximum aperture size setting of $f/4$.

3.4 Mounting System

Collecting DGV data requires two images of the laser sheet plane from each viewing angle. The early systems by Komine [11] and Meyers [13] used two cameras for each viewing angle, giving a total of six cameras for a three-component velocity system. A schematic view of the two camera system is shown in Figure 3.4. A non-polarizing beamsplitter sends one image through the iodine filter and into camera 1, while the other image is passed directly into camera 2. This arrangement has the advantage of providing a full image frame for each view, which maximizes the spatial resolution of the system. The main drawback to the two-camera arrangement is the cost of implementation. Meyers [15] recently demonstrated a three-component DGV using a six camera system which was possible due to his use of low cost CCD video cameras digitized at 10-bit resolution.

To make the use of more expensive scientific grade cameras practical for DGV, McKenzie [17] developed and tested the split-image optics camera system shown in Figure 3.5. After passing through a beamsplitter, one image is directed through the iodine cell while the other is passed over a set of mirrors until it is directed back into the same camera. The dashed lines in Figure 3.5 represent the actual width of the image passing though the system and illustrate a problem with this arrangement. After passing through the iodine

cell, the filtered image passes by the corner of the mirror which directs the reference view into the camera. To prevent cutting off portions of the filtered image, a large separation is required between the filtered image and the edge of the reference mirror. Another potential problem is the difference in optical path lengths of the filtered and reference views. McKenzie's test images from this split-image system indicated that only 21% of the total image area was used by the resulting two views. A large portion of the unused image area is caused by the separation between views.

The substantial cost of the 16-bit CCD cameras used in this research necessitated the use of a split-image optics system. Building from the work of McKenzie, a new design for a split-image system was developed. The goals in the new design were the maximization of the usable image area on the CCD array, and maintaining equivalent optical path lengths for each image. A schematic of the new optical design for the Virginia Tech DGV is shown in Figure 3.6. The front collection mirror sends the image down to a mirror which reflects the image at 45° through the beamsplitter. The reference image passes though the beamsplitter while the filtered image is reflected at $-45°$ though the iodine cell. The reference and filtered images then reflect off of mirrors at the corners which send the images towards the center right-angle mirror and then into the camera. This system performs well, utilizing over 70% of the image area, and allows fine adjustment of the positions of each view on the image.

There is little information in the literature relating to the mechanical design of the mounts which hold the cameras and other optics. Meyers [15] and Naylor [26] each show an image of their systems – the foundation of their DGV modules appear to be standard small optical boards approximately $0.3 \times 0.6m$. The beamsplitter and mirrors are mounted to the boards using optical bench post mounts. Optical bench post mounts are designed for rapid adjustment in component position, rather than robustness. A mounting system was designed for the Virginia Tech DGV to provide rigid support for the optics, camera system and iodine cells. A drawing of this system is shown in Figure 3.7. The module frame consists of two plates separated by six aluminum spacer struts. Each component bolts between the two side plates through slots which provide one transverse and one rotational degree of adjustment. This form of two-point mounting is not only rigid, but also protects the equipment from damage. One side plate is machined from Plexiglas sheet, which allows the use of reference marks to aide in angular alignment of the optical components. All electrical connections into the module, for iodine cell temperature control, are made via a 9-pin D-Subminiature plug and an Amphenol 5 pin jack. The matching panel is machined from aluminum sheet and contains a lightening hole cutout. The operating mass for a finished module is approximately $16kg$ $(35lb)$.

A completed Virginia Tech DGV module is shown in Figure 3.8, and a picture of all three

modules is given in Figure 3.9. It should be noted that the modules are shown in their "upright" positions, but all the modules can be mounted or hung in any orientation. The only required modification for non-standard mounting positions is rotation of the camera body.

3.5 Computer System

The computer and related software are the key to integrating all of the previously discussed components into a functioning DGV system. As with the mounting system designs, little information is given in the literature on recent computer and software systems. Once again, however, Meyers [15] and Naylor [26] provide a few details of their computer systems. The system described by Meyers uses five computers, with one of the machines dedicated to synchronizing the other four. This number of computers is partially required due to the use of six camera systems, each requiring a digitizing board. No mention is made of the software used to implement the control over the system. The two-component system described by Naylor is controlled by two linked computers. One of the computers is dedicated to operation of the laser frequency monitoring system, while the other contains the digitizer boards for the two cameras. Naylor provides an overview of the custom software which was written for control of the system and data reduction.

Using a single computer for all required DGV tasks eliminates the problems of synchronizing multiple computers, and makes the system easier to operate. This was possible in the Virginia Tech DGV due to our use of only three cameras and the custom software written to control all system components and reduce the acquired data.

3.5.1 Control Computer

The control computer for the Virginia Tech DGV is an IBM compatible PC with an Intel Pentium $166MHz$ processor and $32MB$ of RAM running Microsoft Windows 95. The current hard disk has a capacity of $2.1GB$. A CD-ROM writer is available for data archiving. The control computer is housed in a wheeled cart which also houses the temperature controllers for the iodine cells as shown in Figure 3.10.

Camera Control Boards

Digitizing boards made by Spectra-Source Instruments were purchased with the three camera systems. Each 16-bit board requires an ISA slot in the control computer. Man-

ufacturer specifications for the boards require their operation in ISA slots with clock speeds not exceeding $11MHz$. This requirement, and the need for multiple ISA slots, has prevented upgrade of the control computer to a newer system. The cameras were purchased over a period of two years, during which time Spectra-Source began producing PCI standard control boards, but PCI boards were not available for the oldest camera. To maintain compatibility with the oldest camera, ISA control boards were purchased with the other two. Interfacing to the camera boards is accomplished using DLL's [‡‡] purchased from the manufacturer.

Data Acquisition Board

A data acquisition (DAQ) board is primarily used to sample the temperature outputs of the stem temperature controllers discussed in Section 3.2.2. The DAQ board also samples voltages from the laser during operation that indicate the quality of the emitted pulses (see Section 3.1.2). The DAQ board used in the Virginia Tech DGV is a 16 channel PCI-DAS1602/16 made by ComputerBoards Inc. The board uses dual $100kHz$ 16-bit analog to digital converters to sample 16 channels in single-ended mode, or 8 channels differentially. One of the analog voltage output connections is used to supply a bias voltage to the laser injection seeder for control of the frequency output. The digital output lines are used to control the shutter for the Nd:YAG laser during image acquisition (see Section 3.1.3). The board also has an external trigger input line, and an input to a digital counter. These inputs are required for synchronizing the DGV system with external events but are not currently used. Operation of all data acquisition board functions is done using a DLL function interface.

Serial Interface

A standard RS-232 serial connection is used to interface with the Nd:YAG laser computer interface module. This connection allows the computer system full control over the laser, including power on/off, emission power settings, and timing adjustments to the laser repetition rate.

[‡‡]Dynamic Link Librarys are pre-compiled Windows functions which can be called by other programming languages

3.5.2 Control Software

The custom software written for the Virginia Tech DGV integrates laser operation, camera control, and iodine cell temperature control into a system operable by a single user. The software was written entirely in C++ using the Microsoft Visual C++ Integrated Development Environment. Writing the DGV control code using the Microsoft Visual Studio enabled use of the Microsoft Foundation Class library, easing many tasks such as user interface design and memory management. However, because the code utilizes so much Microsoft specific code, it is not portable to a non-Windows operating system. Due to other restrictions (specifically the code libraries provided to run the digital cameras) the code will only run on a Windows 95 (or possibly Windows 98) system.

Control of the Virginia Tech DGV hardware for steady data acquisition can be summarized by the diagram shown in Figure 3.11. The diagram shows the signal states of the internal program control triggers for acquiring a single steady DGV data image. The top row of pulses represent the analog triggers from the laser which occur at $10Hz$. When images are not being acquired, the laser shutter is open. On occurrence of a pre-trigger event, the laser shutter is closed. During the pre-trigger delay, the control program samples and stores the temperature data from the iodine cell systems and laser the performance data. After the pre-trigger delay passes, the camera shutters are opened, and the next falling edge of the laser pulse trigger begins the laser shutter delay. After the laser shutter delay, the shutter is opened for $100ms$ passing a single laser pulse. The laser shutter delay is set on the shutter driver/timer unit and must be calibrated such that the shutter opens between laser pulses. After the sequence of events is complete, the control program digitizes the acquired images from each camera, storing them to binary files. If the program is set to acquire multiple images, the process is repeated.

Chapter 4

Image Acquisition & Processing

The acquisition and reduction of DGV images into velocity data is a complex process which has evolved along with the improvements made in system designs. The original DGV system tested by Komine [11] was entirely analog. The filtered and reference views from each analog video camera pair were divided at a rate of 30 frames-per-second by a divider circuit. This system lacked the ability to correct images for misalignment or geometric distortion. In 1991, Meyers and Komine [12] worked on a one component DGV and introduced the methods of digitizing the camera frames for later processing. This technique was much slower than the analog system, but the digital processing methods used to reduce the image data resulted in more accurate velocity data. Since that time, almost all DGV systems have used the techniques outlined by Meyers [34]. This chapter describes the techniques used in the Virginia Tech DGV to acquire images and reduce them into velocity data. All of the methods discussed are implemented in the Virginia Tech DGV control program as part of the automated image collection and reduction routines.

4.1 Acquiring Images

The most fundamental requirement for any DGV system is the ability to simultaneously acquire images from all system cameras. The definition of "simultaneous," however, is dependent on the system configuration. DGV systems using continuous wave lasers require exact camera synchronization so that each image represents the same moment in time. The use of a pulse laser in the Virginia Tech DGV system eliminates the need for precise camera synchronization: allowing only a single laser pulse to illuminate the image plane means that all the cameras must simply be open so that the same pulse is

recorded in each frame. However, the control program operates the cameras in a software synchronized mode. This is to ensure that all cameras remain open for the same exposure time, to within a tolerance of $\pm 20ms$*. The diagram in Figure 4.1 shows the sequence for acquiring a single laser pulse image. At the beginning of the cycle all camera shutters are opened and the CCD arrays begin integrating†. After a laser trigger delay time, a laser pulse is allowed, the cameras stop integrating and the shutters are closed. An optional step involves setting a new laser frequency bias voltage (see Section 3.1). This is performed only during iodine cell calibration to increment the laser output frequency. At all other times the bias voltage is held constant.

The DGV control software automates the process of image acquisition. After setting the required parameters of camera exposure time, number of images to acquire, and relevant file settings, the program automatically captures the designated number of images. After acquiring multiple images, the operator has the option to average the image set and calculate the standard deviations. The acquired images, or the averages, are then displayed for inspection. Before proceeding with the average calculation, or any other routine which operates on a sequence of images, the operator can quickly examine all images in the set and exclude any image from processing.

4.2 Image Processing

The technique of DGV relies on calculating the ratio of reference and iodine cell filtered views. These ratios are then related to Doppler shift at each pixel, and then to the velocity. Before reaching this step, however, a significant number of image processing steps are needed. The following sections detail the image processing requirements for reduction of DGV velocity data.

4.2.1 Geometric Correction

Reduction of DGV data requires the overlay of multiple views of the measurement plane as viewed from each camera. The first step in the alignment process is acquiring images of a dot grid, placed in the desired measurement plane, from each camera system. Each camera's image shows a different perspective projection of the alignment grid. Before the views from the camera system can be aligned, the perspective distortion must be

*The time tolerance is caused by the Windows operating system, which creates timing lags and prevents more accurate synchronization

†CCD integration is the process of allowing charge to build up in the array in response to light levels

corrected. This distortion is shown in the pictures of the alignment dot grid taken during the wind tunnel testing of this DGV system, in Figures 4.5-4.7(a) and the corrected views are shown in Figures 4.5-4.7(b)[‡]. In these example images, the bottom view of the alignment grid is the iodine cell filtered view while the top view is reference. In the Camera 1 and 2 images, the filtered views have been vertically mirrored. The Camera 3 image shows the original inverted orientation of the filtered view.

Perspective distortion is removed from a digital image by the process of warping, or mapping. The techniques used in this research are based on methods from Wolberg [35]. The correction of images for planar perspective distortion begins by defining a non-linear mapping function which relates coordinates between the warped and dewarped views. These mapping functions are written as

$$x = a_{11}u + a_{21}v + a_{31} - a_{13}ux - a_{23}vx \tag{4.1a}$$

$$y = a_{12}u + a_{22}v + a_{32} - a_{13}uy - a_{23}vy \tag{4.1b}$$

where (x, y) are the coordinates in the warped view, (u, v) are the coordinates in the dewarped view, and a_{ij} are the mapping coefficients. Applying Equations 4.1b and 4.1b to four points in the warped and dewarped views results in an 8×8 system of equations which is solved for the unknown mapping coefficients.

The control program performs the dewarping of data images based on four control points selected from the alignment dot grid and the rectangular corner points of the processing region. The mapping coefficients are solved by mapping the warped control points to the corners of a user specified processing rectangle, named a Region of Interest (ROI). All other points inside the ROI are dewarped using the same mapping coefficients. The dewarped views of the alignment dot grid are shown in Figures 4.5-4.7(b). Note how the warped views are mapped to the same size rectangular ROI. After dewarping, the views are all aligned to within an estimated ± 0.25 pixel accuracy. Accurate alignment of the views is important so that each dewarped pixel represents the same spatial coordinate. However, recently McKenzie [20] demonstrated that highly sub-pixel accurate alignment processes are less important when low-pass filtering the image data.

In general the dewarped coordinates (u, v) calculated for a warped image point (x, y) will not be integer values. However, image coordinates are defined to exist only as integer values. There are two methods for dealing with this situation: one, the calculated coordinates can simply be truncated to the nearest integer value, and two, an interpolation

[‡]These images, and all other presented raw camera images, are colorized versions of the actual greyscale images. This improves the visual contrast of low light level images.

scheme can be employed which calculates a new brightness level for the nearest integer pixel coordinate. The Virginia Tech DGV control program employs a bilinear interpolation scheme from Lindley [36]. This method uses the four pixel values surrounding the warped image point to interpolate a new pixel value for the nearest integer address pixel in the dewarped image.

4.2.2 Correction Images

In addition to the geometric corrections made to DGV images, a series of correction images are acquired which compensate for a range of image defects. Pixel sensitivity images equalize the response characteristics of the CCD array, while other images correct for background illumination levels and intensity variance between the filtered and reference views.

Pixel Sensitivity

Ideally all elements within a single CCD array have equivalent responses. Therefore if all the elements are exposed to a constant illumination level, each element will measure the same value. In a real CCD array however, element responses are not constant. When viewing normal images the variance is not easily seen, but an image of a uniform illumination level reveals circular patterns of varying sensitivity. This type of variance is easily corrected by calculating a pixel sensitivity factor for each pixel in the CCD array. Calculation of this factor is made by removing the camera lens and acquiring sequences of images at two illumination levels. The images from the each level are averaged, and the pixel sensitivity factor is calculated for each CCD element according to Equation 4.2:

$$PS_{ij} = \frac{P^1_{ij} - P^2_{ij}}{L_1 - L_2} \tag{4.2}$$

Where PS_{ij} is the factor for the CCD element at row i column j, $P^1_{i,j}$ is the pixel value in the higher illumination level image, $P^2_{i,j}$ the lower level pixel value, and L_1 and L_2 are the average greyscale pixel levels in the two images. This equation represents the slope of a line passing through the two pixel values for each CCD element. The resulting array of floating point values can then be divided into subsequent images to remove the effects of variable pixel sensitivity. Examples of the effectiveness of this technique are shown in Figure 4.4. The curved lines represent the original pixel values in horizontal and vertical cuts across the image for a uniform illumination level of 75% full scale. Dividing image values by the pixel sensitivity matrix flattens the response considerably, reducing the

standard deviations for the two cross sections from almost 1500 counts[§] to less than 65. Calculating and storing the pixel sensitivity matrix is only done once for each camera. The sensitivity variations are inherent to the CCD sensor and do not change in time.

The DGV control program simplifies the task of determining the pixel sensitivity matrix for each camera. The program acquires and averages the images for the two light levels, and calculates the sensitivity factor for each element, storing the result in a floating point binary correction file for later use. After specifying the sensitivity correction file names for each camera, the program can then automatically apply the correction during the data reduction process.

Background

Background images are acquired before each set of data images to record the ambient illumination levels. These images are then directly subtracted from subsequent data images. Even under conditions of apparent total darkness, in a few seconds the CCD arrays used in the Virginia Tech DGV system can accumulate 1000 counts out of a possible 65535. Subtracting the background image helps minimize bias error in the final velocity calculations.

White Card Ratio

White card image correction is similar to pixel sensitivity correction. However, the white card ratio correction is used to equalize the slight differences in illumination levels between the filtered and reference camera views. A large contributor to these differences is the molecular iodine cell. The filtered image passes through the windows of the cell, which causes losses in intensity. The white card ratio correction is applied so that the filtered and reference images of the laser plane have equivalent brightness levels *when the laser is set to a full transmission frequency.*

The white card ratio is calculated from an image of a uniform white card illuminated by a laser pulse. Dividing a filtered view pixel by the corresponding reference view pixel gives a floating point value which should ideally be equal to 1.0. The floating point division values are stored in binary files which are read by the control program during the data reduction process.

[§]A digitized monochrome image is represented by an array of 16-bit unsigned integers with brightness values from 0 (black) to 65535 (white) counts

4.2.3 Image Filtering

Filtering acquired images is necessary to reduce the effects of laser speckle and it improves reduced data quality by reducing the effects of small view alignment errors [20]. Image processing filters are an area process called a convolution. The resulting filtered pixel is a function of the pixels contained in the filter's kernel[¶]. Large kernels result in highly smoothed images, but sacrifice spatial resolution. McKenzie [20] recommends a minimum 3×3 pixel kernel and a linear low pass filter with the convolution kernel with all elements equal to $\frac{1}{9}$. This filter is applied by multiplying each pixel in the neighborhood by the corresponding convolution kernel value and placing the sum of those values in the center pixel. The Virginia Tech DGV control program implements low-pass filtering using an algorithm from Lindley [36]. For completeness, the program also includes two other low-pass convolution kernels and a median filter algorithm. However, only the recommended low-pass filter is used during DGV data reduction.

Low pass filtering of the image data relaxes the constraint on reference and filtered view alignment. McKenzie [20] states that sub-pixel accurate view alignment is not required when using 3×3 and larger filter kernels. This is due to the decrease of spatial resolution after filtering. He also maintains that using kernels as large as 5×5 causes no significant loss of velocity information and further improves the velocity data quality.

4.2.4 Other Functions

Common functions for image arithmetic are also required for DGV data reduction. The control program implements subtraction and division of images or selected regions. The subtraction routine is used for background image correction, while division is used for the pixel sensitivity and white card ratio corrections. An important function used during data reduction is image mirroring. The control program can perform horizontal or vertical mirrors of any selected region of the image; all filtered views from the DGV cameras must be vertically mirrored to orient them correctly for data reduction. The beam splitter in the split-image optics flips the filtered image upside down. This is shown in Figure 4.7.

4.3 Reduction of DGV Data

The operations discussed in the preceding sections, combined with an iodine cell calibration, are used to produce reduced DGV velocity data from raw images. The steps for

[¶]A convolution kernel defines the size of the filter neighborhood, e.g. 3×3 or 5×5 pixels

acquiring and reducing DGV velocity data are summarized in Figures 4.2 and 4.3. All of the steps in Figure 4.2 must be completed prior to the acquisition of DGV velocity images. One of the most important steps is the calibration of the iodine cell transmission function. An accurate determination of the absorption profile is essential for velocity calculations.

4.3.1 Iodine Cell Calibration

Calibration of the iodine cells is required to define the transmission properties of the cell as a function of frequency. Acquiring calibration data is similar to acquisition of normal pulse illuminated images, but an extra step is added for adjusting the laser output frequency (see Section 4.1). Each acquired image contains a reference and filtered view of the white card at set frequency increments.

Acquisition and reduction of calibration data is performed automatically by the Virginia Tech DGV control program. The parameters for the calibration include exposure time, number of calibration images, and the frequency voltage range output to the laser injection seeder. After each image is stored, the frequency bias voltage is incremented to the next value, and a time delay occurs to allow the laser to lock onto the next frequency. Typical calibration sets consist of 100-200 images and require approximately 45-90 minutes to acquire. Processed calibration data give the transmission of the iodine cell as a function of the laser frequency voltage. For this reason, longer scans, of up to 600 images, were also acquired in order to reveal a series of several absorption lines. By comparing the experimental transmission lines to a computer model, the proper scaling of the voltage axis into relative frequency is determined.

Calibration Data Reduction

Reducing the acquired calibration images into transmission line data is a similar process to the reduction of a DGV velocity data set (Figure 4.3). Each image is corrected for background light levels, pixel sensitivity, and is low pass filtered. The separated views are then dewarped, aligned and divided. The process then skips directly to the white card ratio correction, and the average ratio value of the matrix is stored as the transmission ratio. Images which did not pass the laser monitoring criteria discussed in Section 3.1.2 are not processed.

Iodine Cell Computational Model

Forkey *et al.* [37] developed a computer program to predict the transmission properties of diatomic iodine molecular filters. Example output from the model is shown in Figure 1.1. The model predicts the transmission properties of iodine cell based on temperature and partial pressure, as well as the physical characteristics of the cell. The lines shown are numbered 16 and 17 in [37]; the lower frequency side of line 17 was used for the tests of the Virginia Tech DGV.

Figure 4.8 shows the match of an experimental transmission curve to the predicted model output. The experimental data matches the model output well, except for the points near the top of the curve. This discrepancy was also encountered by Forkey, as shown in Figure 4.9. The experimental points near the bottom of the curve are in error due to subtraction of the background images from the calibration data set: at very low transmission levels, the pixel values in the filtered view are of the same order as the background light levels. Since neither the top or very bottom portions of the absorption lines are used for normal data reduction, these errors in the calibration data are not critical,

Frequency Calibration Function Curve Fit

The goal of the iodine cell calibration process is to provide a functional relationship between transmission ratio and frequency. Naylor [26] fit his experimental calibration curve with a Boltzman fitting function, whose parameters were determined by a non-linear optimization scheme. McKenzie [20] used a computational model he developed for prediction of iodine absorption lines, and optimized the calculated response to fit the calibration data.

The system currently employed in the Virginia Tech DGV is based on the computational model of Forkey. Velocity measurements are made first by tuning the laser frequency to a middle transmission ratio point on the absorption line, then measuring Doppler shifts above or below that set frequency. Thus, only the highly sloped portion of the absorption profile is needed for velocity calculations. A plot of this region is shown in Figure 4.10. The plot shows the experimental profile data, the model prediction, and several polynomial curve fits to the model profile.

The predicted model in Figure 4.10 falls within the uncertainty bounds of the experimental transmission points. Therefore, curve fits to the model output are used in the Virginia Tech DGV. The first order fit is shown to emphasize the non-linearity of the absorption line. It is interesting to note that the early DGV system of Komine [11] used a linear fit

for a calibration function. The 5^{th} order polynomial fit is used in the current research as it provided the best fit for the fewest parameters, and is shown in Figure 4.11. Note the model output and curve fit in Figure 4.11 are plotted inverted relative to the other absorption plots; this yields a polynomial fit function which returns the frequency value for a given transmission ratio. Currently the same curve fit is used for the all three iodine cells. This was made possible by the excellent performance of the iodine cell temperature controllers, which maintained all cells at the same conditions.

Examining the example iodine absorption lines in Figure 1.1 reveals the slopes of line 16 are greater than line 17. The steeper slopes of line 17 would result in improved sensitivity of the DGV system. However, due to laser performance problems which will be discussed in more detail later, repeatable calibration scans of line 17 were not possible – leaving the less sensitive line 16 as the only alternative.

4.3.2 DGV Velocity Calculation

Once the correction images are collected and the iodine are cells calibrated, DGV images of the flow of interest can be acquired. These images are then processed according to the steps shown in Figure 4.3.

The reduction procedure for DGV velocity data is equivalent to the iodine cell calibration reduction procedure up to the ratio step of the filtered and reference views. At this point, the velocity data ratio view is divided by the reference laser transmission ratio, $TR^{LaserRef}$. This ratio is calculated by dividing the current filtered laser intensity by the reference filtered laser intensity. The reference filtered laser intensity is equal to the transmission ratio of the system with the laser tuned to the midpoint of the absorption line. The laser intensity values in the present system are extracted from the reference tab circled in upper right corner of the filtered Camera 1 image shown in Figure 4.5. The laser reference laser transmission ratio is ideally unity. Dividing the ratio image by this value scales the intensity values to the correct level – removing the effect of laser frequency drift. If there are multiple images in the data set, the reduction process is repeated, and the resulting transmission ratios are averaged. Images in a data set which were acquired with multi-mode pulses are not processed. The remaining processing steps include the white card image correction, and then passing each ratio value to the iodine cell calibration function. A required input to the iodine cell calibration function is the reference transmission ratio, TR^{ref}. All frequency shifts are calculated relative to the frequency corresponding to TR^{ref}. Then the iodine calibration routine outputs three matrices of Doppler shift frequencies. Solving the 3 by 3 system shown in Equation A.5 for each triplet of of Doppler shifts yields the three velocity components at each pixel

location.

$$\begin{Bmatrix} V_x \\ V_y \\ V_z \end{Bmatrix} = \lambda \begin{bmatrix} \sin\theta_1 - l_x & -\sin\phi_1\cos\theta_1 - l_y & -\cos\phi_1\cos\theta_1 - l_z \\ \sin\theta_2 - l_x & -\sin\phi_2\cos\theta_2 - l_y & -\cos\phi_2\cos\theta_2 - l_z \\ \sin\theta_3 - l_x & -\sin\phi_3\cos\theta_3 - l_y & -\cos\phi_3\cos\theta_3 - l_z \end{bmatrix}^{-1} \cdot \begin{Bmatrix} \Delta f_1 \\ \Delta f_2 \\ \Delta f_3 \end{Bmatrix} \tag{4.3}$$

A detailed derivation of these velocity equations is given in Appendix A. The angles ϕ_i and θ_i represent 3-2-1 rotation sequence Euler angles, and Δf_i is the Doppler shift frequency. The relative orientation of each receiving camera to the measurement plane determines the required rotation angles which transform between the camera reference frame and the measurement plane. These angles were determined by a camera calibration procedure which is described in Appendix B. It is important to understand that the returned velocity components are relative to a right-hand coordinate system attached to the measurement plane. Transforming the calculated velocity components into another reference frame requires knowledge of the orientation of the measurement plane with respect to the new reference frame. The control program only calculates velocity components in the measurement plane coordinate system. These values are stored to binary files and optionally to ASCII files which can read by commercial graphing programs.

Chapter 5

System Testing

During the development of the Virginia Tech DGV system, each of the components was tested routinely to ensure proper operation. The real test, however, was found in setting up the system to acquire velocity data in the Virginia Tech Stability Wind Tunnel. This full system test had several important goals:

- Setup and verification of full system operation in a wind tunnel test environment
- Calibration of the iodine molecular filters
- Acquisition of three-component planar velocity data in the wake of a 6:1 prolate spheroid model (at $x/L = 0.772$, and 20° angle of attack)

5.1 Experimental Arrangement

Setting up the Virginia Tech DGV system for its first test required several days in order to mount and align the camera modules, set up the laser system and associated optics, and mount the prolate spheroid model inside the wind tunnel test section. The following sections describe the hardware used for the test.

5.1.1 Stability Wind Tunnel

The DGV system was tested in the Virginia Tech Stability Wind Tunnel facility, shown in Figure 5.1. This subsonic continuous return tunnel has a 9:1 contraction ratio with a $1.8 \times 1.8m$ test section, $7.3m$ in length. The tunnel is driven by a $4.37m$ diameter

8 blade prop, powered by a $447kW$ DC motor. Seven turbulence screens, mounted in the settling chamber, help limit the maximum turbulence intensity in the test section to around 0.06%. Top speed in the test section is approximately $80\frac{m}{s}$.

Some modifications were made to the tunnel test section for these tests. New Plexiglas window panels were made to provide optical access from the top and port side of the test section. Also, a hole was cut in a control room floor panel to allow laser access from below the test section.

5.1.2 Prolate Spheriod Model

The prolate spheroid model tested for this experiment was the same model used by Chesnakas and Simpson [2] for acquisition of LDA data in the separated wake region. A diagram of the model is shown in Figure 5.2. The major axis length is $L = 1.37m$, resulting in a maximum diameter of $0.228m$. The aft $38mm$ of the model is removed for sting* mounting hardware. The measurement plane location is at $x/L = 0.772$ ($x = 1.059m$), where x is the coordinate along the axis of the model, starting from the nose. For all tests conducted, the model was mounted at 20.0° angle of attack, which inclined the measurement plane 26.2° from vertical, so that it was perpendicular to the model surface and matched the measurement plane of Chesnakas [2].

5.1.3 Flow Seeding

In the technique of Laser Doppler Anemometry (see Section 1.2.1), flow seeding requirements are stringent. The seed particles must have a uniform small size (typically on the the order of $1\mu m$) and be present in an appropriate concentration. Planar Doppler techniques, however, which rely only on scattered laser light intensity, perform well with much larger particles [26].

Previous DGV research performed in large scale wind tunnels provided some guidance in the selection of a seeding system. Meyers [15] made DGV measurements in the $14 \times 22ft$ subsonic tunnel at NASA Langley using three propylene glycol vaporization/condensation smoke generators mounted on a traverse system in the tunnel settling chamber. McKenzie [20] also used a smoke generator with the same liquid compound in his tests at NASA Ames' National Full Scale Aerodynamic Complex. McKenzie positioned the smoke generator on a lift platform in front of the inlet to the wind tunnel. Neither McKenzie nor

*A sting is a mounting rod which protrudes from a wind tunnel model.

Meyers provide details about seed particle size or concentration. McKenzie, however, discusses the difficulty of obtaining uniform seeding through the measurement plane.

The flow seeding system for the Virginia Tech Stability Tunnel was not available for these tests, therefore a commercial Rosco theatrical smoke machine was used. The machine uses a Rosco proprietary fluid to create a dense white smoke, output at a maximum rate of $0.71\frac{m^3}{s}$ with average particle sizes of 60-70μm. Initially, the smoke was output from the center of the tunnel settling chamber, creating the least interference with the test section flow. However, dispersion of the smoke resulted in a lack of seed in the measurement volume. The smoke output was instead routed through a pipe passed through the ceiling of the test section approximately $4m$ upstream of the model. This arrangement, shown in Figure 5.3, resulted in more uniform seeding of the measurement volume.

5.1.4 DGV System Setup

Approximately one month of tunnel time was available for execution of the first DGV system test. It was clear, given the broad objectives of this first test, that only one possible DGV camera configuration could be tested. Determining the best camera positions for future use will require a systematic series of measurements and analysis of the acquired data. Other features of the setup, such as the laser position and operator console position, are not as variable. The following sections describe the setup procedures for the DGV system.

Camera Module Mounting

A diagram of the tested camera module configuration is shown in Figure 5.4. All three modules were mounted to heavy duty camera tripods, and positioned around the test section. Camera module 1 was positioned in the control room at a highly oblique angle to the measurement plane – to increase its sensitivity to the transverse component of velocity. Module 2 views the plane from a more shallow angle,which improves measurement of the streamwise component, and was located on the far side of the test section. Modules 1 and 2 were mounted at approximately the same height above the tunnel floor. Camera module 3 was mounted on top of the test section, looking down through a Plexiglas window. The tilted view from above the plane made module 3 sensitive to the vertical component of velocity. A photograph of this arrangement is shown in Figure 5.5. Note that camera module 2 is visible through the far test section wall window.

Alignment Tripod

An aluminum plate mounted on a tripod inside the test section was used to facilitate the alignment and focusing of all cameras onto the measurement plane. The position of the plate was determined by transferring reference points from the mounted prolate spheroid model to the tunnel floor with a plumb bob. The plate was then adjusted to an inclination angle of $26.2° \pm 0.1°$ from vertical using a Lucas Instruments digital inclinometer. The plane was set perpendicular to the tunnel side walls using the laser as a reference. Firing the laser (at a low power setting) through the Plexiglas window, then to a mirror mounted on the opposite wall, produced two back reflections. By adjusting the laser mirror, the back reflections could be aligned with the main beam, giving an excellent perpendicular reference beam. The estimated angular uncertainty using this method was $\pm 0.2°$. Once the position and angular alignment were complete, mounting holes were drilled through the tripod feet and into the tunnel floor. This allowed for repeatable repositioning of the plate throughout the testing process.

Laser & Optics

The space available in the elevated control room of the Stability Tunnel is limited. Proper laser and optics placement was critical for space and safety considerations. The sensitive nature of the Nd:YAG laser was also a factor. Meyers [15] experienced poor laser performance due to excessive vibration and temperature changes inside the wind tunnel test section. For these tests, the laser would not be mounted inside the test section, but the elevated control room experiences vibration and temperature variations during operation. Therefore, a mounting plan which placed the laser below the test section on the balance platform was tested. The balance platform was originally used as a base for the large mechanical force and moment balance used during the tunnel's early history. It rests on the concrete foundation of the wind tunnel control room, and is an ideal platform for sensitive equipment. A picture of the mounted laser system is shown in Figure 5.6. The laser head rests on an optical table, along with the laser shutter and the primary mirror. The primary mirror reflects the beam up through an access hole in the control room floor. All mirrors used in the DGV laser optics are made by Melles-Griot (model 16MFB153) and are tailored for use with high power Nd:YAG lasers. Their custom hard coatings are optimized for the Nd:YAG wavelength range and for reflection angles of 45°.

After entering the control room vertically, the laser beam is reflected back to horizontal by a periscope assembly. The periscope then directs the beam to the reference, laser sheet and cone optics. A diagram of this optical system is shown in Figure 5.7 and a picture is shown in Figure 5.8.

Before reaching the top mirror of the periscope, the beam passes though a 1% neutral density filter[†]. The small reflection from this filter is directed through additional neutral density filters, and then to a mirror which reflects the beam onto the laser reference tab (see Figures 5.7 and 5.8). The tab was placed inside the field of view of camera module 1, and the laser reference spot is visible in Figure 4.5.

The laser cone optics are used during the dot grid alignment process and during iodine cell calibration. The cone optics pass the beam through a convex lens, creating a cone of light to illuminate the tripod-mounted alignment plate. The components of the cone optics are listed in Table 5.1.

Table 5.1: Components list for the laser cone optics

Manufacturer	**Model**	**Description**
Melles-Griot	16MFB153	$25mm$ diameter Nd:YAG steering mirror (523-532nm)
Oriel	71594	$25mm$ diameter plano-convex lens

Traversing the cone optics mirror out of the beam path allows the beam to enter the laser sheet optics. A mirror directs the incoming beam through a convex lens and then through a cylindrical lens which creates the laser sheet. The distance between the convex lens and the cylindrical lens was adjusted to yield the minimum thickness laser sheet (approximately $2mm$ in the measurement plane). A list of the components in the laser sheet optics is given in Table 5.2. The sheet optics are attached to a vertically mounted milling machine rotary table. Use of a rotary table enabled precise alignment of the laser sheet at 26.2° from vertical (see Figure 5.2). Pictures of the laser sheet optics while in use are shown in Figures 5.9 and 5.10. It is important to note that all stray laser reflections were contained by beam stops and laser safety screens around the optics table.

[†]Neutral density filters uniformly attenuate incoming light and are rated by the percentage of light blocked (reflected)

Table 5.2: Components list for the laser sheet optics

Manufacturer	Model	Description
Melles-Griot	16MFB153	$25mm$ diameter Nd:YAG steering mirror (523-532nm)
Melles-Griot	01LPX106	$25mm$ diameter plano-convex lens
Unknown	Unknown	$70 \times 56 \times 13mm$ cylindrical lens

Control Console

The control cart for the DGV system, shown in Figure 3.10, was located on the lower level of the tunnel control room. This position for the operator was selected for reasons of safety and convenience. All aspects of the DGV operation are controlled by the operator from the control computer; cables are run from the control console to the three cameras, to the iodine cell modules and to the laser/shutter system. This allows the operator to run the system without the dangers of being near the Nd:YAG laser beam. During measurements taken with the tunnel running, a tunnel operator wearing laser safety goggles sets the tunnel speed using the upstairs control panel and operates the smoke generator.

5.2 Experimental Procedures

Once all of the equipment was in position, the first major test performed measured the sensitivity of the Virgnia Tech DGV to tunnel test section vibration. Subsequent tests collected iodine cell calibration data, and finally flow velocity images in the wake of the 6:1 prolate spheroid model. The following sections detail the procedures used during these tests.

5.2.1 Vibration Test

The DGV modules are mounted to tripods which are located around and on top of the tunnel test section. All the modules are therefore subject to the vibrations of the tunnel test section during wind-on testing. To measure the effects of these vibrations, a series of tests were performed which used the prolate spheroid model for reference.The model

was mounted to a strut which in turn was clamped to a mounting frame below the test section. The frame is another part of the original mechanical balance system and is mounted to the balance platform.

A paper card, printed with black target dots, was attached to the back of the model such that it was imaged by each of the cameras. The overhead lights were used to illuminate the target while images were acquired at tunnel dynamic pressures of 0 to $1.5kPa$ (0 to $6inH_2O$) in $0.1kPa$ ($0.5inH_2O$) increments. Fifteen images were taken at each tunnel speed setting.

5.2.2 Iodine Cell Calibration

The tripod mounted plate used to display the alignment dot grid (see Figure 5.7), was also used as a mount for a blank white card. This card served as the imaging target during the iodine cell calibration process discussed in Section 4.3.1.

A calibration procedure began with warming up the laser system for least 30 minutes. During the warm up time, the laser optics were configured for a calibration scan. Before adjusting the optics, the laser beam was blocked by a piece of wood placed over the laser access hole in the control room floor. Then the cone mirror was translated to the full back position, so that it would reflect the top beam leaving the laser periscope into the convex lens.

Once the optics were properly set, all lights were switched off and background images were acquired from all cameras. The wood block was removed, and the operator began the automated calibration image acquisition process. After the calibration scan, the reduced calibration data were stored, and images of the white card at full transmission laser frequency were acquired for use in the white card ratio correction discussed in Section 4.2.2. The laser tuning frequency was then selected from the calibration results, and the corresponding voltage bias was set. Images of the white card were acquired at the laser set point frequency to record the reference transmission ratio (TR^{ref} in Section 4.3.2). The laser was then blocked, and the optics set for acquisition of DGV velocity images.

5.2.3 Prolate Spheroid Data Acquisition

During attempts at acquiring velocity data, it was determined that the output volume from the smoke generator was not sufficient to allow acquisition of single pulse illuminated flow images – the low density of smoke in the measurement plane did not scatter enough

light from a single pulse to register on the camera images. No sources of additional smoke were available, so the procedure for acquiring velocity data images was modified to allow multiple pulses to illuminate each image. The laser shutter was latched open, allowing all laser pulses into the test section. Even with this method, camera exposure times of 3 seconds (30 pulses per image) were required to register adequate illumination in the images.

An important side effect of the multiple pulse images was the loss of the laser reference intensity. Allowing multiple pulses overexposed the reference beam spot on the Camera 1 images, so the reference beam had to be blocked during velocity data acquisition. This eliminated the only per-pulse laser frequency information in the DGV system and the ability to correct for laser frequency drift.

To promote stable laser frequency output, the laser was not switched off between the calibration scan and velocity data acquisition. The beam was blocked, and the cone mirror moved out of the main beam path. The tripod was then removed from the tunnel, and the prolate spheroid model was mounted to the test section strut at 20° angle of attack (shown in Figure 5.2). Next, the laser shutter was latched open and the tunnel speed set. The smoke generator was activated, and a series of velocity data images were acquired at tunnel free stream speeds of 32.4, 35.5, and 38.3$\frac{m}{s}$. After the velocity image acquisition, the tunnel was shut down and a another calibration scan performed. This scan provided a check on the stability of the laser and iodine cells during the test.

5.3 Experimental Results

Following initial setup, testing of the DGV system took place in three phases: the first involved testing the system for vibration effects at increasing tunnel speeds; the second, calibration of the iodine cell molecular filters for each module; and the third, acquisition of flow velocity data over the 6:1 prolate spheroid model. Testing the system for vibration sensitivity was imperative to prove the adequacy of the tripod mounting scheme for the DGV modules. The calibration phase of the testing verified the ability of the system to discriminate frequency shifts. This proved the system's ability to make planar velocity measurements. However, attempts to collect accurate velocity data in the prolate spheroid wake were not successful. A combination of equipment failures and inadequate flow seeding produced velocity measurements with unacceptable uncertainties.

5.3.1 Vibration Test Results

Images from the vibration test were used to track the centroids of a selected target dot throughout the tunnel speed range. The centroid locations for the 15 images at each tunnel speed were then tabulated for analysis. Results of the vibration tests are plotted in Figure 5.11. The vertical axis represents the percentage deviation of the centroid point for the target dot from its zero tunnel speed value. The error bars at each point represent the standard deviation of the 15 point measurements at each tunnel speed. In terms of pixels, the centroid location uncertainties over the entire speed range are 1.76, 2.86, and 2.86 pixels, for camera modules 1, 2 and 3 respectively. The larger uncertainties of the Camera 2 and 3 data are reasonable, considering their direct mounting on the wind tunnel test section. However, the increasing trend of the centroid location movement, and the generally small standard deviations at each tunnel speed, can be explained by flexing of the model sting and strut system. If the bulk of the uncertainty is attributed to model flex, a more realistic uncertainty estimate of less than 1 pixel for all cameras is achieved. This uncertainty, however, does not affect the processed data, due to the blurring effects of image low-pass filtering (see Section 4.2.3).

Two issues not directly addressed by the vibration tests are the flexibility of the control room and the test section floor panels. The tripod for Camera 1 partially rested on removable wooden floor panels in the control room. These panels are designed to be taken out when other Stability Wind Tunnel test sections are installed, and thus are not rigidly connected to the control room floor or the tunnel test section. Walking across the floor panels produced marked vertical deflection of the tripod. Another floor flexibility consideration is caused by the tunnel test section steel panels. The panels bowed in when walked on, which affected the position of the alignment tripod. The main issue in both cases is the likelihood that the flexed floor panels do not always return to the exact same shape, thereby creating positional errors in the camera images. This problem is only averted by carefully monitoring the dot card grid positions before and after calibration runs. By tracking the reference points, at least some positional error can be accounted for and corrected.

5.3.2 Calibration Results

Some calibration results have been previously discussed in Section 4.3.1. These results were obtained on the last day of testing, immediately before acquiring velocity data sets in the prolate spheroid wake. Before that time, however, many other calibrations were performed and the performance of the system was evaluated.

Absorption Line Identification

Calibration data is based on incrementing the frequency bias voltage of the injection seeder laser (see Section 3.1). Thus, calibration curves are initially obtained only as a function of frequency bias voltage. A voltage to frequency conversion is needed to match the collected calibration data to the computational model. To accomplish this, several scans were performed over large frequency ranges. These large frequency scans identified multiple absorption lines for comparison and matching with the computational model. An example of such a scan is shown in Figure 5.12. This calibration data set was compared with the model output data shown in Figure 1.1 to identify the measured absorption lines. Note, however, that in the experimental data set, increasing the bias voltage to the injection seed laser *decreased* the frequency of the output beam. The two curves shown for cameras 1 and 3 data represent the raw calibration data and the data as filtered for laser performance. The laser performance criteria are discussed in Section 3.1.2 and consist of the Q-switch build up time voltage and the reset state of the injection seed laser. The lower plot in Figure 5.12 shows the sampled laser Q-switch build up time voltage for each acquired image in the calibration scan. The spikes in the build up time correlate well with the points in the calibration curve which were removed by the laser performance filtering process.

Laser Performance

Inconsistencies in the performance of the Nd:YAG laser system created difficulties in system operation and data reduction. The frequency locking ability of the laser varied on a daily basis. On some days the laser locked frequency well and the acquired calibration data contained relatively few rejected points. Such was the case on the day the calibration scan shown in Figure 5.12 was acquired, which lost only 20% of the acquired data points. However, on the final day of tunnel testing, the laser was not locking frequency well. The calibration scan in Figure 5.13 was taken immediately before acquiring velocity data images over the prolate spheroid model. The scan shown in Figure 5.14 was acquired after the last set of velocity images, not more than 30 minutes after the previous scan. Degradation of the laser frequency locking performance is evident. Over half of the last calibration scan points were rejected by the laser performance filter, compared to 37% rejection in the first calibration set. Only calibration data from Camera 1 is shown for comparison due to unexplained overexposure of the Camera 3 images in the final calibration scan. The lack of calibration data from the Camera 2 module is discussed in the following section.

Camera Performance

Throughout the development process of the Virginia Tech DGV, the camera systems have functioned well. However, before setting up the DGV in the Stability Wind Tunnel, Camera 2 began to malfunction. The problem occurred after the camera was in operation for more than approximately 10 minutes. After this time, the acquired images became washed out and did not contain brightness levels below 30,000 counts. This effectively halved the resolution of the camera and prevented the accurate imaging of low light levels. The decision to proceed with the system test was made based on the nature of the problem: the Camera 2 output appeared normal prior to the images washing out. Therefore, Camera 2 was only turned on during velocity data acquisition, and then only for a few minutes at a time. All three cameras use the same CCD array and have equivalent electronics. Thus, it was assumed that calibration data acquired from Cameras 1 and 3 was also valid for Camera 2. The key to the accuracy of this assumption was the performance of the iodine cell temperature controllers.

Temperature Control Performance

The extensive calibration and system tests performed during the tunnel entry thoroughly tested the performance of the iodine cell temperature control systems. The air exchange tower of the Stability Tunnel (see Figure 5.1) fixes the tunnel stagnation pressure at atmospheric, but it also exposes the tunnel flow to outside air temperature fluctuations. These temperature changes are also felt inside the control room. Over a day of testing, the control room temperature can vary $10°C$ or more. The iodine cell temperature control systems coped with these temperature changes extremely well. An example of the stem temperature control performance is shown in Figure 5.15. This data was acquired during a 600 image calibration scan, which lasted over three hours. Uncertainty values for a 95% confidence level are 0.055, 0.041, and $0.079°C$ for modules 1,2 and 3 respectively. It is likely that most of the calculated uncertainties are due to electrical noise in the temperature controller feedbacks. Also note that all three stem temperatures were maintained within a $0.25°C$ band. A low amplitude oscillation is present in the module 3 feedback data, which accounts for its higher uncertainty. This oscillation is likely due to the proximity of module 3 to the air conditioner vents for the upstairs control room.

5.3.3 Prolate Spheroid Results

Velocity data images in the wake of the prolate spheroid flow could not be acquired until the final day of the wind tunnel testing. As discussed in the previous sections, the laser performance on that day was not optimal, and the performance of Camera 2 was marginal. Despite these difficulties, the full procedure for acquiring velocity images was performed and a series of flow images acquired.

Flow Images

The raw flow images for a tunnel speed of $32.4\frac{m}{s}$ are shown in Figures 5.16-5.18(a)[‡]. The shed vortices over the prolate spheroid are clearly visible in the Camera 2 images. The images from the other cameras are not as bright, but also show views of the vortex system. Longer exposure times were tested to increase the brightness levels of the Camera 1 and 3 images, but resulted in severe overexposure of the the Camera 2 images. The dewarped views of the measurement plane are shown in Figures 5.16-5.18(b). These images show the alignment of the views resulting from the dewarping procedure. Compared to the data acquired by Chesnakas [2], the vortex locations and the general flow structures appear consistent.

Velocity Data

Following the procedure described in Section 4.3, the acquired images were processed into velocity data. However, due to the multiple laser pulses contained in each image, critical information was lost. Each data image contained the average image of 30 laser pulses, with no information on per-pulse laser frequency. The only frequency information available was the Q-switch build up time voltage, which only provides an estimate of the quality of the emitted pulses. Out of the fifteen images acquired at each tunnel speed, only seven of the lowest speed data set appeared to be viable.

Attempts at processing the images separately, or as an average set produced different results. None of the processing schemes, however, resulted in velocity data which was comparable to the data set obtained by Chesnakas. An example plot of the calculated velocity values is shown in Figure 5.19. Calculating the uncertainties of the image data revealed high values throughout the velocity data. These values are plotted in Figure 5.21, and are lowest near the center of the image, but still near the magnitude of the free stream

[‡]The image color scheme of blue→green→yellow→red represents the increasing greyscale values of the pixels from black to white.

velocity. Towards the outer parts of the image, where flow seeding levels were much lower, the uncertainties are higher. The calculation of the plotted uncertainties is discussed in Section C.1.

Another attempted method of data reduction processed the images *without* applying the coordinate transformation used to derive Equation 4.3. Without the transformation, each DGV module measures a velocity component in the direction defined by the vector difference $\bar{o} - \bar{l}$ (see Figure A.1). This removes the simultaneous solution requirement for velocity, but results in non-orthogonal components. However, since the transformation matrix between the image planes and the measurement plane was known, velocity components from data of Chesnakas [2] were transformed into the coordinate system for each camera. The results did not produce quantitative correlation between the data sets, but demonstrated an alternative method for analyzing DGV data. The results from processing the Camera 3 data in this manner are plotted in Figure 5.20. The velocity contours appear to capture more detail of the flow structures than the results shown in Figure 5.19. This method allows processing of images from a single camera into velocity data and may prove useful in the future.

The predominate source of uncertainty in the acquired data set is the variance of the brightness levels between images. This variance led to large uncertainties in transmission ratios between images. The importance of these transmission ratio variances is detailed in Section C.2. Images from Camera 2 contained the highest levels of transmission ratio uncertainty. The images from Cameras 1 and 3 contained approximately half the Camera 2 levels of uncertainty, however, as shown in Section C.2.5 the uncertainty levels were still unacceptable.

Chapter 6

Conclusions & Recommendations

A new laser based flow interrogation system, capable of simultaneous measurement of planar three-component velocity data, was constructed and tested. The Virginia Tech Doppler Global Velocimeter (DGV) system was designed for use in the Virginia Tech Stability Wind Tunnel as a tool for investigating complex three-dimensional separated flow regions. A series of tests in the Stability Tunnel were conducted to determine the suitability of the new DGV system for this task. Extensive calibration tests proved the system is capable of measuring the frequency shifts of scattered laser light, and therefore velocity. However, equipment failures and inadequate flow seed density prevented accurate velocity measurements in the separated wake region behind a 6:1 prolate spheroid. The following conclusions and recommendations for future improvements are made:

1. The system-oriented design of the DGV resulted in an instrument which can be operated from a single computer by a lone operator with little experience.

2. New methods of temperature control for the iodine molecular filters using thermoelectrics performed extremely well, yielding lower temperature uncertainties than water bath systems.

3. Laser frequency locking performance during the tests was poor, which contributed to the high uncertainties in the velocity data. Repair of the laser system is being performed by the manufacturer.

   (a) After the laser is repaired, the current data reduction scheme should account for pulse to pulse laser frequency shifts.

   (b) To prevent future degradation in laser performance, the laser system should always be stored in a temperature and humidity controlled environment.

4. Malfunctions in one of the camera systems also contributed to the high uncertainty velocity data.
   (a) Use of lower f/number camera lenses (possibly down to 1.4) will improve the acquisition of single pulse velocity data, but increase distortion in the images.
   (b) Optimum positions for the camera modules must be determined in order to maximize sensitivity of the system and improve the signal to noise ratio.
5. A new flow seeding system, which produces at least 3-4 times the output volume of the unit employed in this research, is required for single laser pulse velocity data images.
   (a) The Rosco company makes several such large output smoke generators.
   (b) More seed would allow positioning of the seeder system in the tunnel settling chamber, producing less flow disturbance than injection from the test section ceiling.
   (c) A possible concern with injecting such a large volume of smoke is its affect on the flow structures and the scattered light path back to the camera systems. The minimum amount of smoke needed to acquire single laser pulse images must be used.
6. A new method for determining camera module orientation was implemented. The method only requires the images of the alignment dot grid as input, and provides the needed coordinate transformation from the camera reference frame to the measurement plane used in velocity calculations.
7. Detailed uncertainty analysis of the tested configuration show the system will be capable of accurate flow measurements.
   (a) Base levels of velocity uncertainty (excluding transmission ratio variance) for the *tested* configuration are $\pm 2.51 \frac{m}{s}$ for V_x, $\pm 4.59 \frac{m}{s}$ for V_y and $\pm 4.94 \frac{m}{s}$ for V_z.
   (b) These base levels can be lowered by diffusing the laser illumination on the white card during system calibration (and improved laser performance). This will decrease the reference transmission ratio uncertainties and can greatly reduce the overall velocity uncertainty.
   (c) Based on the analysis, uncertainty levels around $\pm 2 \frac{m}{s}$ will eventually be possible with the Virginia Tech DGV system.

The advances made in the design and construction of the Virginia Tech DGV place it in the forefront of current DGV research. If the recommendations given are carried

out, the DGV system can become an important tool for experimental fluid dynamics measurements at Virginia Tech.

References

[1] W. Rae and A. Pope, *Low Speed Wind Tunnel Testing.* New York: John Wiley and Sons, Inc., 2^{nd} ed., 1984. 2

[2] C. Chesnakas and R. Simpson, "Detailed Invesitigation of the Three-Dimensional Separation About a Prolate Spheroid," *AIAA Journal*, vol. 35, January 1997. 3, 10, 34, 44, 45

[3] M. Ölçmen and R. Simpson, "An Experimental Study of a Three-Dimensional Pressure-Driven Turbulent Boundary Layer," *Journal of Fluid Mechanics*, vol. 290, 1995. 3

[4] M. Samimy and M. Wernet, "Review of Planar Multiple-Component Velocimetry in High Speed Flows," *AIAA Journal*, vol. 38, April 2000. 3, 6, 12

[5] H. Shimizu, S. Lee, and C. She, "High Spectral Resoultion LIDAR System with Atomic Blocking Filters for Measuring Atmospheric Parameters," *Applied Optics*, vol. 22, no. 9, 1983. 5

[6] H. Shimizu, K. Noguchi, and C. She, "Atmospheric Temperature Measurement by a High Spectral Resolution LIDAR," *Applied Optics*, vol. 25, no. 9, 1986. 5

[7] R. Miles, W. Lempert, and J. Forkey, "Instantaneous Velocity Fields and Background Supression by Filtered Rayleigh Scattering," in *29^{th} Aerospace Sciences Meeting*, no. AIAA-91-0357, (Reno, Nevada), January 1991. 5, 6

[8] J. Forkey, W. Lempert, S. Bogdonoff, and R. Miles, "Volumetric Imaging of Supersonic Boundary Layers Using Filtered Rayleigh Scattering Background Suppression," in *32^{nd} Aerospace Sciences Meeting*, no. AIAA-94-0491, (Reno, Nevada), January 1994. 6

[9] W. Lempert, P. Wu, and R. Miles, "Filtered Rayleigh Scattering Measurements Using a MHz Rate Pulse-Burst Laser System," in *35^{th} Aerospace Sciences Meeting*, no. AIAA-97-0500, (Reno, Nevada), January 1997. 6

[10] G. Elliot and M. Samimy, "A Molecular Filter Based Technique for Simultaneous Measurements of Velocity and Thermodynamic Properties," in *35th Aerospace Sciences Meeting*, no. AIAA-96-0304, (Reno, Nevada), January 1996. 6, 16

[11] H. Komine, S. Brosnan, A. Litton, and E. Stappaerts, "Real-Time Doppler Global Velocimetry," in *29th Aerospace Sciences Meeting*, no. AIAA-91-0337, (Reno, Nevada), January 1991. 6, 18, 23, 30

[12] J. Meyers and H. Komine, "Doppler Global Velocimetry: A New Way to Look at Velocity," in *ASME 4th International Conference on Laser Anemometry, Advances and Applications*, (Clevland, Ohio), August 1991. 6, 23

[13] J. Meyers, "Doppler Global Velocimetry The Next Generation," in *17th Ground Testing Conference*, no. AIAA-92-3897, (Nashville, Tennessee), July 1992. 7, 18

[14] J. Meyers, "Development of Doppler Global Velocimetry for Wind Tunnel Testing," in *18th Ground Testing Conference*, no. AIAA-94-2582, (Colorad Springs, Colorado), June 1994. 7

[15] J. Meyers, G. Fleming, S. Gorton, and J. Berry, "Instantaneous Doppler Global Velocimetry Measurements of a Rotor Wake: Lessons Learned," in *9th International Symposium on Applications of Laser Technologies to Fluid Mechanics*, (Lisbon, Portugal), July 1998. 7, 17, 18, 19, 20, 34, 36, 57

[16] J. Meyers, "The Reduction of Laser Speckle Noise in Planar Doppler Velocimetry Systems," in *20th Advanced Measurement and Ground Testing Conference*, no. AIAA-98-2607, (Albuquerqe, New Mexico), June 1998. 7, 12

[17] R. McKenzie, "Measurement Capabilities of Planar Doppler Velocimetry Using Pulsed Lasers," in *33rd Aerospace Sciences Meeting*, no. AIAA-95-0297, (Reno, Nevada), January 1995. 7, 12, 13, 17, 18, 57

[18] Spectra-Physics Lasers, Inc., Mountain View, California, *Model 6300/6350 Injection Seeder Manual*, 1994. 8, 12

[19] R. McKenzie, "Planar Doppler Velocimetry Performance in Low Speed Flows," in *35th Aerospace Sciences Meeting*, no. AIAA-97-0498, (Reno, Nevada), January 1997. 9

[20] R. McKenzie and M. Reinath, "Planar Doppler Velocimetry at Low Speeds and Its Application to a Full-Scale Rotor Flow (Invited)," in *21st Aerodynamic Measurement Technology and Ground Testing Conference*, no. AIAA-2000-2292, (Denver, Colorado), June 2000. 9, 13, 17, 25, 28, 30, 34

[21] A. Mosedale, G. Elliot, C. Carter, W. Weaver, and T. Buetner, "On the Use of Planar Doppler Velocimetry," in *29th Fluid Dynamics Conference*, no. AIAA-98-2809, (Albuquerque, New Mexico), June 1998. 9

[22] S. Arnette, G. Elliot, A. Mosedale, and C. Carter, "A Two-Color Approach to Planar Doppler Velocimetry," in *36th Aerospace Sciences Meeting*, no. AIAA-98-0507, (Reno, Nevada), January 1998. 9

[23] G. Elliot, T. Buetner, and C. Carter, "Application of Planar Doppler Velocimetry Wind Tunnel Testing," in *38th Aerospace Sciences Meeting*, no. AIAA-2000-0412, (Reno, Nevada), January 1996. 9, 13, 15

[24] S. Ramanath, "Development of a point doppler global velocimeter," Master's thesis, West Virginia University, MAE Department, 1997. 9

[25] J. Kuhlman, S. Naylor, K. James, and S. Ramanath, "Accuracy Study of 2-Component Point Doppler Velocimeter (PDV)," in *28th Fluid Dynamics Conference*, no. AIAA-97-1916, (Snowmass, Colorado), June 1997. 9

[26] S. Naylor, *Development and Accuracy Determiniation of a Two-Component Doppler Global Velocimeter.* PhD thesis, West Virginia University, MAE Department, 1998. 9, 11, 12, 15, 17, 19, 20, 30, 34

[27] S. Naylor and J. Kuhlman, "Accuracy Study of Two-Component Doppler Global Velocimeter (DGV)," in *36th Aerospace Sciences Meetings*, no. AIAA-97-0508, (Reno, Nevada), January 1998. 9

[28] T. Wetzel, *Unsteady Flow over a 6:1 Prolate Spheroid.* PhD thesis, Virginia Polytechnic Institute & State University, 1996. 10

[29] T. Wetzel and R. Simpson, "Unsteady Crossflow Separation Location Measurements on a Maneuvering 6:1 Prolate Spheroid," *AIAA Journal*, vol. 36, November 1998. 10, 55

[30] J. Mila, Personal Communication, 1999. Spectra-Physics Repair Engineer. 14

[31] V. Chan, A. Heyes, D. Robinson, and J. Turner, "Iodine absorption filters for Doppler global velocimetry," *Measurement Science and Technology*, no. 6, 1995. 14, 15

[32] F. H. Moffitt and E. M. Mikhail, *Photogrammetry.* New York: Harper & Row, 3rd ed., 1980. 17

[33] G. Fleming, Personal Communication, 1997. NASA Langley Research Engineer. 18, 56

[34] J. Meyers, "Evolution of Doppler Global Velocimetry Data Processing," in *8^{th} International Symposium on Applications of Laser Technologies to Fluid Mechanics*, (Lisbon, Portugal), July 1996. 23

[35] G. Wolberg, *Digital Image Warping.* Los Alamitos, California: IEEE Computer Society Press, 1992. 25

[36] C. Lindley, *Practical Image Processing in C.* New York: John Wiley and Sons, Inc., 1991. 26, 28

[37] J. N. Forkey, W. R. Lempert, and R. B. Miles, "Corrected and calibrated I_2 absorption model at fequency-doubled Nd:YAG laser wavelengths," *Applied Optics*, vol. 36, September 1997. 30, 54, 66

[38] B. Etkin and L. Reid, *Dynamics of Flight Stability and Control.* New York: John Wiley and Sons, Inc., 1996. 82

[39] C. C. Slama, C. Theurer, and S. W. Henriksen, eds., *Manual of Photogrammetry.* Falls Church, Virginia: American Society of Photogrammetry, 4^{th} ed., 1980. 85, 86

[40] Z. Zhang, "Flexible Camera Calibration By Viewing a Plane From Unkown Orientations," in *7^{th} IEEE International Conference on Computer Vision*, no. 6365272, September 1999. 86, 87

[41] R. Tsai, "A versatile camera calibration technique for high accuracy 3D machine vision metrology using off-the-shelf TV cameras and lenses ," *IEEE Journal of Robotics and Automation*, no. 4, 1987. 87

[42] J. Holman, *Experimental Methods for Engineers.* New York: McGraw-Hill, Inc., 6^{th} ed., 1994. 90, 91

Figures

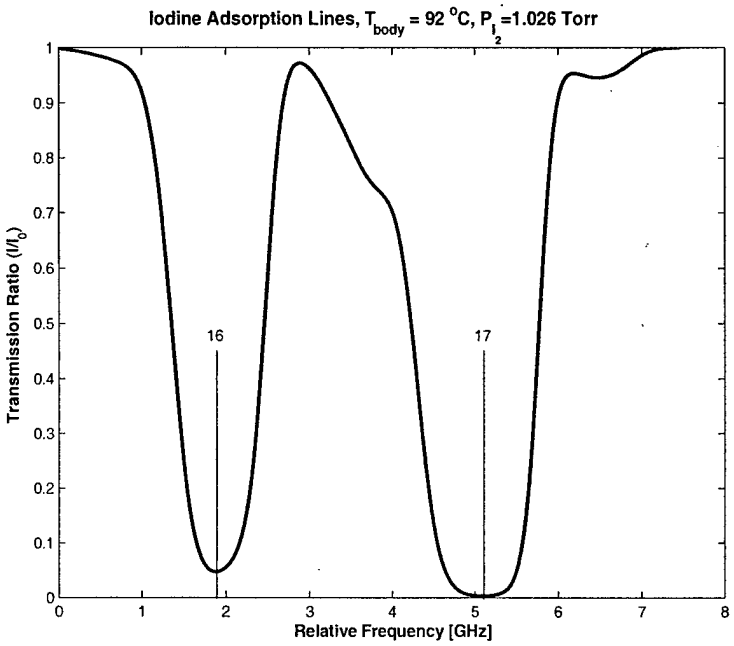

Figure 1.1: Example iodine transmission lines in the vicinity of 532*nm* (output from a program by Forkey [37])

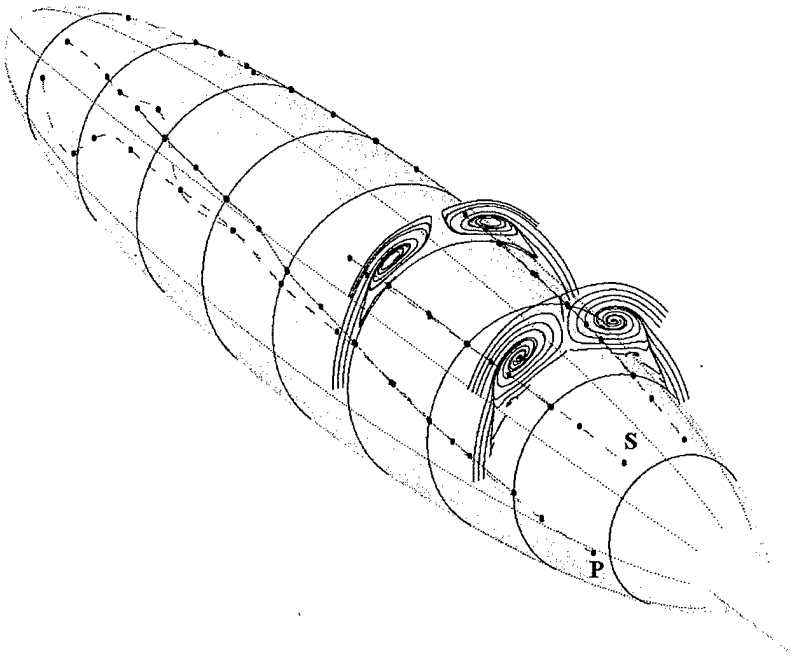

Figure 1.2: Crossflow separation topology over a 6:1 prolate spheroid, $Re_L = 4.2 \times 10^6$ (from ref. [29])

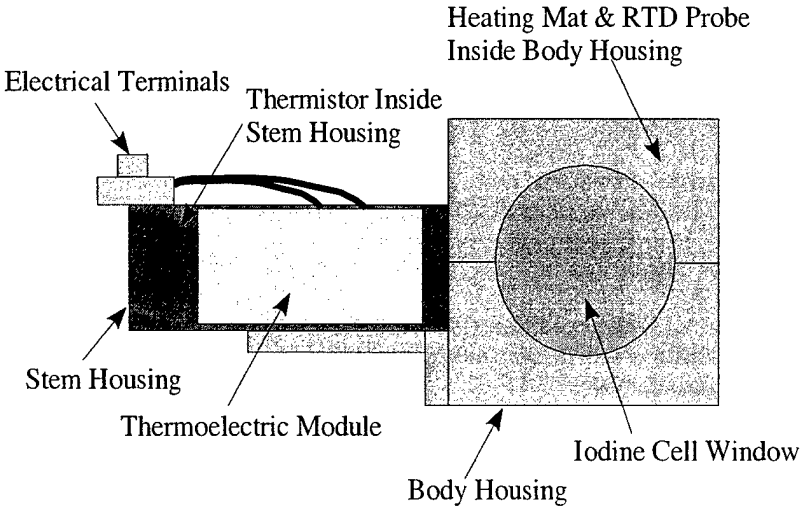

Figure 3.1: Iodine cell temperature control housing design

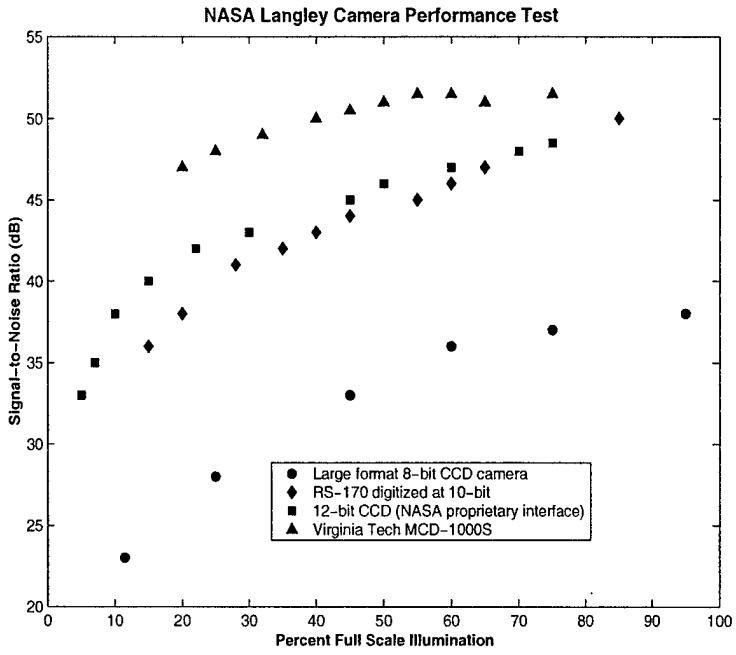

Figure 3.2: Camera performance comparison from NASA Langley tests conducted by G. Fleming [33] (exact model names of other tested systems were withheld)

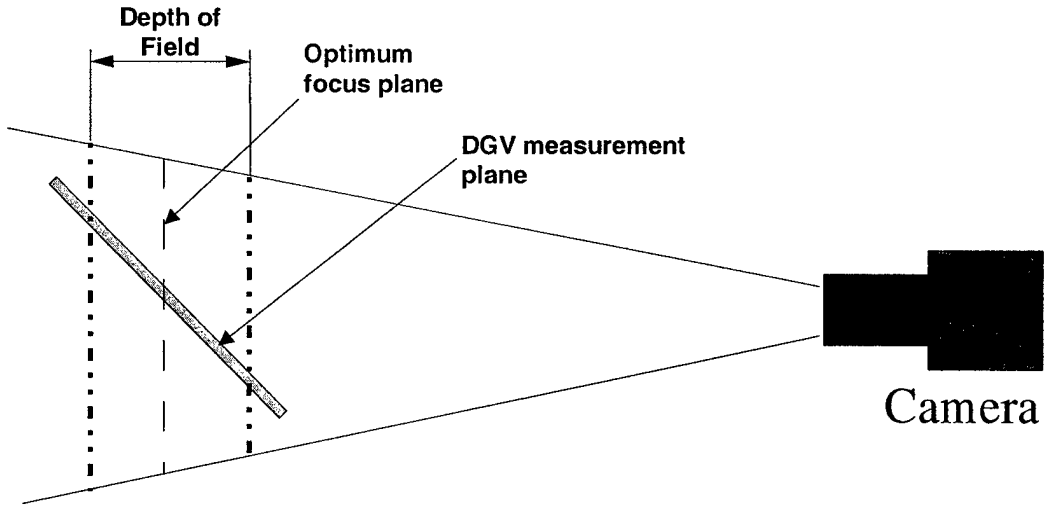

Figure 3.3: Possible effect of decreasing the camera lens depth of field for DGV use

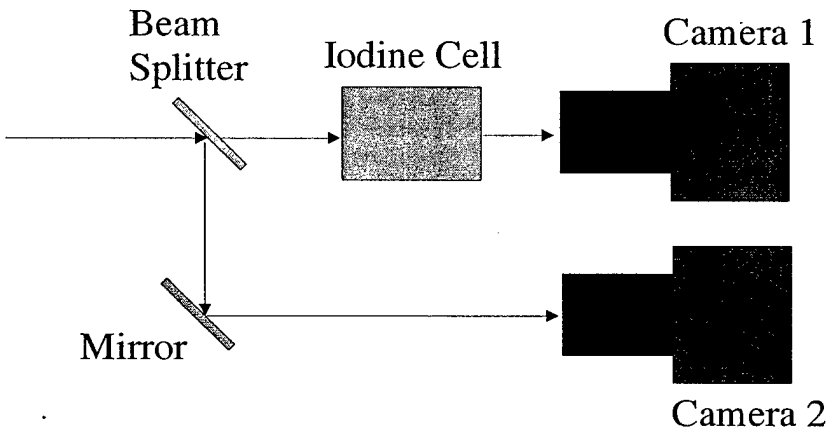

Figure 3.4: Schematic of a two-camera DGV measurement component used by Meyers [15]

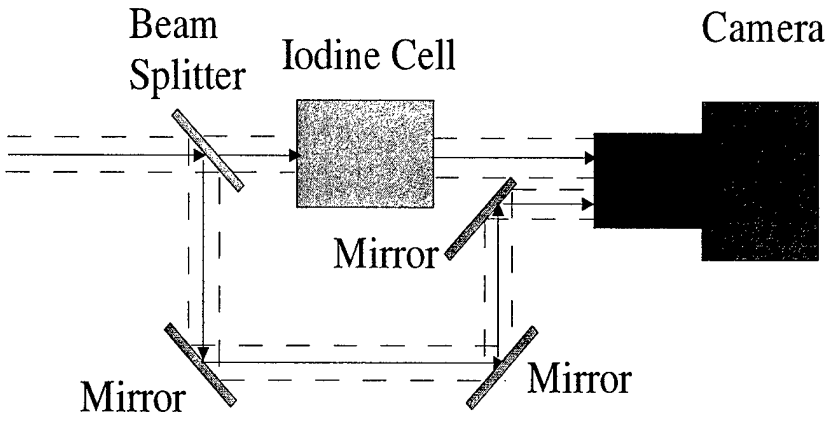

Figure 3.5: Schematic of split-image optics DGV measurement component used by McKenzie [17]

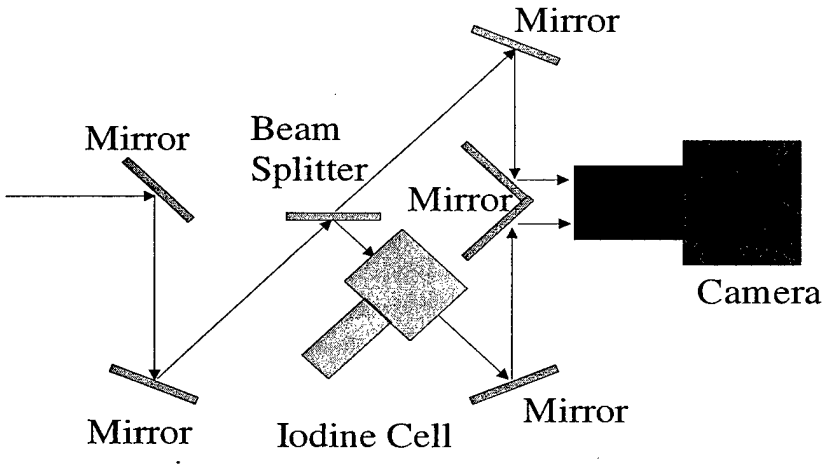

Figure 3.6: Schematic of a Virginia Tech DGV measurement component

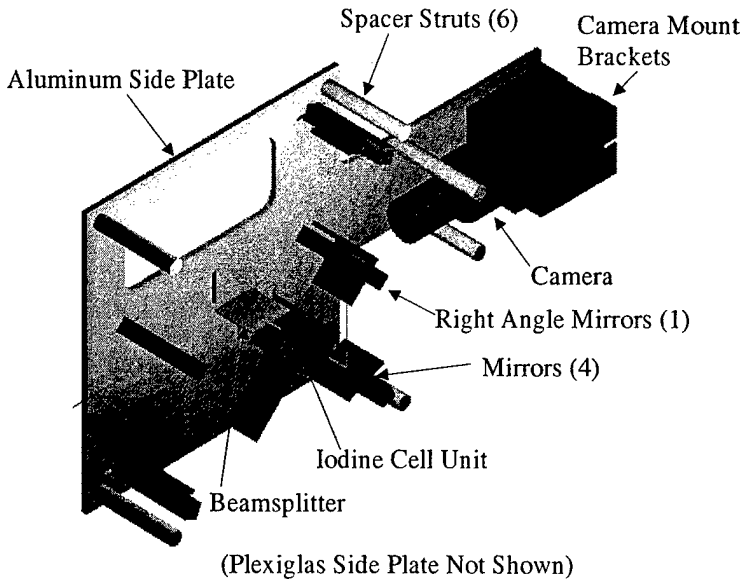

Figure 3.7: Virginia Tech DGV module design features

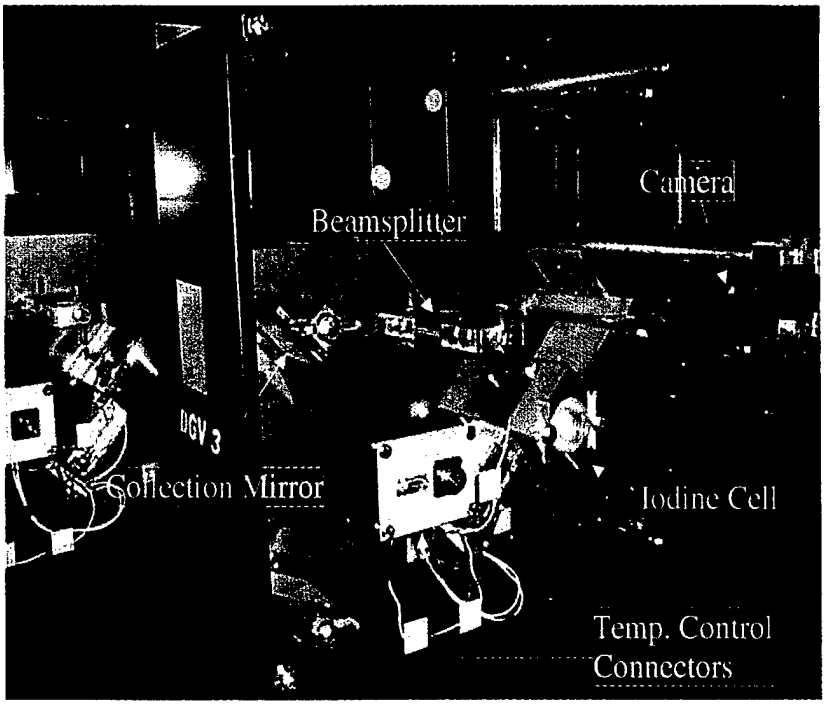

Figure 3.8: Completed Virginia Tech DGV module (close-up)

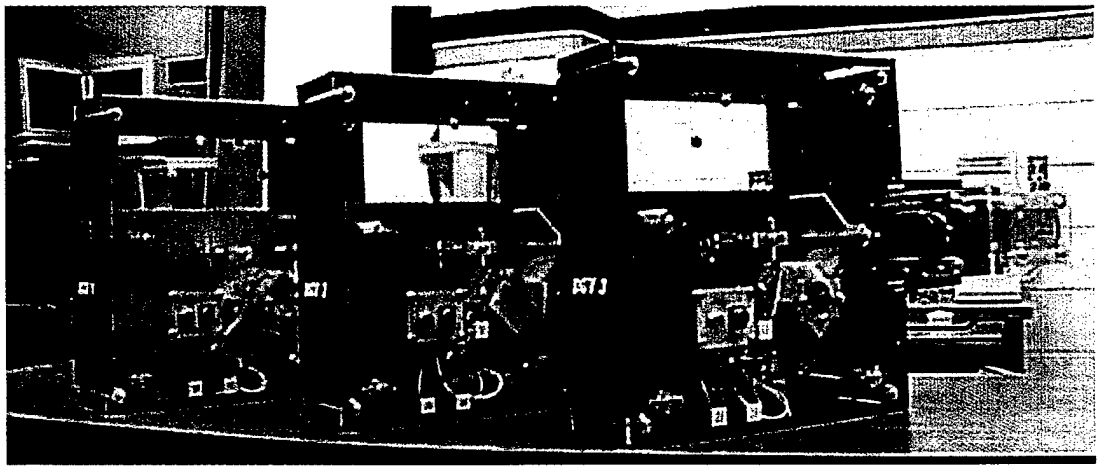

Figure 3.9: All three completed Virginia Tech DGV modules

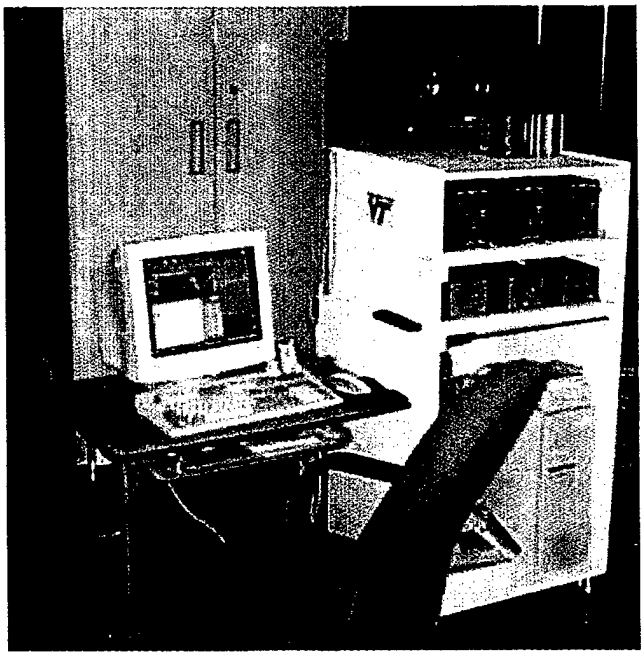

Figure 3.10: Virginia Tech DGV control cart: iodine cell stem temperature controllers on top shelf, body controllers on middle shelf, and control computer on bottom

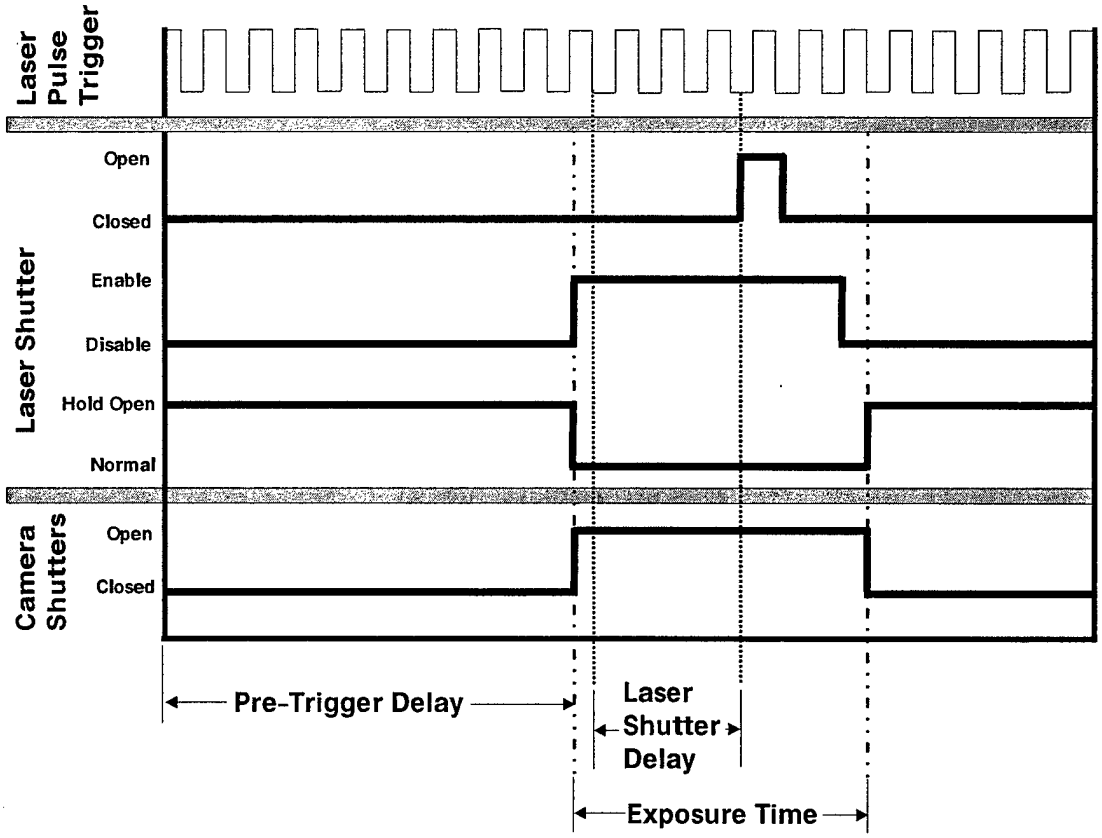

Figure 3.11: Virginia Tech DGV Control program steady measurement timing diagram. Note the laser pulses are not to drawn to scale for clarity. Typical time values are: Pre-Trigger Delay = 2000*ms*, Laser Shutter Delay = 500*ms* and Exposure Time = 3000*ms* (laser shutter always remains open for 100*ms*)

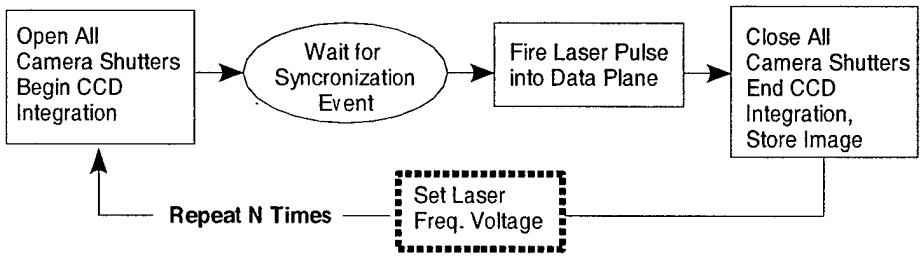

Figure 4.1: Flow diagram for image acquisition (dotted line indicates step performed only during iodine cell calibration)

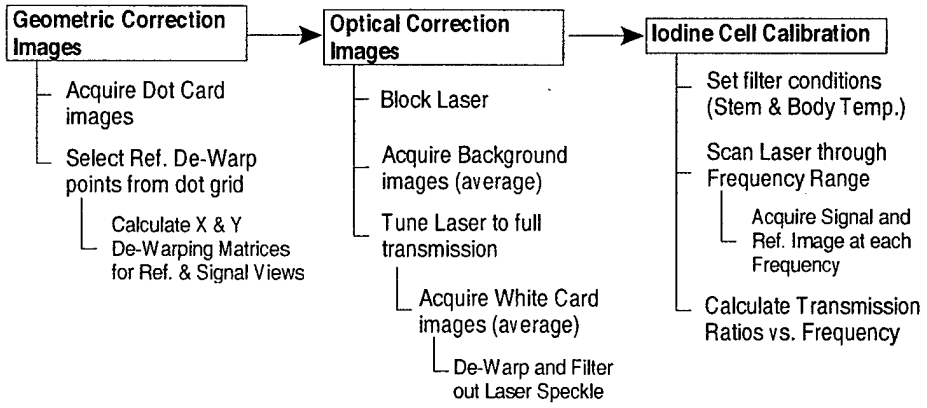

Figure 4.2: Acquisition steps for correction and iodine cell calibration images

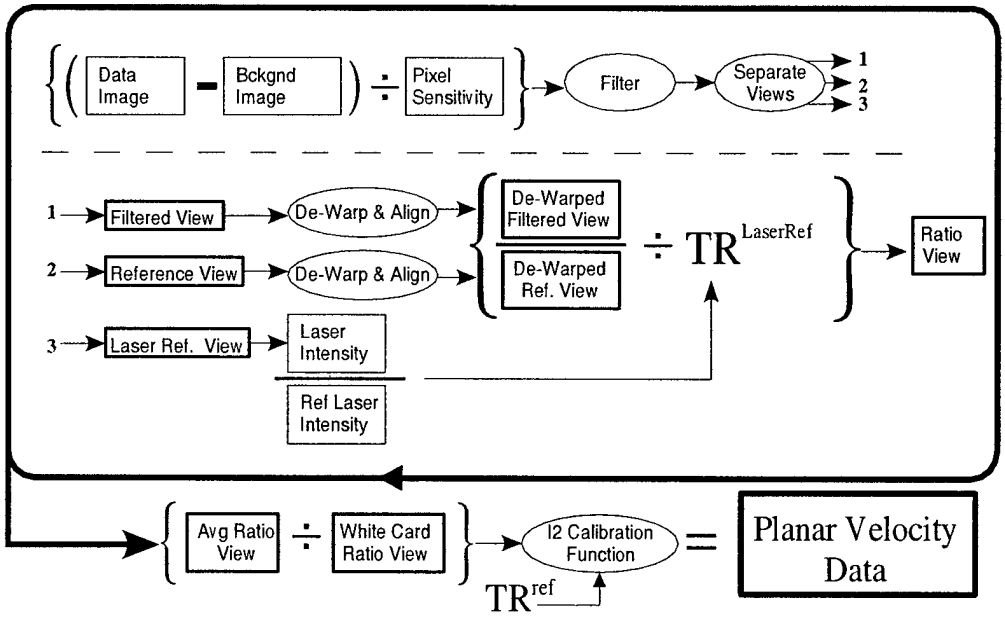

Figure 4.3: Diagram of DGV data reduction procedure

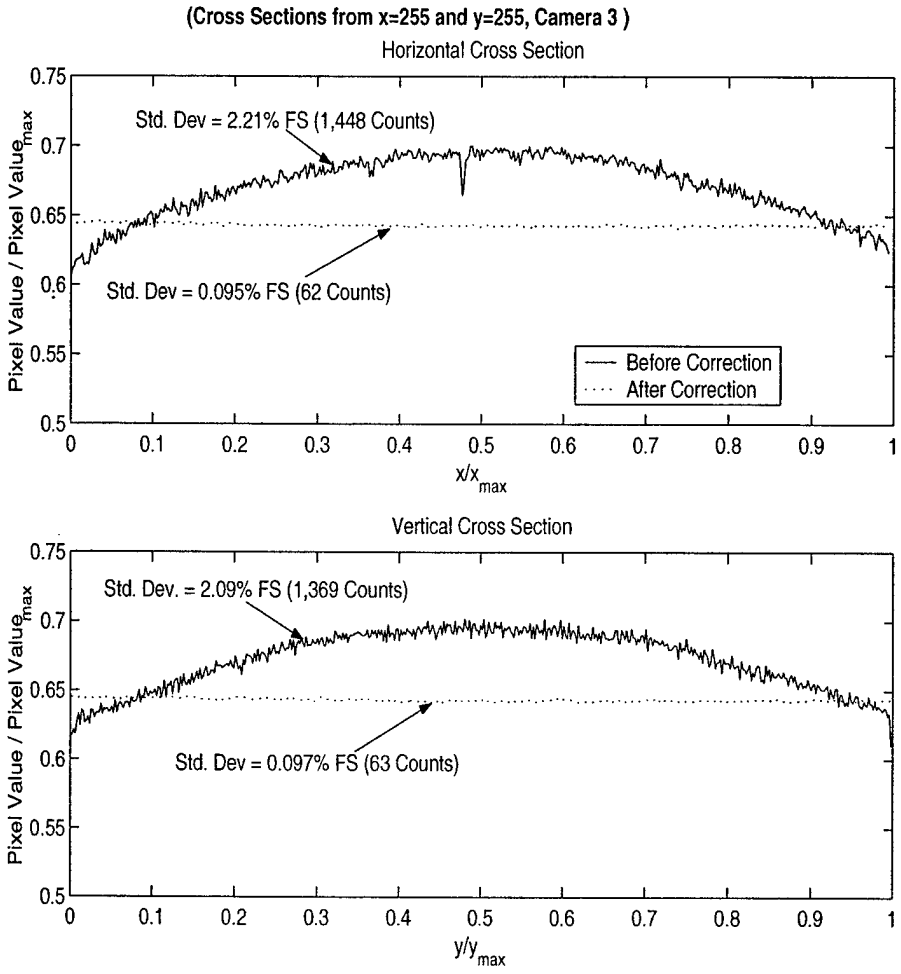

Figure 4.4: Horizontal and vertical mid-image cross sections showing the effectiveness of pixel sensitivity correction

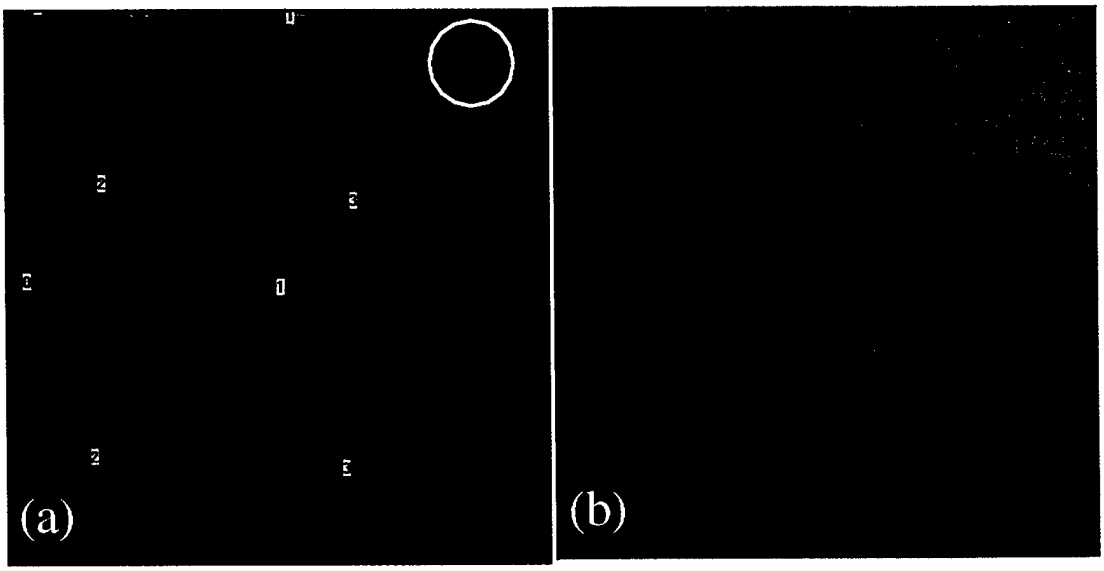

Figure 4.5: (a) Camera 1 view of alignment grid (b) Camera 1 dewarped reference view of alignment grid

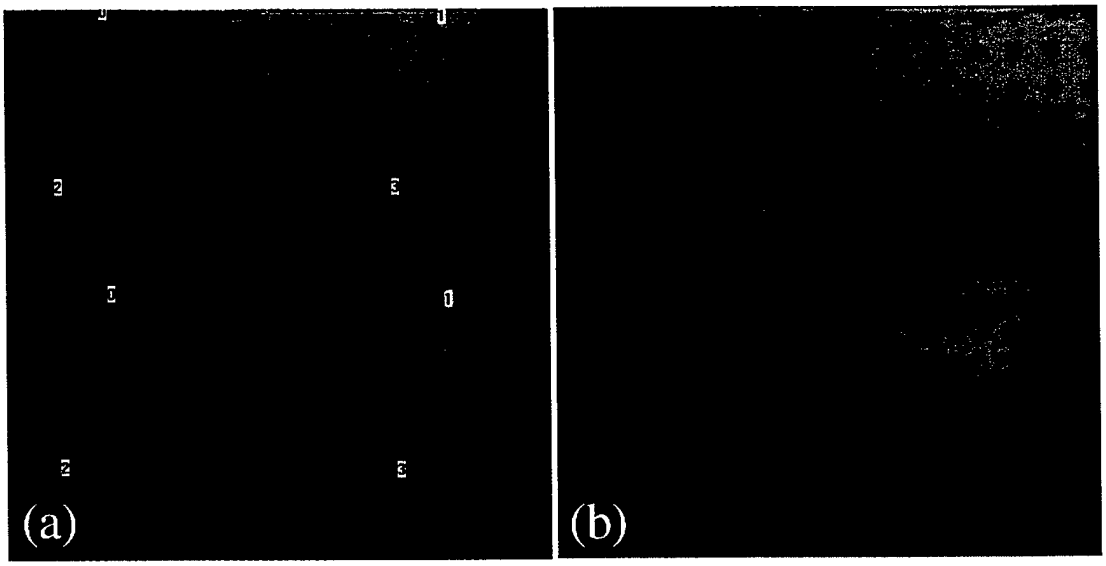

Figure 4.6: (a) Camera 2 view of alignment grid (b) Camera 2 dewarped reference view of alignment grid

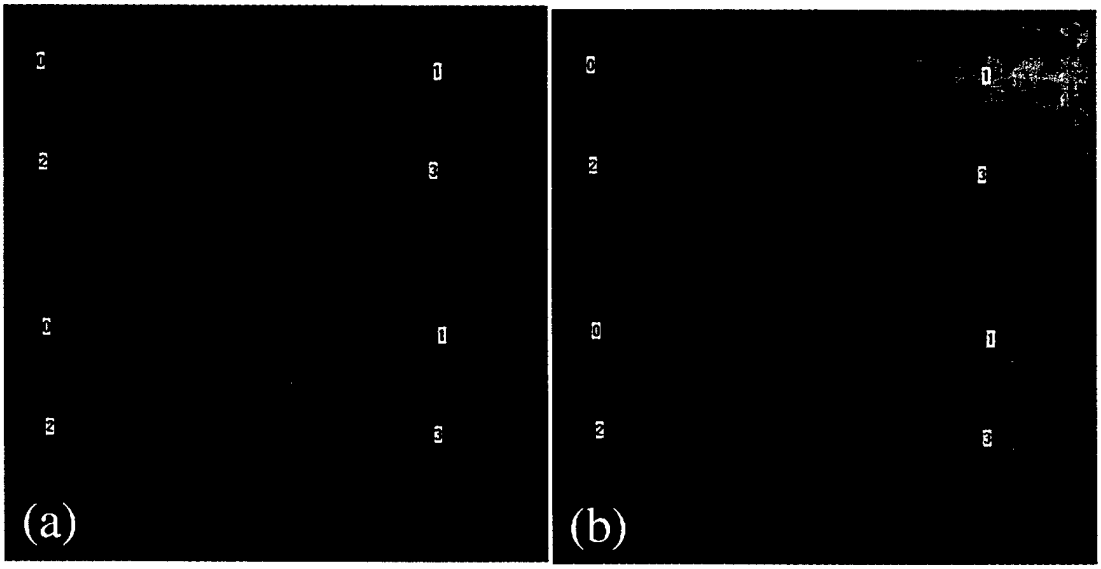

Figure 4.7: (a) Camera 3 view of alignment grid (b) Camera 3 dewarped reference view of alignment grid

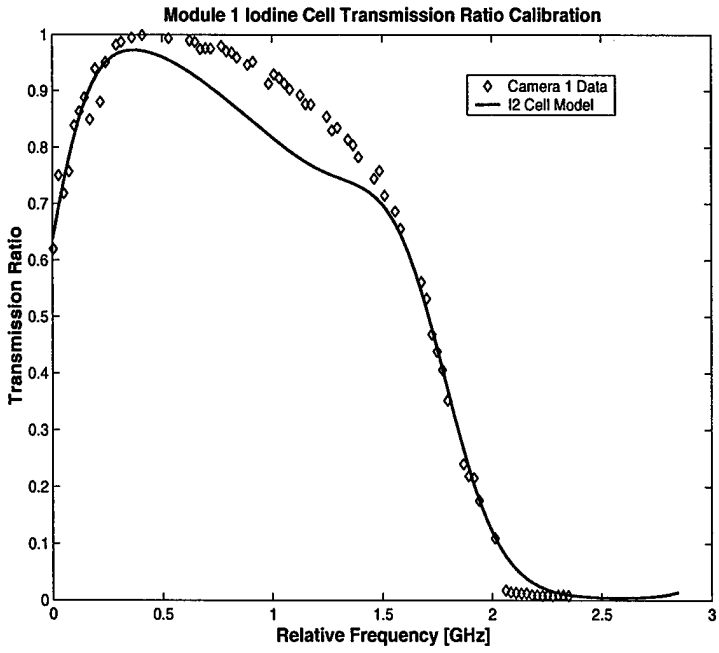

Figure 4.8: Module 1 experimental iodine cell calibration data and model transmission line

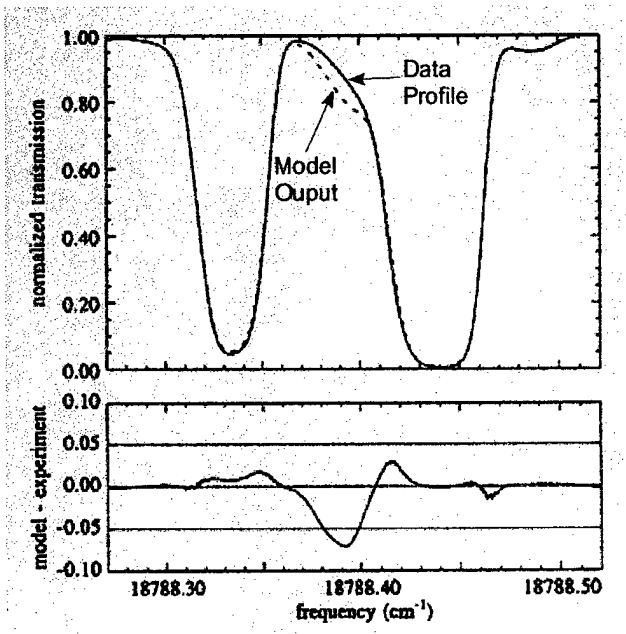

Figure 4.9: Experimental transmission line compared to model output (figure from Forkey *et al.* [37])

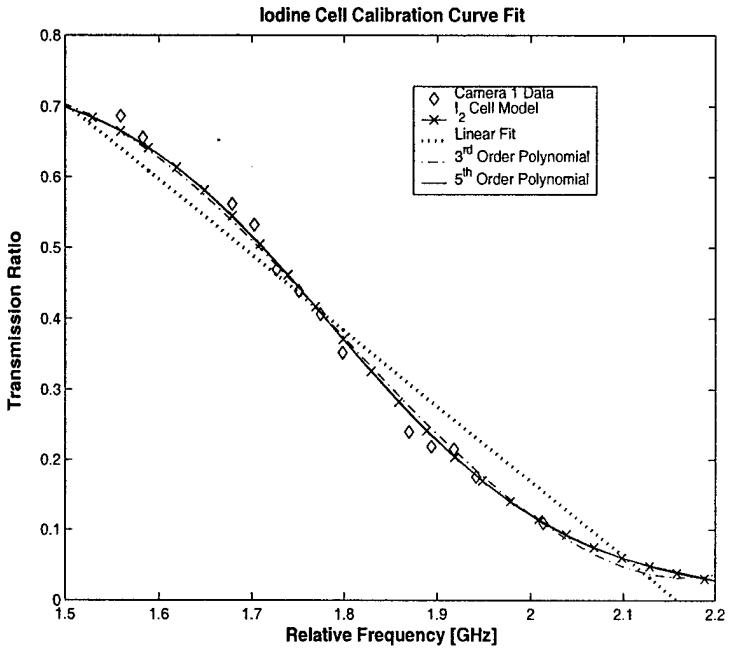

Figure 4.10: Measurement region of the iodine absorption line showing experimental data and the model predicted profile with 1^{st}, 3^{rd} and 5^{th} order polynomial fits

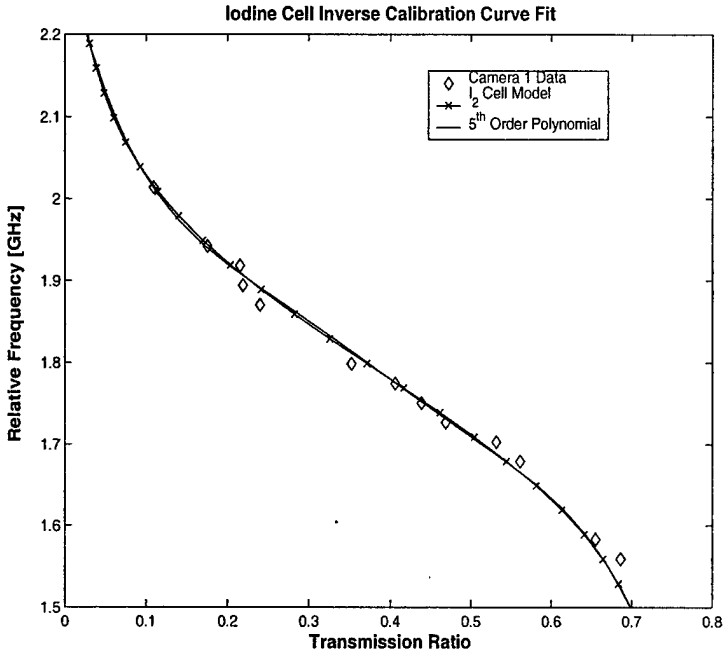

Figure 4.11: DGV velocity calculation iodine calibration function

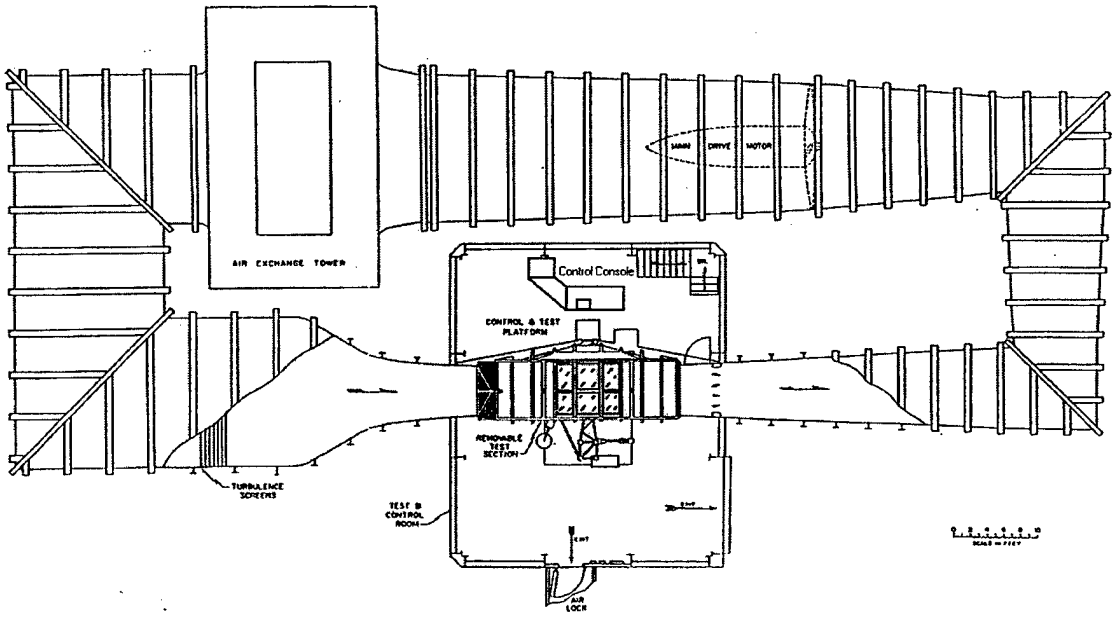

Figure 5.1: Top view of the Virginia Tech Stability Wind Tunnel

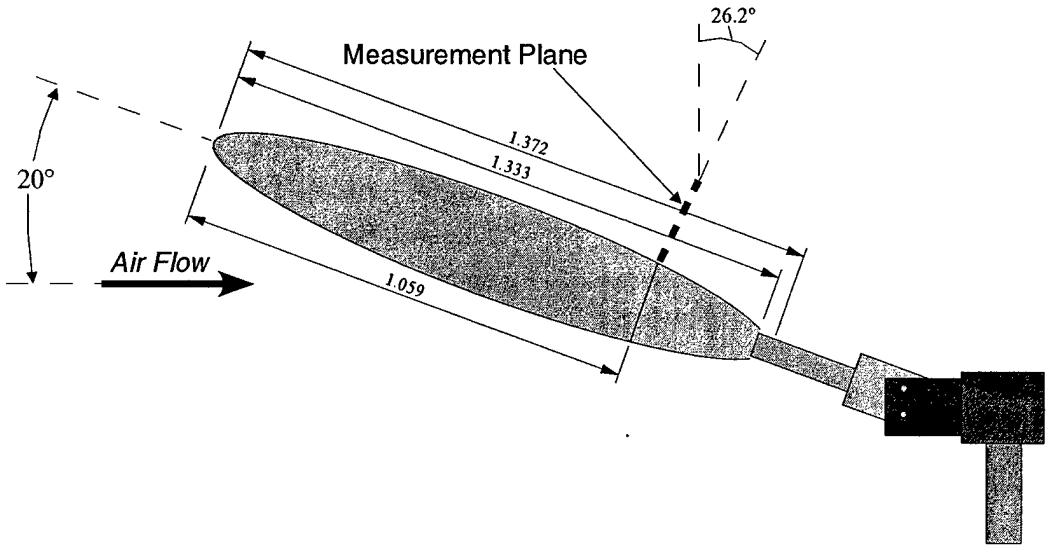

Figure 5.2: Side view of 6:1 prolate spheroid model and sting mount for Virginia Tech Stability Wind Tunnel (dimensions in m)

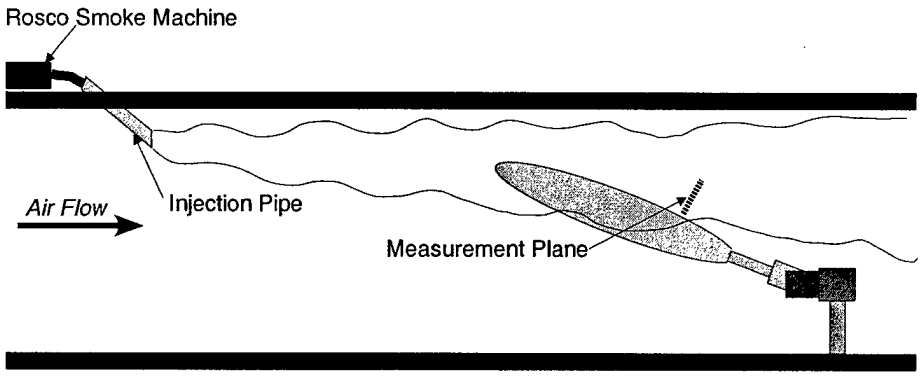

Figure 5.3: Injection of smoke into the wind tunnel test section

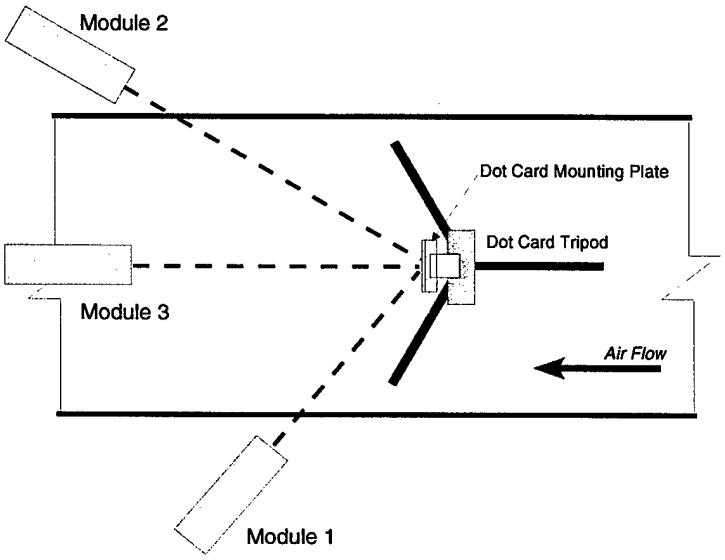

Figure 5.4: Top view of DGV module positions

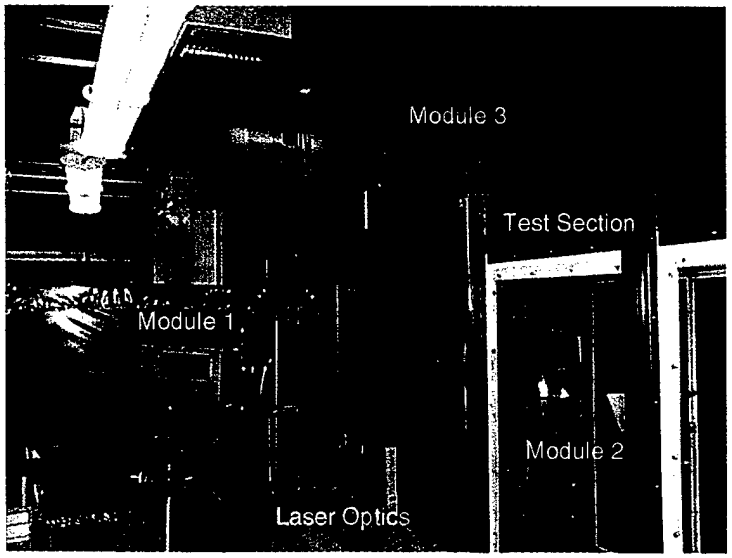

Figure 5.5: View from tunnel control room showing the DGV module positions

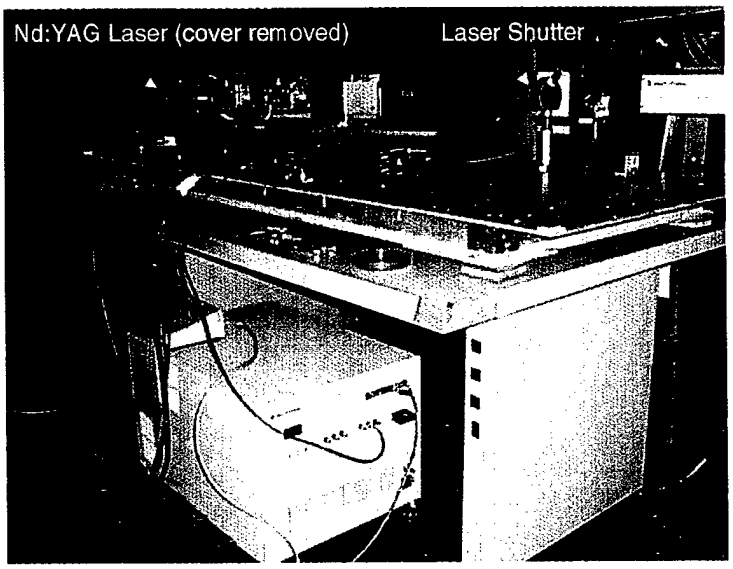

Figure 5.6: Nd:YAG laser system mounted below the Stability Tunnel test section

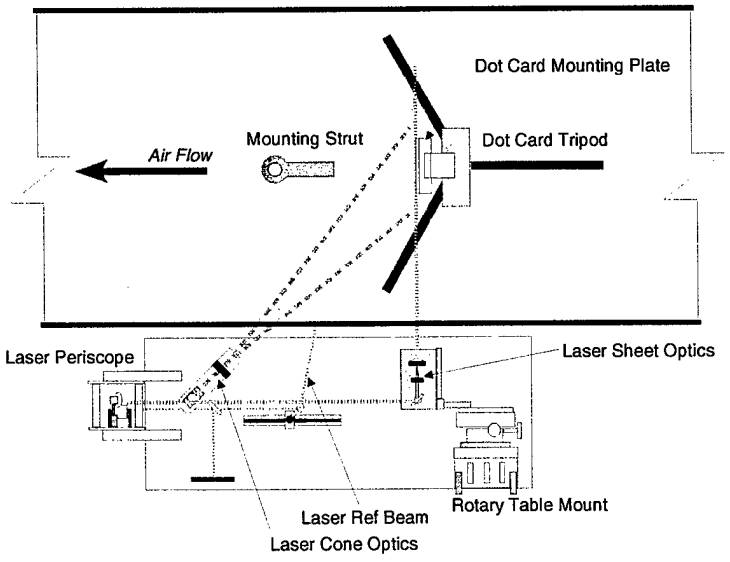

Figure 5.7: Top view of laser sheet and cone optics, and alignment dot grid tripod

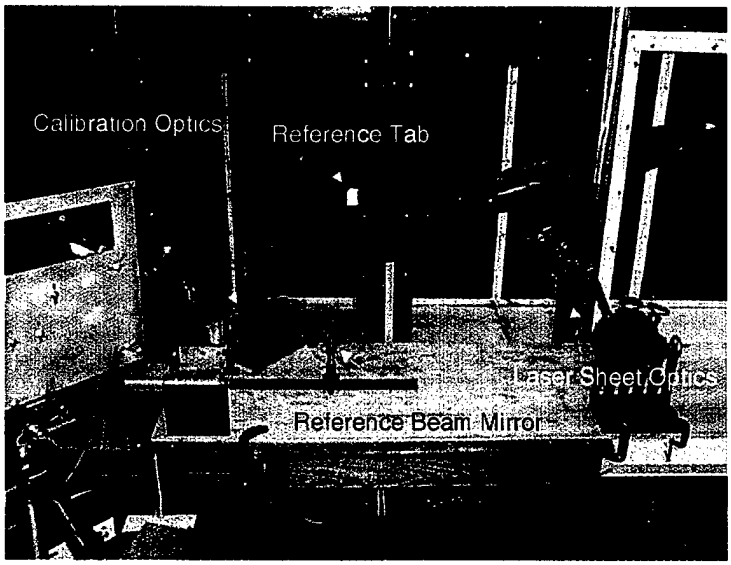

Figure 5.8: Control room view of laser optics, mounted prolate spheroid model and camera module 1

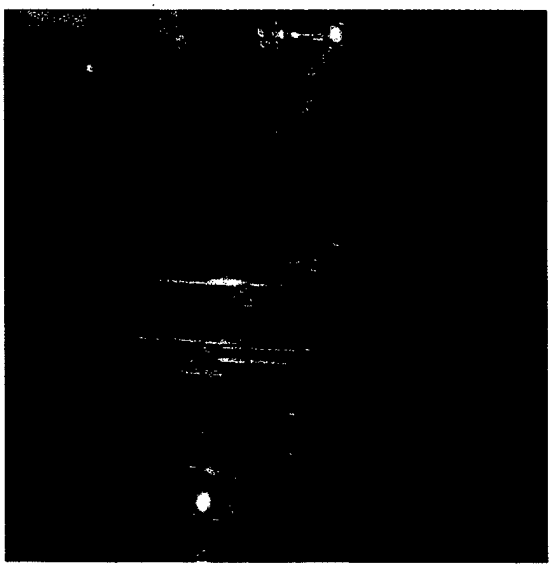

Figure 5.9: Picture of the laser optics during a test, from over the periscope (note the back reflection from the laser sheet mirror)

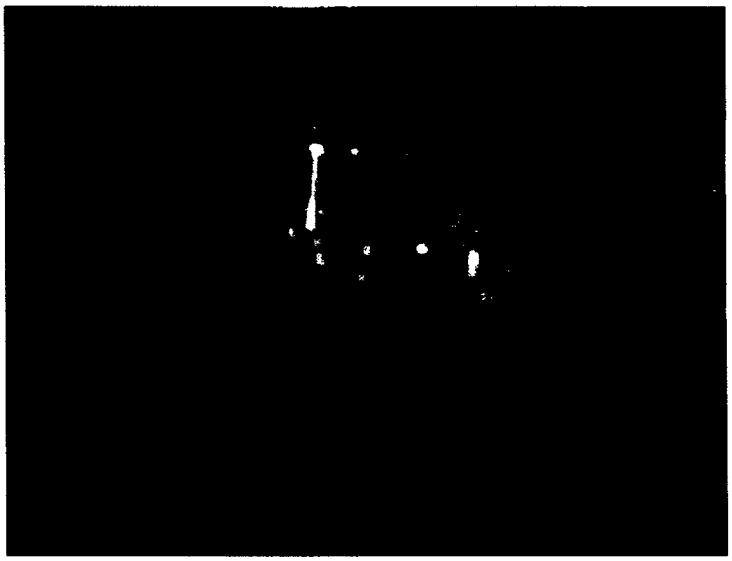

Figure 5.10: Close up of laser sheet optics during a test (note the cutout in the Plexiglas window for laser sheet)

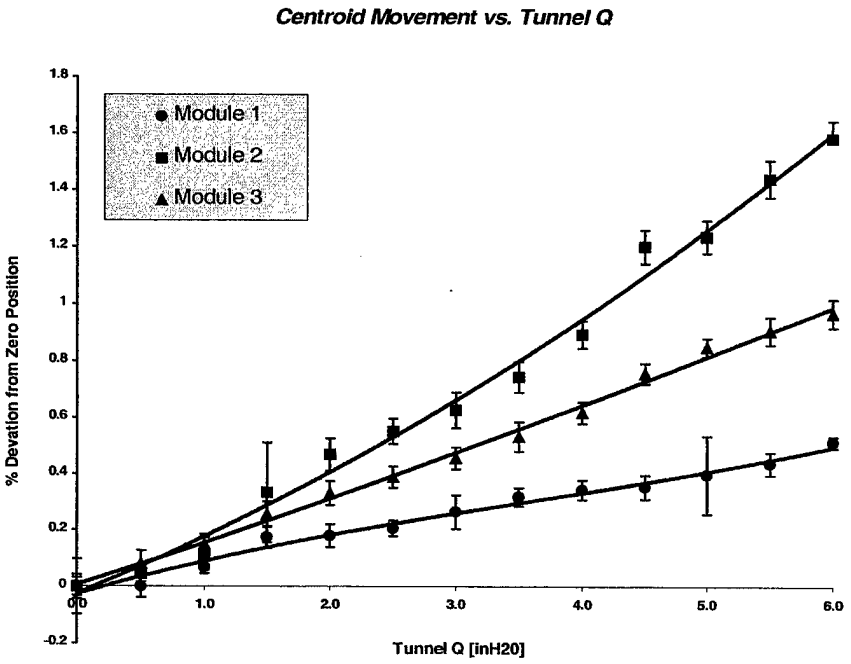

Figure 5.11: Vibration analysis for tunnel dynamic pressures up to $1.5kPa$ ($6inH_2O$)

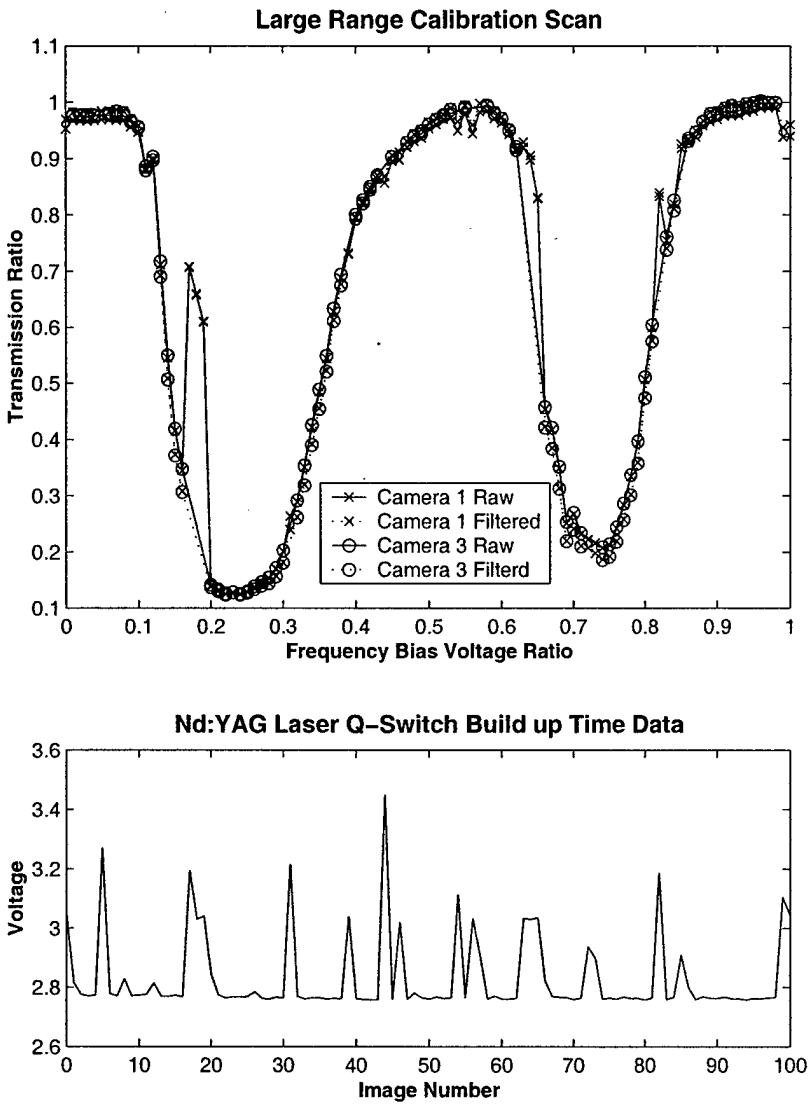

Figure 5.12: Calibration scan and laser performance data covering two iodine absorption lines

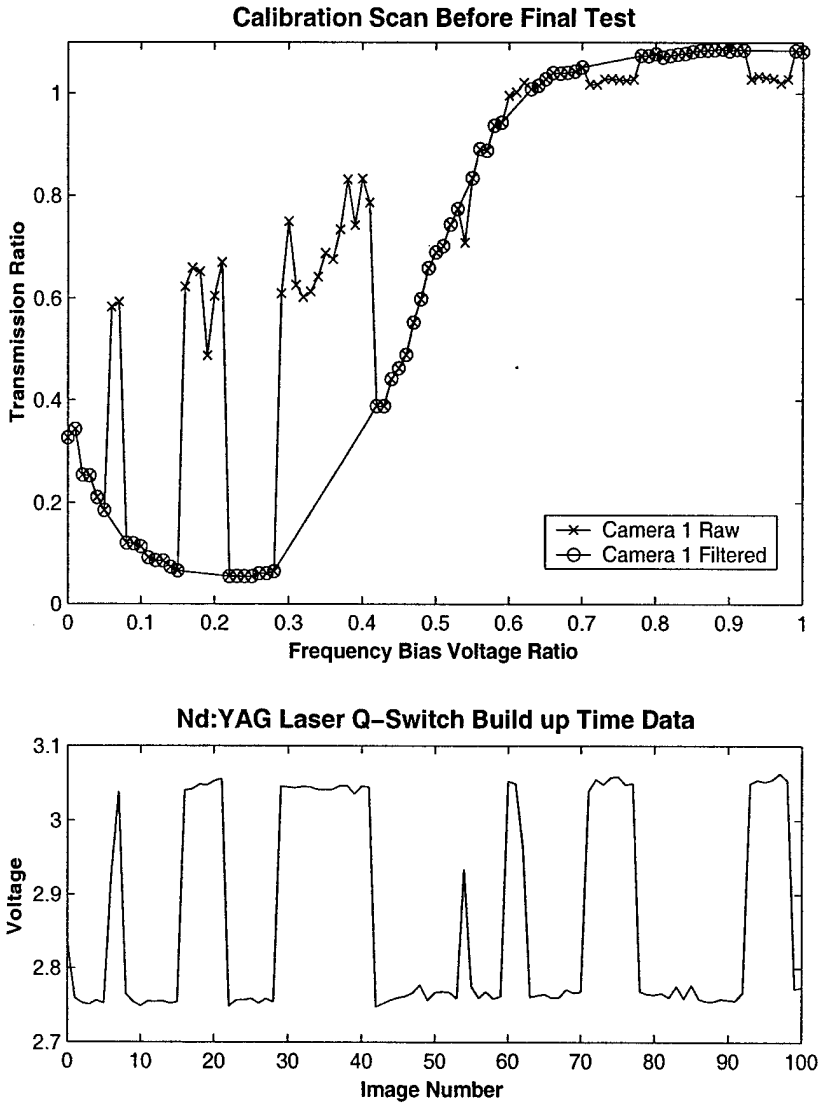

Figure 5.13: Module 1 iodine cell calibration scan and laser performance data taken before the final set of velocity data

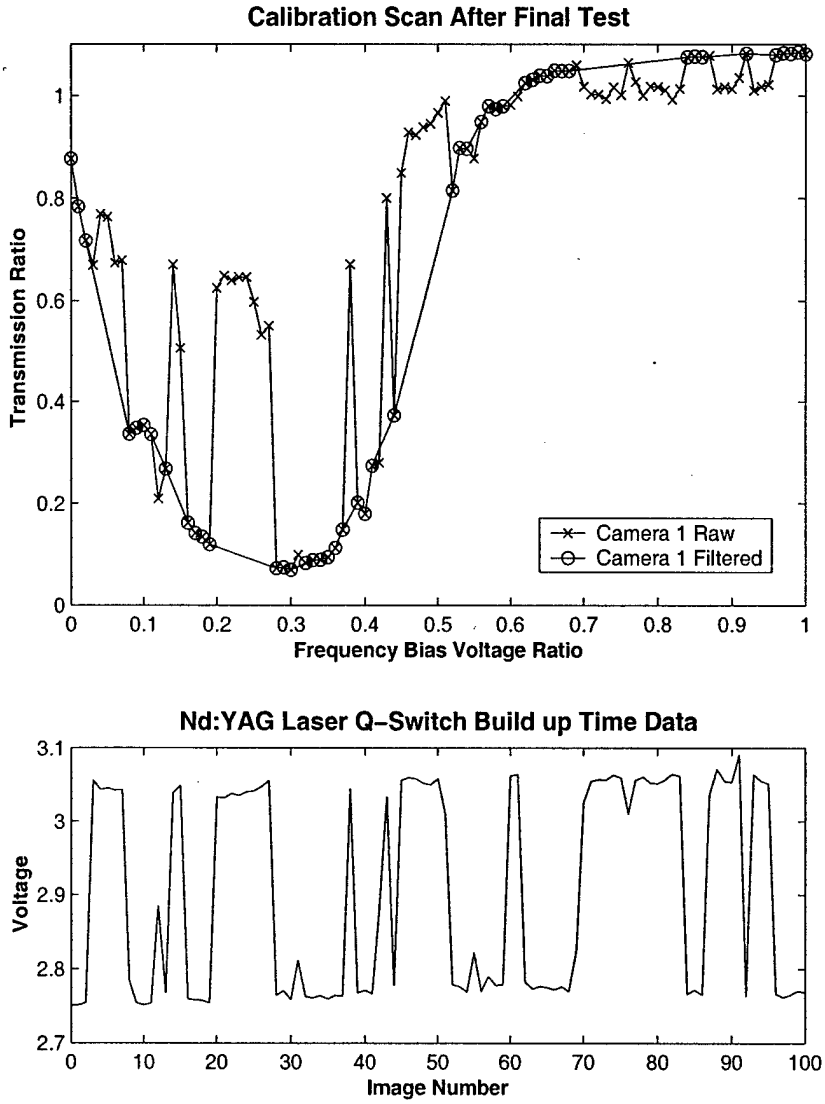

Figure 5.14: Module 1 iodine cell calibration scan and laser performance data taken after the final set of velocity data

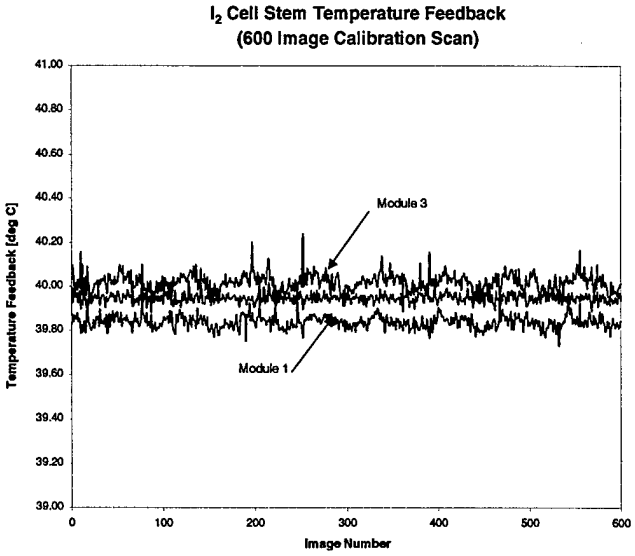

Figure 5.15: Iodine cell temperature control feedbacks from all three modules for a 600 image calibration scan

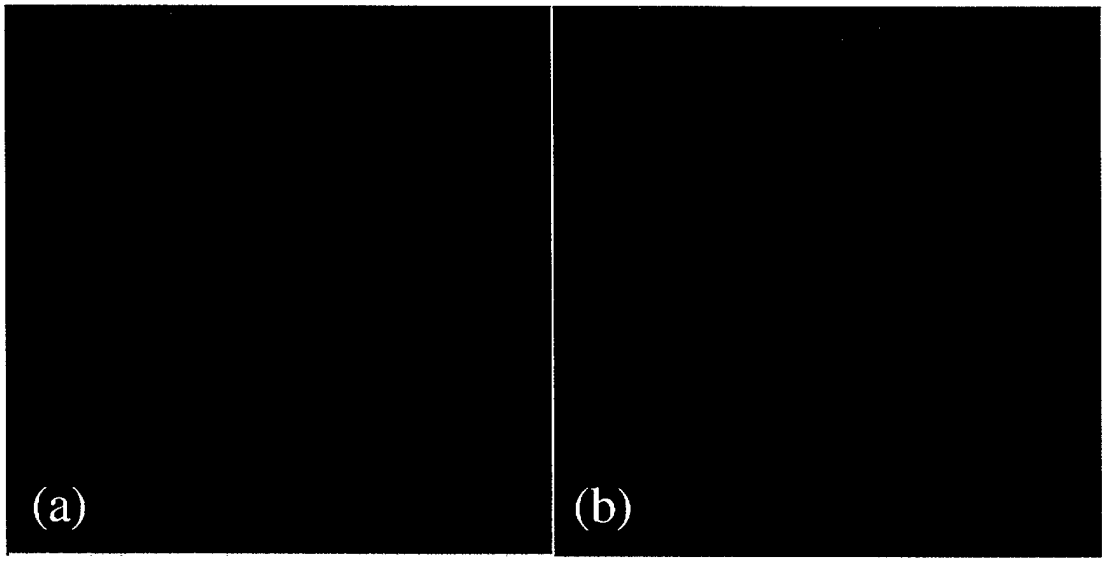

Figure 5.16: Module 1 views of prolate spheroid wake flow (a) raw data images (b) dewarped for processing

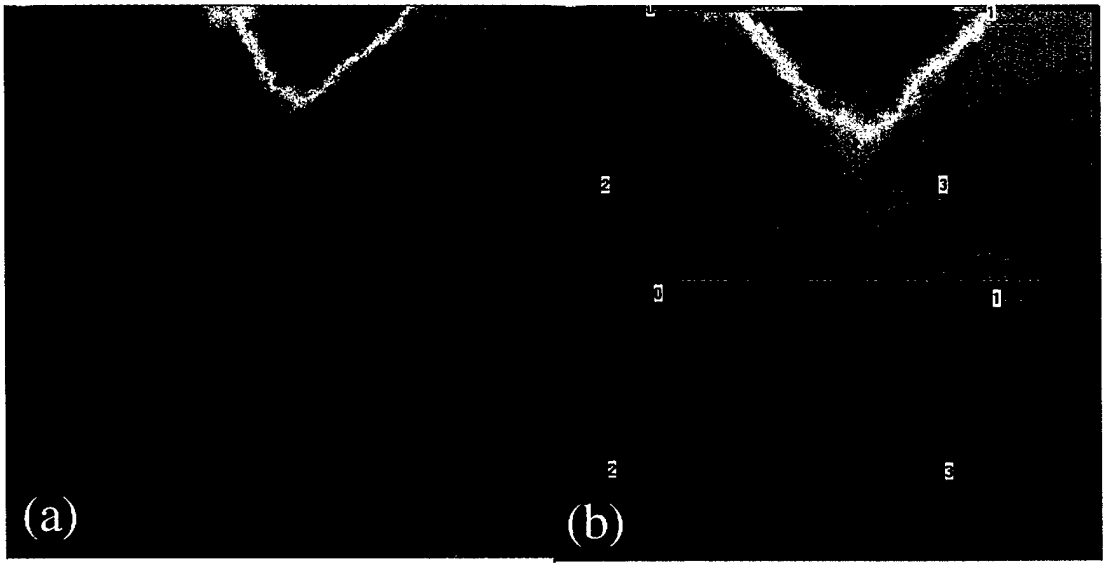

Figure 5.17: Module 2 views of prolate spheroid wake flow (a) raw data images (b) dewarped for processing

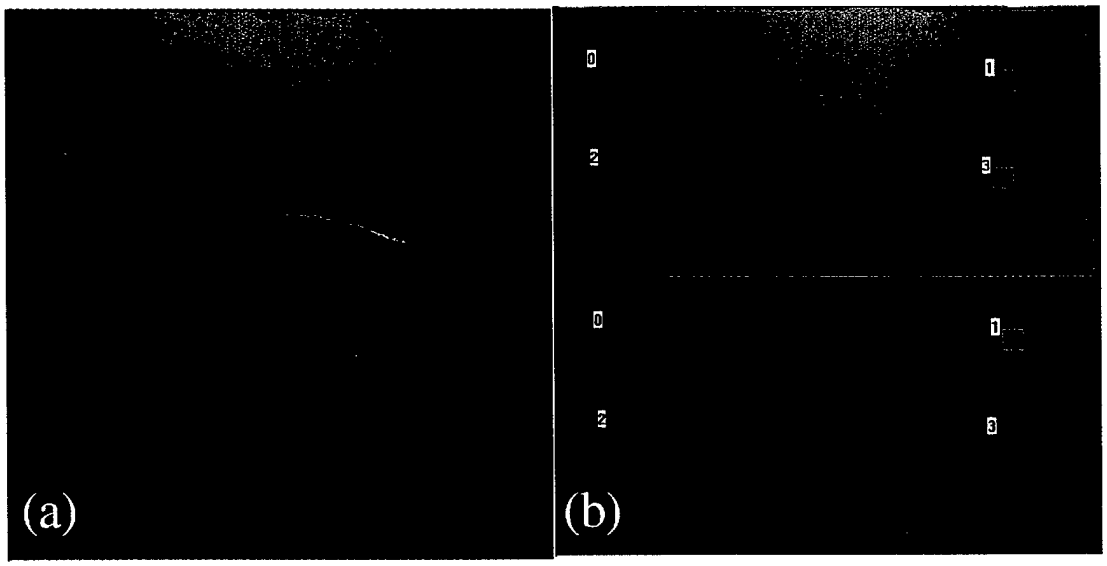

Figure 5.18: Module 3 views of prolate spheroid wake flow (a) raw data images (b) dewarped for processing

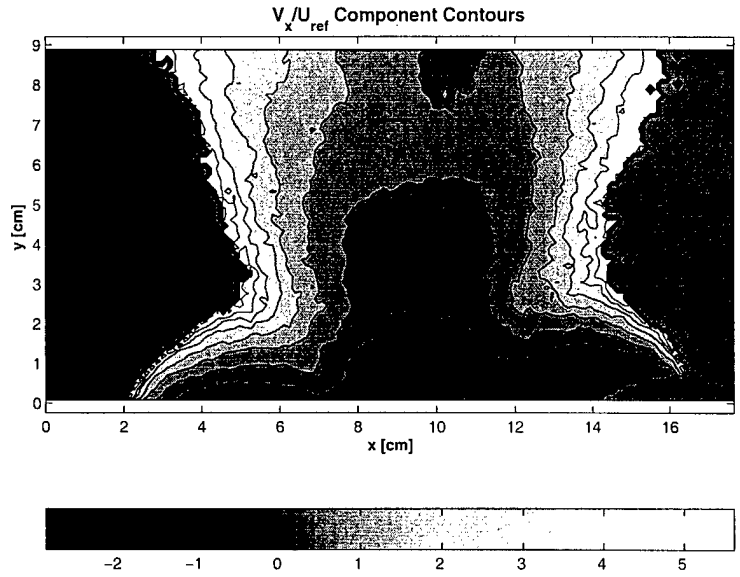

Figure 5.19: Contours of V_x velocity component from the acquired prolate spheroid flow images

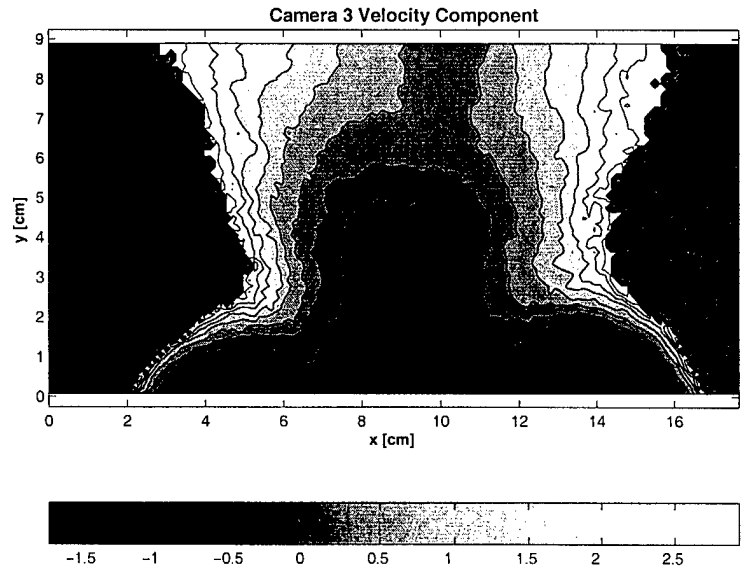

Figure 5.20: Contours of velocity in the Camera 3 measurement direction from the acquired prolate spheroid flow images

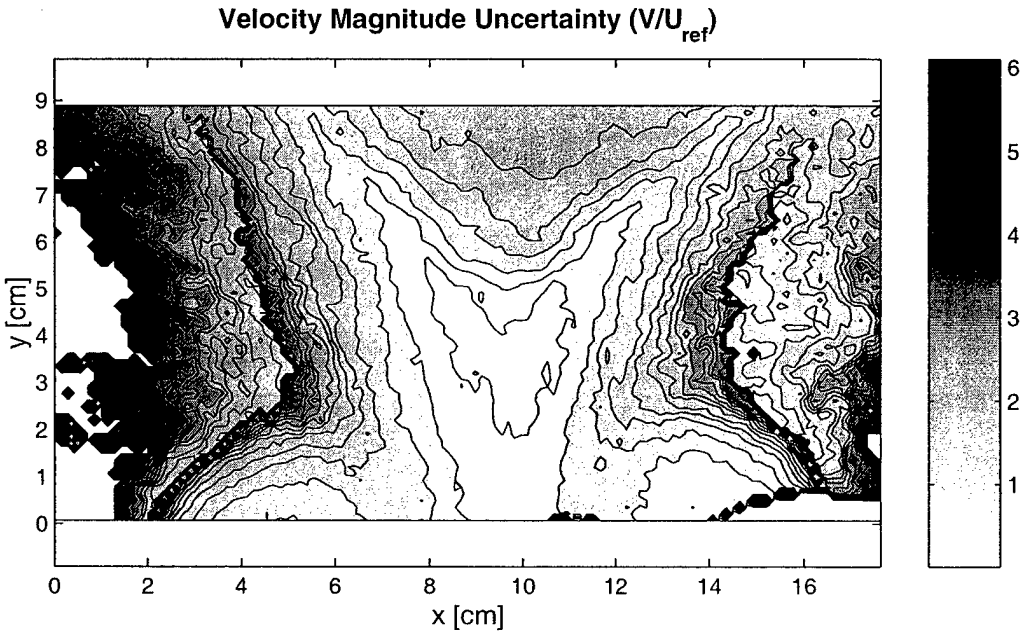

Figure 5.21: Contours of uncertainty levels for the $32.4\frac{m}{s}$ data images

Appendix A

Velocity Relations

The positioning of each DGV system module determines the measured velocity component, as shown in Equation 1.1. A coordinate transformation then resolves the measured velocity components into the desired final coordinate system. Calculation of the angles required for these transformations are discussed in Appendix B.

A.1 General Transformation

Consider the two coordinate systems, F_1 and F_2, shown in Figure A.1. The observer vector, $\overline{o_i}$, represents the observation direction of the i^{th} camera and is defined as a unit vector along the -z-axis of the F_2. Therefore, the vector components represented in F_2 system are;

$$\{\overline{o_i}\}_2 = \left\{ \begin{array}{c} 0 \\ 0 \\ -1 \end{array} \right\}_2$$

We wish to represent the direction vector in the F_1 system by means of a transformation. For convenience we choose the Euler angle *3-2-1* rotation sequence with the azimuth angle, ψ, elevation angle, θ, and roll angle, ϕ [38]. The transform matrix, T_{12}, is given by;

$$T_{12} = \left[\begin{array}{ccc} 1 & 0 & 0 \\ 0 & \cos\phi & \sin\phi \\ 0 & -\sin\phi & \cos\phi \end{array} \right] \cdot \left[\begin{array}{ccc} \cos\theta & 0 & -\sin\theta \\ 0 & 1 & 0 \\ \sin\theta & 0 & \cos\theta \end{array} \right] \cdot \left[\begin{array}{ccc} \cos(\psi) & \sin\psi & 0 \\ -\sin(\psi) & \cos(\psi) & 0 \\ 0 & 0 & 1 \end{array} \right]$$

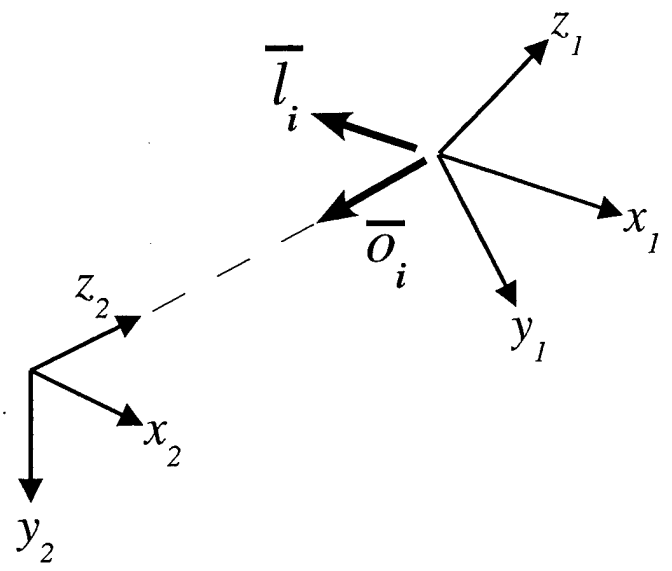

Figure A.1: Definition of primary and observer coordinate systems

Using this transformation, we may represent the observer vector in the F_1 system as;

$$\{\overline{o_i}\}_1 = T_{12}\{\overline{o_i}\}_2$$

Carrying out the transformation gives the observation unit vector,$\overline{o_i}$, represented in the F_1 system.

$$\{\overline{o_i}\}_1 = \left\{ \begin{array}{c} \sin\theta \\ -\sin\phi\cos\theta \\ -\cos\phi\cos\theta \end{array} \right\}_1 \tag{A.1}$$

A.2 Transformation Application

The preceding transformations relate a direction vector in two coordinate systems. The observation vector is required to apply the LDA equation as described in Section 1.2 Using the observation vector given in Equation A.1 we may derive the velocity relations required for the DGV system. The LDA equation for the i^{th} camera is written as,

$$\Delta f_i = \frac{1}{\lambda}(\overline{o_i} - \overline{l_i}) \cdot \overrightarrow{V}$$

We represent the incident laser direction vector in the F_1 system as,

$$\{\bar{l}\}_1 = \left\{ \begin{array}{c} l_x \\ l_y \\ l_z \end{array} \right\}_1$$

Viewing from three observation directions allows calculation of all three velocity components. Substituting in the observation and laser direction vectors results in the following equations:

$$\Delta f_1 = \frac{1}{\lambda} \left[\left\{ \begin{array}{c} \sin\theta_1 \\ -\sin\phi_1 \cos\theta_1 \\ -\cos\phi_1 \cos\theta_1 \end{array} \right\}_1 - \left\{ \begin{array}{c} l_x \\ l_y \\ l_z \end{array} \right\}_1 \right] \cdot \left\{ \begin{array}{c} V_x \\ V_y \\ V_z \end{array} \right\}_1 \tag{A.2}$$

$$\Delta f_2 = \frac{1}{\lambda} \left[\left\{ \begin{array}{c} \sin\theta_2 \\ -\sin\phi_2 \cos\theta_2 \\ -\cos\phi_2 \cos\theta_2 \end{array} \right\}_1 - \left\{ \begin{array}{c} l_x \\ l_y \\ l_z \end{array} \right\}_1 \right] \cdot \left\{ \begin{array}{c} V_x \\ V_y \\ V_z \end{array} \right\}_1 \tag{A.3}$$

$$\Delta f_3 = \frac{1}{\lambda} \left[\left\{ \begin{array}{c} \sin\theta_3 \\ -\sin\phi_3 \cos\theta_3 \\ -\cos\phi_3 \cos\theta_3 \end{array} \right\}_1 - \left\{ \begin{array}{c} l_x \\ l_y \\ l_z \end{array} \right\}_1 \right] \cdot \left\{ \begin{array}{c} V_x \\ V_y \\ V_z \end{array} \right\}_1 \tag{A.4}$$

Which can be written as a single system of equations given in A.5. The general solution for the three velocity components is given by Equation 4.3

$$\left\{ \begin{array}{c} \Delta f_1 \\ \Delta f_2 \\ \Delta f_3 \end{array} \right\} = \frac{1}{\lambda} \left[\begin{array}{ccc} \sin\theta_1 - l_x & -\sin\phi_1 \cos\theta_1 - l_y & -\cos\phi_1 \cos\theta_1 - l_z \\ \sin\theta_2 - l_x & -\sin\phi_2 \cos\theta_2 - l_y & -\cos\phi_2 \cos\theta_2 - l_z \\ \sin\theta_3 - l_x & -\sin\phi_3 \cos\theta_3 - l_y & -\cos\phi_3 \cos\theta_3 - l_z \end{array} \right] \cdot \left\{ \begin{array}{c} V_x \\ V_y \\ V_z \end{array} \right\}_1 \tag{A.5}$$

Appendix B

Module Orientation

All the planar Doppler systems reviewed in Chapter 2 report the orientation angles of the receiving cameras relative to the measurement plane, but none report how the angles were measured. For the systems which are built and operated on optical tables, the orientations of the modules is easily measured. Systems operated in large wind tunnel facilities however, present a new problem in determining the camera orientation. One possible method may involve surveying equipment to accurately measure the locations of each camera system. This solution would be accurate if done correctly, but involves a substantial investment in time and personnel. For the Virginia Tech DGV system a method for determining camera orientation was sought which eliminated the problems and inaccuracies of physical measurements. The search was also motivated due to the unique split-optics configuration of each camera module. The mirrors and beamsplitters used in each module change the optical axis of the camera system. Without the split-optics, the optical axis of the camera could be assumed along the centerline of the camera housing. These reasons lead to the investigation of image based orientation methods, including photogrammetric techniques, and then to new techniques developed for robotic vision systems.

B.1 Photogrammetric Techniques

Photogrammetry is the name of an entire class of methods employed to obtain information about physical objects through the analysis of photographic images [39]. The techniques were first employed in the creation of topographic maps from aerial photographs, and later in the analysis of satellite images. Almost all techniques used to measure objects from photographs were first developed for photogrammetric use.

The first investigations into determining camera orientations led to photogrammetric methods. Since photogrammetry relies on image analysis from cameras moving relative to the ground, many methods are available to orient the camera to the acquired image. However, these methods mainly rely on the use of special pre-calibrated cameras with precisely known parameters such as lens distortion. Also, photogrammetric methods are tailored for analyzing images acquired approximately vertically over the target area.

The digital dewarping process, discussed in Section 4.2.1, has an analog in photogrammetry which is called rectification. The rectification process is derived using analytical projective geometry, and for the special case of the projection of a planar surface, closed form solutions for the camera orientation are possible. This solution is given in Section 14.4.2 of Ref. [39]. The procedure requires 4 non-collinear points on the plane and their corresponding image points. The method was implemented and tested using the planar reference points obtained from the alignment dot grid for each camera. Results were obtained for only two of the three camera views. The highly oblique view from Camera 3 (see Figure 4.7) resulted in a solution singularity, which implied the method was not valid for highly oblique views. Failure of this method prompted research into the new areas of machine vision.

B.2 Machine Vision Techniques

In the context of machine vision, the process of determining the orientation of the camera system is known as camera calibration. It involves directly calculating the relationship between the image points and points in three-dimensional space. Determining this relationship, known as as the homography matrix, without the aide of special calibration equipment is called self-calibration [40].

The class of methods investigated to solve for the DGV camera calibration all use multiple views of a planar object. Viewing the same planar object, with known reference points, from multiple unknown orientations provides constraints on a non-linear optimization scheme which is solved for the camera calibration parameters. The methods assume that the multiple views are taken from the camera being calibrated, however, for the DGV the views are taken from different cameras. No restrictions were found which precluded this situation, and the results obtained support the validity of this application.

B.2.1 Calibration Method

The camera calibration method implemented in this research uses a toolbox for the Matlab environment created by Jean-Yves Bouguet, Ph.D. at the California Institute of Technology. He based the toolbox on various new calibration methods, including those of Zhang [40] and Tsai [41].

For input, the toolbox requires at least two distinct views of a planar surface with a series of reference points on each image. The three views of the alignment dot grid, taken during the DGV system setup, meet this requirement. All of the dot centroids, contained within the processing area for the reference view of each module, were input to the calibration program. The toolbox then performs an optimization loop which iteratively estimates the camera orientations required to produce the input reference points. After converging to a solution, the toolbox performs an analytical prediction of the grid points based on the computed parameters. These calculated reference points are plotted on the input images, which provides an immediate check on the results. The toolbox also outputs error information related to the predicted reference grid points.

B.2.2 Calibration Results

The results of running the calibration procedure are shown the following figures. Figure B.1 shows the reprojection error of the solution. Note the majority of the errors are less than 0.5 pixels. The calculated points are overlaid on the input images in Figures B.2, B.3, and B.4. The agreement with the input grid points is excellent. The returned camera to measurement plane transformation matrices (T_i) and the corresponding Euler angles (ϕ_i,θ_i,ψ_i) are:

$$T_1 = \begin{bmatrix} 0.5851 & 0.2779 & 0.7619 \\ 0.0484 & 0.9258 & -0.3749 \\ -0.8095 & 0.2563 & 0.5282 \end{bmatrix} \Rightarrow \begin{Bmatrix} \phi_1 \\ \theta_1 \\ \psi_1 \end{Bmatrix} = \begin{Bmatrix} -25.88° \\ -54.05° \\ -4.73° \end{Bmatrix} \quad \text{(B.1)}$$

$$T_2 = \begin{bmatrix} 0.8044 & -0.2246 & -0.5499 \\ -0.0078 & 0.9217 & -0.3879 \\ 0.5940 & 0.3163 & 0.7397 \end{bmatrix} \Rightarrow \begin{Bmatrix} \phi_2 \\ \theta_2 \\ \psi_2 \end{Bmatrix} = \begin{Bmatrix} -23.16° \\ 36.44° \\ 0.56° \end{Bmatrix} \quad \text{(B.2)}$$

$$T_3 = \begin{bmatrix} 0.9997 & -0.0080 & 0.0228 \\ 0.0235 & 0.5462 & -0.8373 \\ -0.0058 & 0.8376 & 0.5462 \end{bmatrix} \Rightarrow \begin{Bmatrix} \phi_3 \\ \theta_3 \\ \psi_3 \end{Bmatrix} = \begin{Bmatrix} -56.89° \\ -0.33° \\ -1.35° \end{Bmatrix} \quad \text{(B.3)}$$

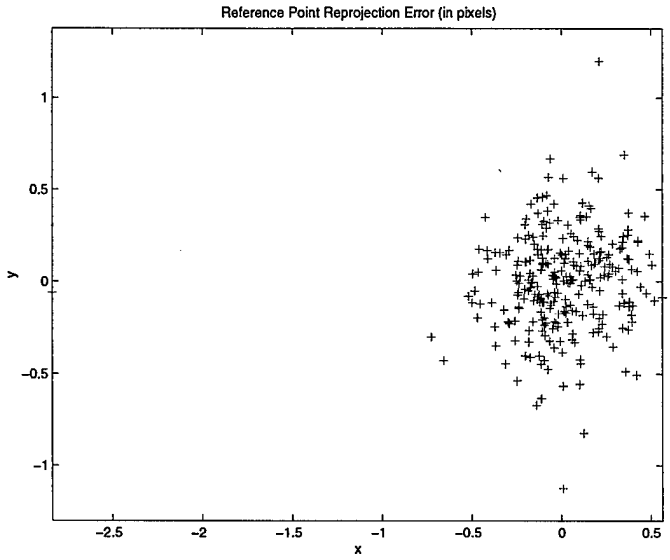

Figure B.1: Error, in pixels, of the analytical reprojection procedure using the calculated camera orientations, Camera 1 error=blue, Camera 2 error=red, Camera 3 error=green

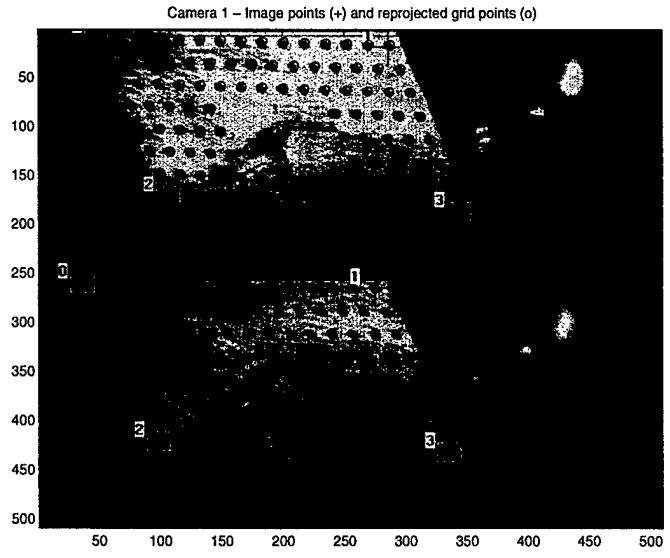

Figure B.2: Predicted reprojection points over the original input image points for Camera 1

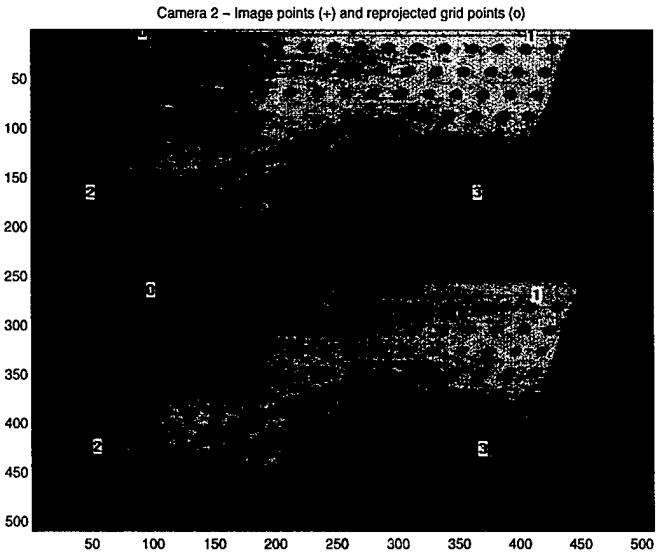

Figure B.3: Predicted reprojection points over the original input image points for Camera 2

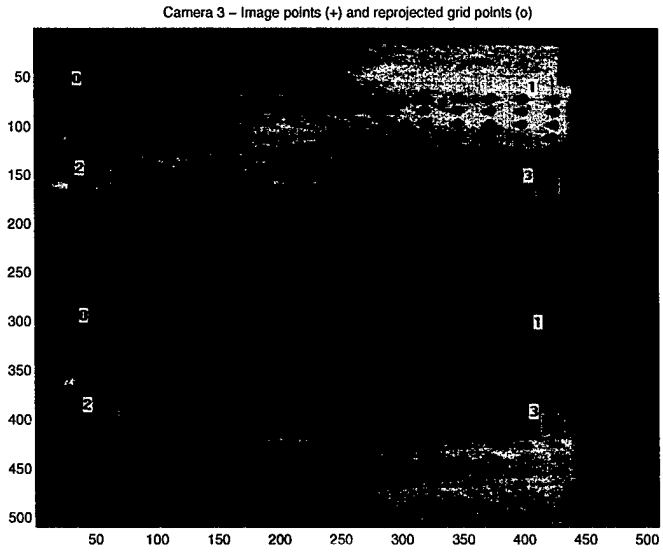

Figure B.4: Predicted reprojection points over the original input image points for Camera 3

Appendix C

Uncertainty Analysis

Calculation of uncertainty estimates for DGV velocity data is critical to understanding the quality of the acquired results. Unfortunately, the velocity data acquired during the first test of the Virginia Tech DGV contained too many unknown factors to warrant a detailed uncertainty analysis of the data. However, this appendix covers the techniques which may be applied to future data sets for uncertainty analysis.

C.1 Presented Velocity Uncertainties

The uncertainty estimates presented in Figure 5.21 are based only on the standard deviation of the averaged image set intensities. As discussed in Section 5.2.3, velocity images of the prolate spheroid flow were acquired using multiple laser pulses per images. This compromise resulted in a loss of all per-pulse laser frequency information, which prevented correction of the images for laser frequency drift.

Without the laser frequency corrections, the resulting images contained high variability in the brightness levels. The first step in the uncertainty estimation was averaging the velocity data images and calculating the standard deviation of the brightness levels at each pixel. This process produced an average image and a "standard deviation" image. The averaged image was then processed into velocity data as described in Section 4.3. Then twice* the standard deviation image was added to the average image, and the reduction process repeated. The resulting velocity data then became the upper bound on the velocity uncertainty. Subtracting twice the standard deviation image from the

*The factor of two is conservative estimate from the Student's T distribution for calculating a 95% confidence level uncertainty from the standard deviation [42].

average was not successful. The standard deviation values were large enough that the resulting filtered image pixel values were zero. Therefore the lower uncertainty bound was assumed equal to the upper bound. Thus, the velocity data uncertainty plot in Figure 5.21 strictly represents only the upper bound uncertainties.

C.2 Detailed Uncertainty Techniques

Future DGV data sets will require a more detailed estimation of the measurement uncertainties. Performing a detailed uncertainty analysis first requires determining the independent variables which affect each measurement. The sensitivity of the final measurement to variance in each independent variable leads to an estimate on the total uncertainty [42]. For a measured quantity g which is a function of n variables, x_1,x_2,... x_n, the total uncertainty is:

$$\omega g = \sqrt{\left[\omega x_1 \frac{\partial g}{\partial x_1}\right]^2 + \left[\omega x_2 \frac{\partial g}{\partial x_2}\right]^2 + \ldots + \left[\omega x_n \frac{\partial g}{\partial x_n}\right]^2} \tag{C.1}$$

where ωg is the total uncertainty, and ωx_n is the uncertainty on variable x_n.

C.2.1 Governing Equations

Applying Equation C.1 to the uncertainty analysis of DGV data requires defining the governing equation for the measurement (the function g). For defining the governing equation we limit the variables to the measured or calculated quantities used in the reduction of image intensity ratios to velocities. Errors involved in these quantities are random, whereas errors from processes like the background and pixel sensitivity corrections are bias errors. Under these assumptions, the functional dependencies for the velocity at each pixel location are:

$$V_x = V_x\left(\Delta f_1, \Delta f_2, \Delta f_3, l_x, l_y, l_z, \theta_1, \theta_2, \theta_3, \phi_1, \phi_2, \phi_2\right) \tag{C.2a}$$
$$V_y = V_y\left(\Delta f_1, \Delta f_2, \Delta f_3, l_x, l_y, l_z, \theta_1, \theta_2, \theta_3, \phi_1, \phi_2, \phi_2\right) \tag{C.2b}$$
$$V_z = V_z\left(\Delta f_1, \Delta f_2, \Delta f_3, l_x, l_y, l_z, \theta_1, \theta_2, \theta_3, \phi_1, \phi_2, \phi_2\right) \tag{C.2c}$$

where Δf_i is the Doppler shift from each direction, $\overrightarrow{l}$ is the laser incident direction vector, and the angles θ_i and ϕ_i define the rotation between the camera coordinate system and

the measurement plane (see Section A.2). The following sections detail the sensitivity of the final velocity measurement to each set of variables.

C.2.2 Doppler Shift Uncertainties

The three Doppler shift values $(\Delta f_1, \Delta f_2, \Delta f_3)$ used in calculating the velocity vector from Equation 4.3 are functions of other input variables. Since the Doppler shift frequencies are so critical in the velocity calculation, these dependencies must be calculated and added into the velocity uncertainty. The Doppler shift at each point is determined by the iodine cell calibration polynomial (see Section 4.3.1) which returns frequency as a function of transmission ratio. The iodine cell calibration polynomial with its functional dependencies is written as:

$$f_i(TR_i, T_s) = c_1(T_s) + c_2(T_s)TR_i + c_3 {TR_i}^2 + c_4(T_s){TR_i}^3 + c_5 {TR_i}^4 + c_6(T_s){TR_i}^5 \quad \text{(C.3)}$$

where TR_i is the transmission ratio for a given pixel from DGV module i, and T_s is the iodine cell stem temperature. Currently all iodine cells use the same polynomial equation, which implies the same stem temperature for each cell, so the Doppler shift at each pixel is given by:

$$\Delta f_1(TR_1, TR_1^{ref}, T_s) = f(TR_1, T_s) - f(TR_1^{ref}, T_s) \quad \text{(C.4a)}$$
$$\Delta f_2(TR_2, TR_2^{ref}, T_s) = f(TR_2, T_s) - f(TR_2^{ref}, T_s) \quad \text{(C.4b)}$$
$$\Delta f_3(TR_3, TR_3^{ref}, T_s) = f(TR_3, T_s) - f(TR_3^{ref}, T_s) \quad \text{(C.4c)}$$

where TR_i^{ref} is the reference transmission for the i^{th} module. The reference TR is calculated from white card images acquired with the laser tuned to a middle point on the absorption line (see Section 4.3.2). Applying Equation C.1, the Doppler shift uncertainty equation for the i^{th} DGV module is:

$$\omega \Delta f_i = \sqrt{\left[\omega TR_i \frac{\partial \Delta f_i}{\partial TR_i}\right]^2 + \left[\omega TR_i^{ref} \frac{\partial \Delta f_i}{\partial TR_i^{ref}}\right]^2 + \left[\omega T_s \frac{\partial \Delta f_i}{\partial T_s}\right]^2} \quad \text{(C.5)}$$

The polynomial form of Equation C.4 allows direct (although tedious) calculation of the partial derivatives with respect to TR_i and TR_i^{ref}. The sensitivity of the Doppler shift with iodine cell stem temperature is less straightforward. The polynomial coefficients in

Equation C.3 are found by fitting output points from a computational iodine absorption model (see Section 4.3.1) and are a strong function of stem temperature. Determining the partial derivatives $\frac{\partial \Delta f_i}{\partial T_s}$ requires creating polynomial fit equations for various stem temperatures and calculating $\frac{\partial \Delta c_j}{\partial T_s}$, where c_j is the j^{th} coefficient in Equation C.3. An example of this calculation is shown in Figure C.1. The linear fits to the variance of each coefficient are quite good and suggest that a future calibration function method may employ linear corrections on the coefficient values to match the exact stem temperature for each data image. Using the linear coefficient equations, Equation C.4 can re-written as an explicit function of temperature, allowing direct calculation of the required partial derivative.

Performing the suggested calculations for the parameter values used in reducing the presented data set results in the following Doppler shift uncertainties;

Table C.1: Measured Doppler shift uncertainties for tested configuration

Component	Value (Hz)
$\omega\Delta f_1$	2.9876×10^6
$\omega\Delta f_2$	3.4054×10^6
$\omega\Delta f_3$	3.6425×10^6

It should be noted that these uncertainty values are for a stem temperature (T_s) uncertainty of $\pm 0.25°C$. This is to compensate for all three modules using the same frequency calibration function. However, even if the ωT_s value is lowered to the experimental average of $0.058°C$ (see Section 5.3.2), the resulting Doppler shift uncertainties change by only 0.7%. A much larger contribution to the Doppler shift uncertainty is made by the uncertainty of the reference transmission ratio values (ωTR_i^{ref}). The values of ωTR_i^{ref} were estimated from the white card images acquired at the laser set point frequency used to calculate TR_i^{ref} and had an average value of 0.0034. Reducing brightness variance across the white card images by reducing variance in the laser illumination will improve the Doppler shift uncertainties.

Calculating the partial derivatives of the final velocities with respect to the Doppler shift values is necessary to estimate the velocity uncertainty for a given Doppler shift uncertainty. The functional dependence of velocity with Doppler shift is given in Equation C.6:

$$V_x = m_{11}\Delta f_1 + m_{12}\Delta f_2 + m_{13}\Delta f_3 \quad \text{(C.6a)}$$
$$V_y = m_{21}\Delta f_1 + m_{22}\Delta f_2 + m_{23}\Delta f_3 \quad \text{(C.6b)}$$
$$V_z = m_{31}\Delta f_1 + m_{32}\Delta f_2 + m_{33}\Delta f_3 \quad \text{(C.6c)}$$

where the matrix of coefficients (**m**) is defined by the right hand side terms of Equation 4.3. The required partial derivatives of $\frac{\partial V_x}{\partial \Delta f_i}$, $\frac{\partial V_y}{\partial \Delta f_i}$, and $\frac{\partial V_z}{\partial \Delta f_i}$ are then simply the components of the matrix **m**. The values of these derivatives for the tested configuration are;

Table C.2: Velocity component sensitivities to Doppler shift $[\frac{m}{s}/Hz]$

Component	$\frac{\partial}{\partial \Delta f_1}$	$\frac{\partial}{\partial \Delta f_2}$	$\frac{\partial}{\partial \Delta f_3}$
V_x	-5.66769×10^{-7}	3.83743×10^{-7}	2.84368×10^{-8}
V_y	-1.71676×10^{-7}	-5.34304×10^{-7}	8.89492×10^{-7}
V_z	-1.29486×10^{-6}	-1.20835×10^{-7}	4.41785×10^{-7}

C.2.3 Angular Dependencies

In addition to the direct dependence of the calculated velocity component on the Doppler shift, the velocity value is also a function of the orientation parameters for the camera systems. This dependence arises from the coordinate transformation used in derivation of the velocity equations (see Section A.2). Due to the simultaneous nature of the velocity solution, each calculated component is a function of all orientation parameters. The laser direction vector is also used in the calculation of the velocity vector. This section details the uncertainties in the final velocity calculation caused by random error in the camera system and laser vector orientation angles.

Camera Orientation

The Matlab toolbox used for calculation of the camera orientation parameters (see Section B.2.1) does not provide obvious uncertainty estimations for the results. The error indications given relate to the accuracy of analytical reprojection of the input reference points. These pixel errors (shown in Figure B.1) are all on the order of 0.5 pixels. This distance in pixels can be converted to actual distances using the known spacing between

the reference grid points. The required scaling factor is approximately $0.31\frac{mm}{pixel}$, which yields an average positional error of $0.16mm$. To find the Euler angle uncertainties which correspond to the estimated positional errors, an iterative procedure of perturbing the angles and calculating the change in a transformed position vector is used. Using this method, angular uncertainties of the Euler angles were estimated as $\pm 0.75°$. For simplicity, the same uncertainty value is used for all the camera modules.

The sensitivity derivatives of the velocity governing equations are needed for calculation of the total uncertainty. Unlike the polynomial equation for the Doppler shift, the complex relationship between the Euler angles and the velocity does not allow for direct calculation of the partial derivatives. Therefore a numerical perturbation technique, similar to the process already discussed in the previous section, must be employed. This method requires changing each Euler angle by a small amount and re-calculating the velocity vector. The process is then repeated for points above and below the nominal case. Results of this analysis are shown in Figure C.2, and the sensitivity slopes (in units of $\frac{m}{s}/\Delta°$) are listed in Tables C.3 and C.4.

Table C.3: Velocity component sensitivities to Euler elevation angle ϕ_i

Component	$\frac{\partial}{\partial\theta_1}$	$\frac{\partial}{\partial\theta_2}$	$\frac{\partial}{\partial\theta_3}$
V_x	−0.51303	0.59523	0.04904
V_y	−0.15541	−0.82876	1.53378
V_z	−1.17209	−0.18743	0.76178

Table C.4: Velocity component sensitivities to Euler roll angle ϕ_i

Component	$\frac{\partial}{\partial\phi_1}$	$\frac{\partial}{\partial\phi_2}$	$\frac{\partial}{\partial\phi_3}$
V_x	1.13485	−1.04921	−0.08517
V_y	0.34376	1.46086	−2.66430
V_z	2.59271	0.33037	−1.32329

The majority of the results indicate that uncertainties as high as $\pm 2°$ create a change of 5% or less in the velocity component. The notable exceptions to this trend are the sensitivities of V_y to ϕ_3 and V_z to ϕ_1 and ϕ_3. The estimated Euler angle uncertainties of $\pm 0.75°$ for the Virginia Tech DGV system result in percentage uncertainties of only 1-3%.

Laser Plane Orientation

The final variable investigated in this uncertainty analysis is the angular orientation of the laser measurement plane. The vector components of the laser incident direction vector ($\bar{l}$) are subtracted from the transformed components of the observation vector ($\bar{o}$) and appear in Equation 4.3. The vertical angle of the laser plane (see Figure 5.2) during the system tests was set to $26.2 \pm 0.1°$ using a rotary table mount. Because of the high confidence level in the vertical angle setting, only the uncertainty of the transverse angle (horizontal and perpendicular to the flow direction) is presented. Also note that once the laser beam passes through the sheet optics, a single vector cannot fully describe the orientation of the resulting plane.

As in the preceding case of the Euler angle sensitivities, the laser plane uncertainty analysis first requires an estimate on the angular uncertainty of the tested plane. The perpendicular alignment procedure (see Section 5.1.4) for the measurement plane utilized laser back reflections across the tunnel test section. Measuring the laser spot positions on either tunnel wall provided an uncertainty estimate of approximately $\pm 0.2°$ perpendicular. To allow for imperfections in the spot measurements and the tunnel side walls, an uncertainty value of $\pm 0.5°$ is used in this analysis.

A plot of the sensitivity of the velocity component measurement with changes in the laser vector horizontal angle (γ) is shown in Figure C.3. The sensitivity slopes of the linear fits are listed in Table C.5.

Table C.5: Velocity component sensitivities to the laser plane horizontal angle γ

Component	$\frac{\partial}{\partial \gamma}$
V_x	0.24868
V_y	−0.26361
V_z	1.69445

The laser plane angle sensitivity trends are less linear than the corresponding Euler angle values. The trends for V_x and V_y produce less than 2% variation in the velocity and are fairly symmetric, while the effects on V_z are not symmetric and are as high as 12%. Based on the uncertainty estimate for the horizontal laser plane angle of $\pm 0.5°$, the resulting velocity uncertainties are less than 2% for V_x and V_y, and approximately 5% for V_z.

C.2.4 Final Uncertainty Calculation

Once all the component uncertainties and sensitivities are calculated, the final base uncertainty can be determined for each velocity component. The term "base uncertainty" is used to clarify further that the results presented in this section *do not* include the uncertainties associated with the transmission ratio (TR_i), therefore the values of ωTR_i are all zero (see Equation C.5).

The equation for calculating the uncertainty of the V_x velocity component is:

$$\omega\Delta V_x = \sqrt{\left[\omega\Delta f_1 \frac{\partial\Delta V_x}{\partial\Delta f_1}\right]^2 + \ldots + \left[\omega\Delta f_3 \frac{\partial\Delta V_x}{\partial\Delta f_3}\right]^2 + \left[\omega\theta_1 \frac{\partial\Delta V_x}{\partial\theta_1}\right]^2 + \ldots} \overline{+ \left[\omega\theta_3 \frac{\partial\Delta V_x}{\partial\theta_3}\right]^2 + \left[\omega\phi_1 \frac{\partial\Delta V_x}{\partial\phi_1}\right]^2 + \ldots} \overline{+ \left[\omega\phi_3 \frac{\partial\Delta V_x}{\partial\phi_3}\right]^2 + \left[\omega\gamma \frac{\partial\Delta V_x}{\partial\gamma}\right]^2} \quad \text{(C.7)}$$

with similar equations for V_y and V_z. The base velocity component uncertainties for the Virginia Tech DGV system in the tested configuration are listed in Table C.6.

Table C.6: Virginia Tech DGV base velocity component uncertainty levels

Component	Base Uncertainty $[\frac{m}{s}]$
V_x	2.51
V_y	4.59
V_z	4.94

C.2.5 Hypothetical Uncertainty Levels

All of the previous uncertainty results are for a system with no uncertainty on the transmission ratios ($\omega TR_i = 0$). This was done due to the high average level of variance in the transmission ratios of the acquired test data set of the prolate spheroid flow. However, it is important to understand the relationship between the transmission ratio uncertainties and the final velocity uncertainty. With this knowledge, future data sets can be quickly analyzed for validity, indicating if the set must be re-acquired. This type of analysis will increases the probability of producing accurate velocity results.

Reference Transmission Ratios

The uncertainty levels of the reference transmission ratios, ωTR_i^{ref}, *were* included in the above analysis, but varying those levels provides insight into the sensitivity of the velocity

uncertainty to the reference transmission ratios. Table C.7 lists the nominal uncertainties in the values of ωTR_i^{ref} and the corresponding velocity component uncertainties. The remaining values listed are for halving and then doubling the values of ωTR_i^{ref}. The results indicate that decreasing the reference transmission ratio uncertainty levels by a factor of two improves the overall velocity uncertainties by an average of 31%.

Table C.7: Virginia Tech DGV base velocity component uncertainty levels

ωTR_1^{ref}	ωTR_2^{ref}	ωTR_3^{ref}	ωV_x	ωV_y	ωV_z
0.0013	0.0022	0.0017	1.69	3.26	3.34
0.0026	0.0043	0.0033	2.51	4.59	4.94
0.0053	0.0086	0.0066	4.48	7.92	8.80

Transmission Ratios

The last variable analyzed is the uncertainty of the transmission ratio (ωTR_i). The method used to compute the velocity uncertainties was applied with increasing levels of ωTR_i and all other variables set their nominal values. The results of this analysis are plotted in Figure C.4. Note that to maintain the lowest possible velocity uncertainties, the values of ωTR_i must be of the same order as ωTR_i^{ref}. Higher TR uncertainties increase the overall velocity uncertainty almost exponentially. These results are the key reason more detailed velocity uncertainty calculations were not performed for the prolate spheroid wake DGV data. The uncertainties of the transmission ratios in the acquired data sets were in excess of 0.04 for Cameras 1 and 3, which is twice the maximum value plotted in Figure C.4, and above 0.1 for the Camera 2 images. This implies the actual uncertainty levels for the acquired data set are near $40\frac{m}{s}$ in the center of the wake region for Cameras 1 and 3, and near $90\frac{m}{s}$ in the same region for Camera 2.

C.3 Uncertainty Analysis Conclusions

The presented detailed uncertainty analysis provided insight in the major sources of possible uncertainty in the Virginia Tech DGV system. The "base uncertainty" velocity levels for an average data set are less than $5\frac{m}{s}$. Those values may be immediately reduced by improvements in the DGV calibration techniques, such as diffusing the laser light to produce more uniform illumination on the target. Improved laser operation and flow

seeding should reduce the uncertainty of the transmission ratios. These enhancements should result in a system capable of uncertainties in the $2\frac{m}{s}$ range.

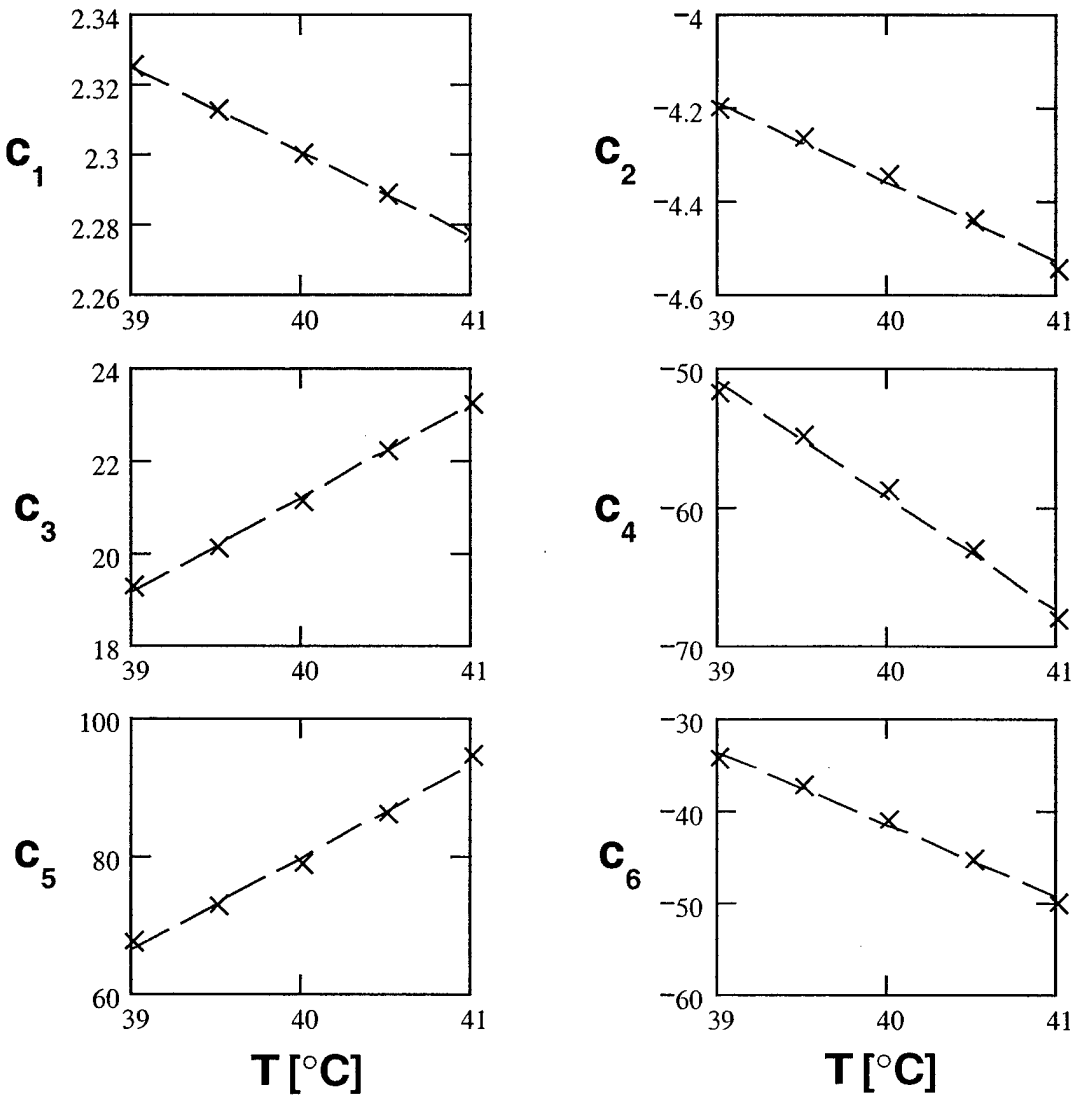

Figure C.1: Frequency function coefficient sensitivity with iodine cell stem temperature

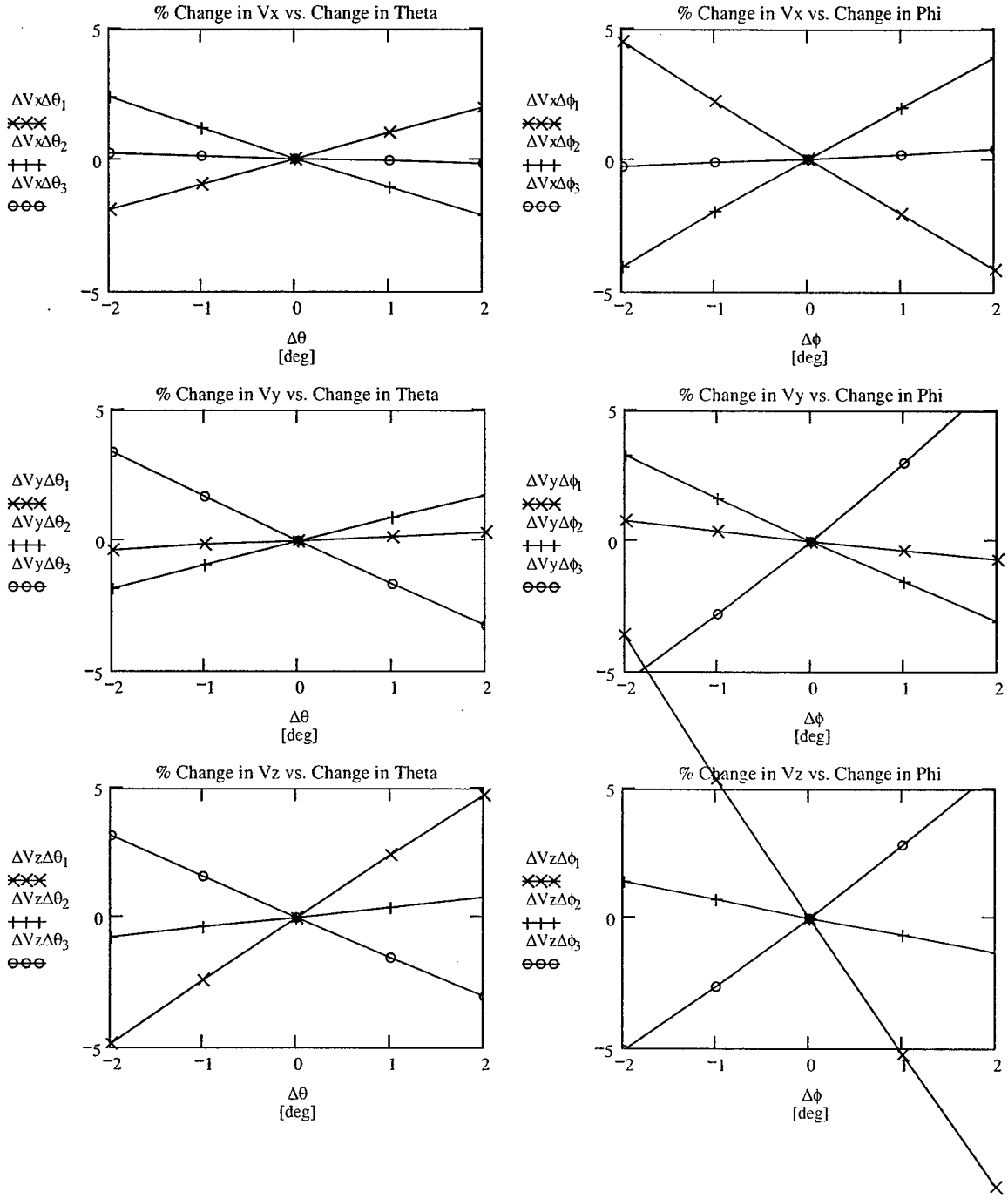

Figure C.2: Velocity component sensitivity with changes in Euler rotation angles

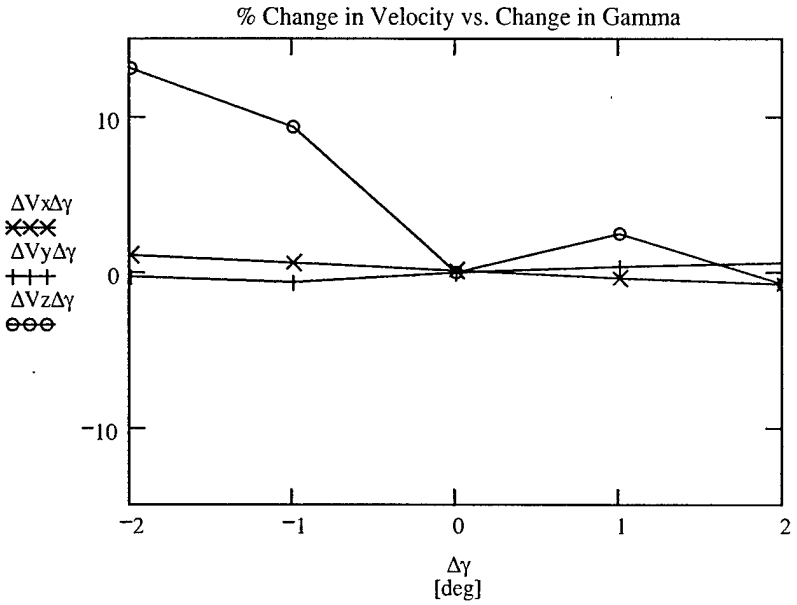

Figure C.3: Velocity component sensitivity with changes in the laser plane horizontal angle

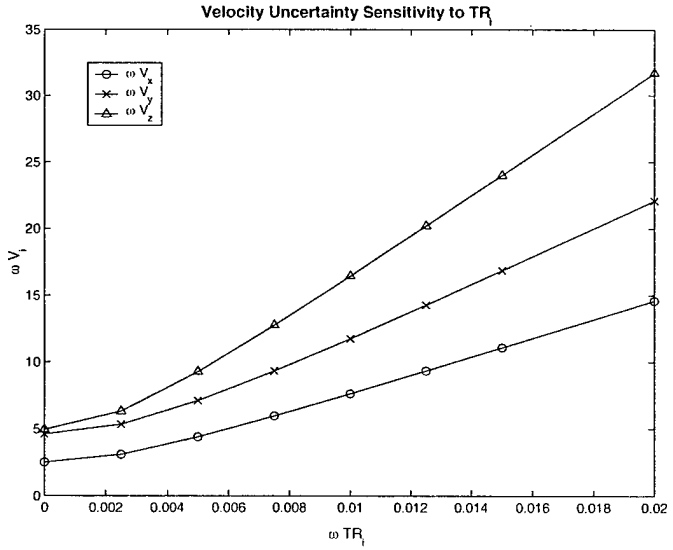

Figure C.4: Velocity component uncertainty sensitivity with changes in transmission ratio (ωTR_i)